UCLouvain

epl

École polytechnique de Louvain

# Planar inductors for detection of magnetic nanoparticles in a paper-based water quality monitoring system

Author: **Dorian Van Nieuwenhove**
Supervisor: **Jean-Pierre Raskin**
Readers: **Laurent Francis, Margo Hauwaert, Martin Lefebvre**
Academic year 2022–2023
Master [120] in Electrical Engineering

# Acknowledgements

This dissertation is not only the fruit of several hundred hours of work, but also the accomplishment of a long road travelled since the beginning of my university studies. I would therefore like to thank all the people who made this thesis possible:

Prof. Jean-Pierre Raskin for having accepted to be my promoter and to have proposed me to take part in the project of which this work is composed, as well as for having kindly supervised me many times during my research and during my studies, notably during my internship or the IngénieuxSud project.

Margo Hauwaert and Martin Lefebvre for their guidance throughout the year, and for calling me to order when my commitment was lacking, for their many words of advice and the pertinence of their comments, and for proofreading my manuscript.

Prof. Laurent Francis for his attention to my subject and his willingness to take part in my restricted jury.

Fares Tounsi who was always there to help me, answer my questions, give me advice, or provide me with material for my measurements, as well as for his tutoring on how to use KiCad and print my inductors.

Benoît Hubert, with whom I spent a lot of time soldering, and who was there whenever I had a question about the WELCOME platform, or to repair my printing and soldering. As well as Souley Djandjandi for letting me print dozens of inductors during the year, and Pascal Simon for training me in the use of the VNA.

To all my friends who have always supported me, especially my roomates of Kap-Hot, as well as Elise, Martin, Nadeige and David for our study sessions in this geography room we have made our own.

Special thanks to Colin Noël for helping me understand and move forward with my research when it became difficult.

Louise Jacques, a.k.a. Salmon, who put up with me throughout the journey of this work.

My family for their support, especially my father for the English proofreading.
And above all, a huge thank you to my mother who, despite a support filled with doubts and worries, was always there to support me, assist me, and above all re-read my work several times.

# Abstract

Water quality is a central concern for human health and environmental preservation, particularly in remote areas where access to drinking water is difficult. Faced with this need, the development of a point-of-care biosensors is emerging as a promising solution to carry out analyses in the field, without the need for specific technical knowledge or equipment.

One of the strategies being considered for the quantification of bacterial concentration in water is based on magnetic nanoparticles that bind to bacteria and are then detected with planar inductors, which have the advantage of being economical and easy to produce. This research focuses on the in-depth analysis of these planar inductors and their role in the detection of magnetic nanoparticles. The goal is to use a pair of exciting and sensing inductors in a differential fashion to refine the detection sensitivity. In this study, we develop theoretical models to derive the electrical parameters from the geometric specifications of the inductors.

Our results highlight the performance of the exciting and sensing inductor pair, underlined by a variation of 4 to 5% of the initial voltage in response to the presence of ferromagnetic materials with a surface area of 1 $cm^2$, as well as a variation of 0.001 to 0.002% caused by the presence of magnetic nanoparticles. Possible improvements, particularly in terms of magnetic coupling, have been proposed, allowing a maximum k-factor of 0.46 for the design of a simple pair of internal/external inductors. Other designs, such as interleaved inductors, have been suggested to achieve magnetic coupling coefficients greater than 0.6. In addition, the study of differential systems integrating these inductors reveals a clear potential to make the system almost 10 times more sensitive. This work thus paves the way for functional and efficient magnetic nanoparticle detectors for water quality monitoring.

# Acronyms

**AMR** Anisotropic magnetoresistance.
**AuNP** gold nanoparticle.

**BNC** Bayonet Neill-Conceman connector.

**CMOS** complementary metal oxide semi-conductor.

**DUT** device under test.

**GMR** Giant magnetoresistance.

**IES** electrochemical Impedance Spectroscopy.

**LFA** lateral flow assay.
**LoD** limit of detection.

**MFLI** multifonction Lock-In.
**MNP** magnetic nanoparticles.
**MP** magnetic particles.
**MR** magnetoresistance.
**MRS** magnetic relaxation switching Detection.

**PCB** printed circuit board.
**PHE** planar Hall effect.
**POC** point-of-care.

**RMS** Root Mean Square.

**SMA** Sub-Miniature version A.
**SNR** signal-to-noise ratio.
**SQUID** superconducting Quantum Interference Device.

**TMR** Tunnel magnetoresistance.

**VIA** vertical interconnect access.
**VNA** vector network analyzer.

**WHO** World Health Organization.

# Introduction

*« We will not be able to defeat any of the infectious diseases that afflict developing countries until we win the battle for clean water, sanitation and basic health care. »* - Kofi Annan (1938 - 2018), septième secrétaire général des Nations unies, prix Nobel de la paix 2021 [1].

Water, this precious element, not only quenches our thirst, but also plays an essential role in maintaining good hygiene, fighting many diseases and preventing deadly infections. Yet more than 2 billion people live in regions where access to water is limited, a situation that is worsening with climate change and demographic expansion [2]. Given this stark reality, it is alarming to note that 8% of the world's population, or more than 686 million people, rely on unprotected surface water or springs [3]. Every drop of water that contains microbiological contaminants can serve as a vector for devastating diseases. These diseases, including diarrhea, cholera, and poliomyelitis, are responsible for some 485,000 deaths a year from diarrheal complications [2].

To better meet the need for water quality control, a point-of-care (POC) **bacteria** biosensor is being developed to meet the « **ASSURED** » criterion defined by World Health Organization (WHO): Affordable, Sensitive, Specific, User-friendly, Rapid and robust, Equipment-free and Deliverable to end-users [4].
This biosensor is based on the use of lateral flow assay (LFA) [5, 6] paper-based [7] as well as the use of magnetic nanoparticles (MNP) [8, 9] allowing the bacteria to be **labeled** in order to improve the limit of detection (LoD).

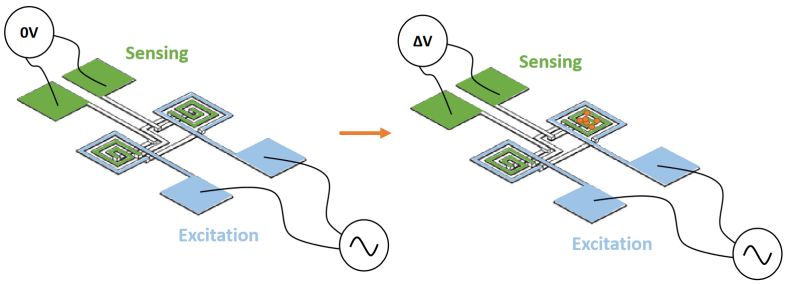


Figure 1 – Differential MNP sensor concept. Illustration by M. Hauwaert from [10]

It is in this context that this work takes place. The main objective is to develop and master the use of **square planar inductors** to detect MNP. The idea originates from the article *"Modeling and Simulation of Magnetic Nanoparticle Sensor"* by J. Mäkiranta and J. Lekkala [10] using planar inductors in a differential system (Fig. 1).

This thesis consists of four main parts. In the first, we will review the state of the art of existing solutions and knowledge regarding the detection of MNP. First, we will highlight the concepts involved in characterizing a sensor, then go on to describe the various magnetic

properties useful for detecting MNP, before concluding with a comparison of different methods, highlighting the advantages and disadvantages of a sensor based on planar inductors.

Second, we will present various models for characterizing a square planar inductor by its geometric parameters, and then print out a simple planar inductor to measure and model its electromagnetic behavior when immersed in a controlled variable magnetic field.

We will then develop a pair of exciting/sensing inductors. We will use various ferromagnetic, nanocrystalline, and amorphous samples to characterize the frequency response of the voltage induced across the sensitive inductor. We will highlight the electromagnetic behavior, the various specificities measured, and the limitations of our system.

Finally, we present three differential system designs to improve the sensitivity of our detector. The first design is based on the inductor pairs already presented, while the second and third designs are based on interleaved and superimposed inductors, respectively. The advantages and limitations of these systems are measured and discussed at the end of this fourth section.

This work concludes with a review of the different stages and relevant results encountered in the use of planar inductors for the detection of magnetic nanoparticles.

# Contents

# Chapter 1

# State of the art

The first part of this thesis describes the main aspects of the magnetic nanoparticle detector, and reviews the state of the art in nanoparticle detection techniques. This chapter is divided into three distinct sections :

1. **Sensors** : via a synthetic overview, an introduction to the subject of sensors will be made by discussing about their main characteristics as well as biosensors and examples of transductions.
2. **Magnetic nanoparticles** : the primary aim of our sensor is to measure the concentration of magnetic nanoparticles, which will ultimately be attached to bacteria in a given sample. We will be introducing these particles, their properties and the means of detection based on these properties.
3. **Inductances** : our detector relies on the variation of magnetic behavior in the vicinity of inductances whose electrical parameters we measure. In this section, we will therefore define the theoretical concepts useful for understanding the system under study.

## 1.1 Sensors

The very basis of the project is to develop a sensor. But what is a sensor? A sensor converts physical input signals into electrical output [11]. From the sensor, we can differentiate the transducer (Fig. 1.1), which will be the centerpiece of the detector. The transducer will enable us to transform our physical quantity into another type that can be easily processed. For example, we want the voltage of our device to vary according to the concentration of our magnetic nanoparticles.

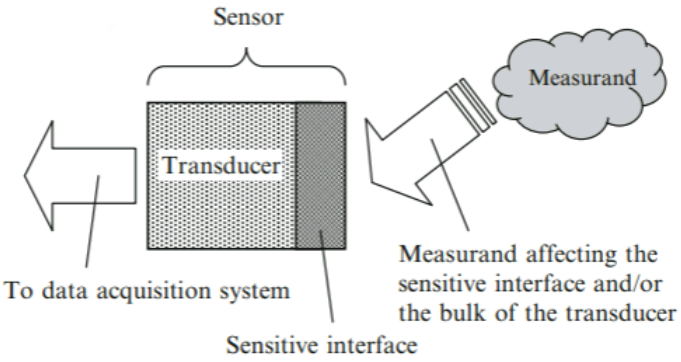


Figure 1.1 – Schematic representation of a detection system [12]

A sensor can be defined by a number of parameters and characteristics. One of the first steps in its development is to determine its transfer function, defined as the response of the sensor to the stimulus. Generally speaking, finding the exact transfer function of a complex sensor is not so easy. We therefore resort to approximations.

A **linear approximation** (Fig. 1.2a) of a transfer function and its inverse transfer function can be defined by :

$$E = A + Bs \tag{1.1}$$

$$s = \frac{E - A}{B} \tag{1.2}$$

with

— E : the measurement of the receiving signal

— s : the stimulus sent to the sensor

— A : the measurement when there is no stimulus (s = 0)

— B : the measured slope of the linear regression of our signal. This slope is called the **sensitivity**, because the higher the slope, the more the sensor's output signal varies as a function of the stimulus.

We also find the transfer function and its inverse by **logarithmic approximation** (Fig. 1.2b) :

$$E = A + B\ ln(s) \tag{1.3}$$

$$s = e^{\frac{E-A}{B}} \tag{1.4}$$

As well as the **exponential approximation** (Fig. 1.2c) :

$$E = Ae^{ks} \tag{1.5}$$

$$s = \frac{1}{k} ln(\frac{E}{A}) \tag{1.6}$$

where $k$ is a fixed parameter. And the **power approximation** (Fig. 1.2d):

$$E = A + Bs^k \tag{1.7}$$

$$s = \sqrt[k]{\frac{E - A}{B}} \tag{1.8}$$

In addition to the transfer function modeling our sensor's response, it also has an operating domain, notably a **detection limit** determining the minimum magnitude to which the sensor is capable of responding, as well as an upper limit, called **saturation**, above which a sensor is no longer capable of responding according to the stimulus detected (Fig. 1.3).

In addition to these upper and lower limits, sensors are only able to detect a certain amount of variation, called **resolution**. Resolution is the minimum change in the stimulus that creates a detectable increment in the output signal. Resolution is greatly limited by the noise present in the signal.

### 1.1.1 Noise

Unexpected changes in the output signal are defined as noise [13, 14].
As our sensor is designed to be economical, it will be more sensitive to noise, so it is important to consider this when designing our system.

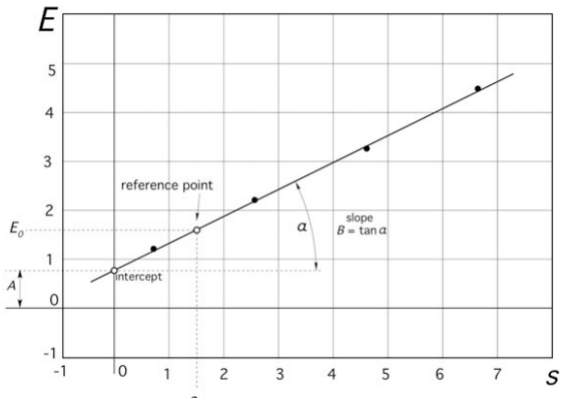


(a) Linear approximation

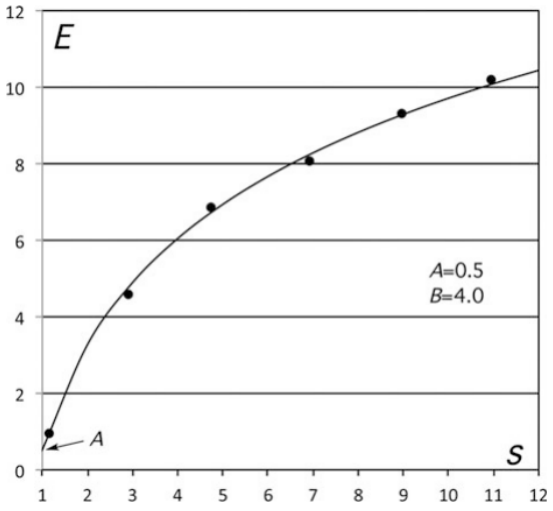


(b) Logarithmic approximation

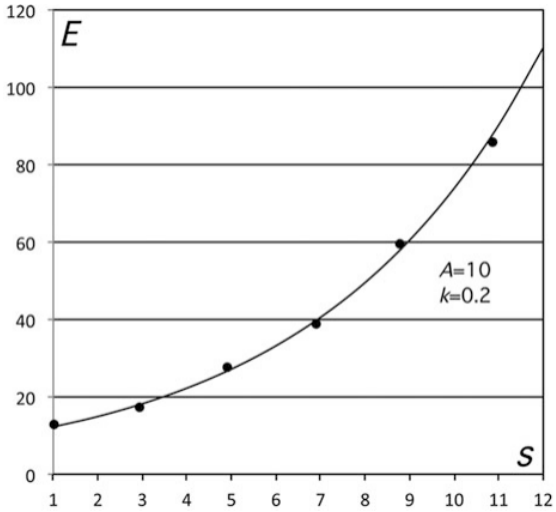


(c) Exponential approximation

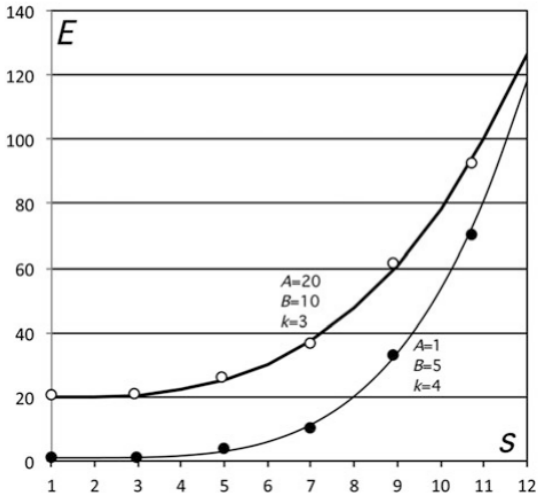


(d) Power approximation

Figure 1.2 – Illustrations of different transfer function approximations [11]

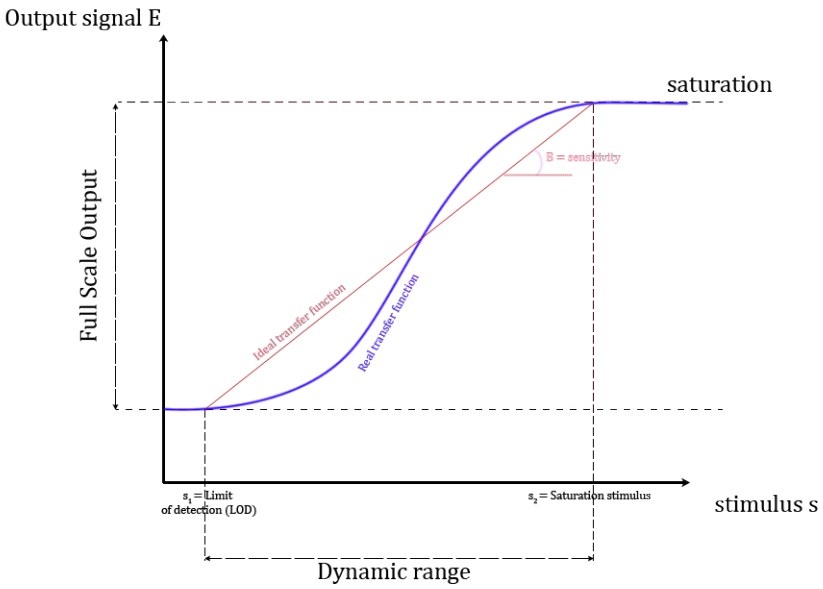


Figure 1.3 – Overview of sensor transfer function specifications

The standard deviation of the noise amplitude is an important factor in our measurements. We characterize the signal-to-noise ratio (SNR) [15] by :

$$\frac{S}{N} = \frac{\text{Average signal value}}{\text{Noise standard deviation}} \tag{1.9}$$

Or in decibels [16] by

$$SNR_{dB} = 10\ log\left(\frac{Signal}{Noise}\right) \tag{1.10}$$

**Intrinsic** noise sources are a set of fluctuations in currents and voltages. They are present in any electronic system and arise from the Brownian motion of electrons and the discrete nature of electrical charges [17]. One of the major noises that can impact the quality of our nanoparticle sensor is thermal noise, also known as Johnson's noise or white noise [18], resulting from the agitation of charges in the conductor. This movement is directly proportional to temperature, and can be described by Nyquist's formula :

$$\overline{v_n^2} = 4k_bTR\Delta f\ [\text{V}^2] \tag{1.11}$$

where $\overline{v_n^2}$ is the variance of the voltage across the resistor, or noise power, $k_b$, Boltzmann's constant in joules per kelvin, T for temperature in kelvin, R for the resistance value in ohms and $\Delta f$ the frequency component expressing the bandwidth in hertz. It is called white, because it doesn't depend on frequency as such, but only on the width of the frequency range. In fact, the power spectral density is uniform over all frequencies of the passband [19].

### 1.1.2 Biosensors

Our project will eventually detect bacteria, and therefore falls into the category of biosensors. Biosensors are measuring devices that integrate a biological component such as an enzyme, an antibody, a plant or animal cell, a DNA fragment, lipids, with a physical transducer (an electrode, an optical fiber, a piezoelectric quartz, etc.) to generate a manipulable electrical signal [20].

After this, the signal undergoes processing and amplification. In some cases, signal conversion and electronics can be integrated together, notably in micro-sensor systems based on complementary metal oxide semi-conductor (CMOS) technology.

### 1.1.3 Examples of transduction

In order to best detect biological material, we need to transform the measurand into a manipulable signal. To achieve this, several techniques exist, either **destructive**, i.e. the sample is altered or degraded for analysis, or **non-destructive**, also known as NDT for non-destructive testing [21].

**Electrochemical detection** The electrochemical biosensor is a conventional sensing device that transforms biochemical events into electrical signals by means of conductive elements. This includes methods such as potentiometry, which measures the potential difference between two of these elements [22], amperometry, which evaluates the current resulting from the application of a voltage across the electrodes [23], as well as voltametry, which analyzes the corresponding voltage for a specific current [24] between these same electrodes [25, 26].

There iss also the measurement of the change in **impedance**, calculated as the ratio of a gradually increasing voltage to the change in current across a frequency spectrum. This measurement, also known as electrochemical Impedance Spectroscopy (IES), is one of the most important electrochemical techniques, measuring the impedance of the circuit [27].

**Piezoelectric detection** Biodetection is also possible thanks to the piezoelectric properties of certain materials, such as quartz, which enable them to polarize electrically in response to mechanical stress, and conversely, to deform when an electric field is applied. These two effects, known respectively as the direct piezoelectric effect and the reverse piezoelectric effect, are inseparable [28].

The vibratory frequency of a quartz crystal is inversely proportional to the root of its mass. A quartz crystal coated with enzymes, antibodies or other binders can thus be used as a microbalance, for example [29].

**Optical detection** One of the first optical detection techniques was fluorescence detection. It consists in « attaching » to the target sample a fluorescent chemical **label**, i.e. one that emits a light beam in a given spectrum. This spectrum is then measured to determine the concentration of the target sample [29, 30].

The simplest version of optical detection is sample colorimetry. Using a given marker or reaction, the color of the concentration can be altered according to the presence or absence of the target sample. It is not a very precise method, of course, but it does enable you to tell quickly whether or not, for example, a virus is present in a sample.

Another optical detection technique is interferometry, i.e. the measurement of interference between light waves (Fig. 1.4). One method is the Mach-Zehnder interferometer, in which a sample is placed in the path of one of the light waves produced by the same source, and the interference between the two is studied. The sample will modify in phase and/or amplitude the result on the interference spectrum, which will indicate the concentration of target biomolecules in the sample [30].

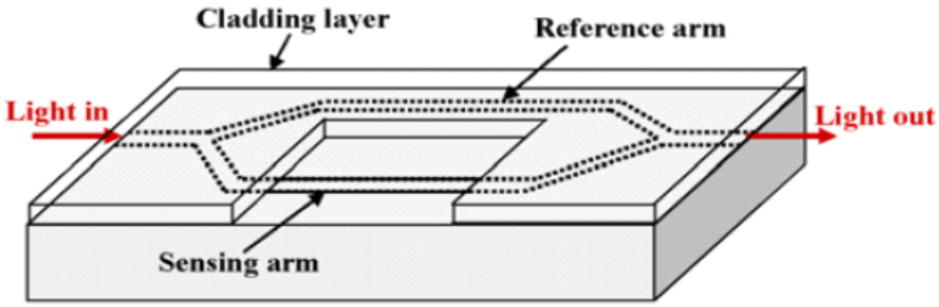


Figure 1.4 – Diagram of a biosensor based on the Mach-Zehnder interferometer[30]

**Magnetic biosensing** One of the last detections to be discussed in this section is magnetic biodetection. This type of detection involves **labelling** target biomolecules with magnetic particles. This particle, generally of the nanometer order, will alter the characteristics of the sample, for example by increasing or decreasing its impedance, and enable it to be detected via this change [30].

In particular, these particles can be detected by magnetoresistivity, i.e. by measuring the variable resistance of the sample when subjected to a magnetic field [31, 32].

Or the nanoparticle-labeled sample can be measured using the Hall effect, a phenomenon that occurs when a material is immersed in a magnetic field, generating a voltage in the material which can then be measured to determine the concentration of magnetic particles [33].

Some detection techniques require **labelling**, such as the ELISA (Enzyme Linked Immunosorbent Assay) [34] method, which detects an antigen or antibody in a sample via the enzymatic colorimetric reaction of the antigen-antibody reaction. But there are also **unlabelled** techniques such as interferometry [35].

### Lateral flow test and markers

To enhance the biosensor, the above-mentioned detection systems can be coupled with lateral flow assay (LFA), a test most often coupled with immunochromatography. This is one of the most modern, simple and rapid techniques for testing a given sample. The best-known examples are pregnancy tests and the COVID-19 self-test.

The standard (or sandwich) test, the most common and simplest, is based on the migration of a sample through a nitrocellulose membrane (Fig. 1.5). The membrane is loaded with nanoparticle-labeled bioreceptors that react with the desired analyte. By capillary action, the particles migrate to two reagent lines, the test line and the control line. The test line contains another bioreceptor which will react and attach to the first if it has previously bound to the target sample. The control line also contains another bioreceptor « attaching » to any bioreceptor, whether bound to the desired analyte or not. Different types of nanoparticles enable different types of detection. For example, AuNP enable red colorimetry when test and/or control lines are reached by the analyte and its bioreceptors [36].

Most LFA are purely qualitative (i.e. we only want to know if the biomolecule is present or not in the given sample), but some can be quantitative (to know the precise concentration of the target molecule) using the appropriate nanoparticle markers and detection devices [37].

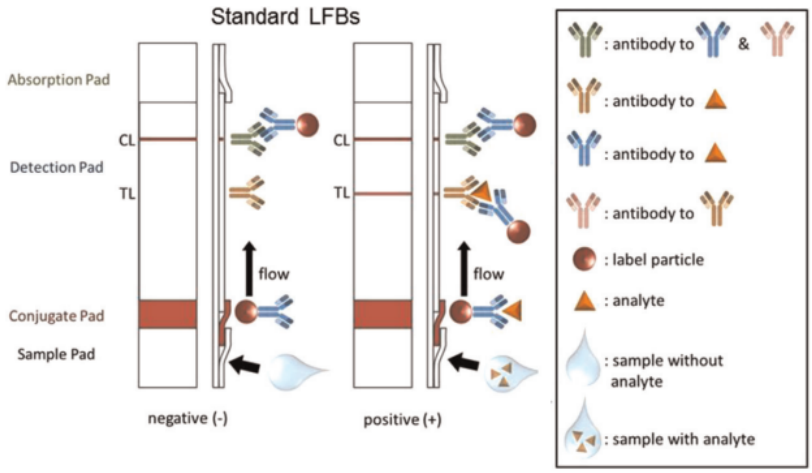


Figure 1.5 – Standard operation of a lateral flow assay [36]

The use of LFA is economical, fast and has two major advantages: the capillarity of cellulose enables the sample to be moved to a target zone without any energy input, and it is an excellent substrate for functionalization (i.e. making particles compatible to capture a desired biomolecule more easily) [7]. These qualities mean that this type of assay is greatly emphasized in biosensors point-of-care (POC), i.e. sensors that can be easily and quickly manipulated close to the patient [38, 39].

### 1.1.4 Differential detection

One of the techniques studied in the design of our biosensor is the « differential » assembly, a widespread technique in the world of sensors. The principle is based on detection via two different sensors, a reference sensor and a main sensor. To improve output processing, the two signals are subtracted to recover the difference. This type of arrangement has a number of applications, including noise reduction, improved selectivity and the possibility of obtaining a relative measurement.

#### Noise reduction

The differential circuit can be used to reduce additive noise defined as $e_n$ in (1.12), such as intrinsic noise produced by electron motion, or extrinsic noise such as environmental noise, power supply noise or noise from external electrical sources:

$$V_{out} = V_s + e_n \tag{1.12}$$

Where $V_{out}$ is the noise-damaged output signal and $V_s$, the useful signal. As can be seen, when the sensors and interface electronics are linear, the magnitude of the additive noise does not depend on the magnitude of the signal, and persists even when the signal is zero.

To improve the stability of the output signal in the face of transmitted additive noise, sensors are often arranged in pairs, in a differential configuration. One of the sensors (the main sensor) is exposed to the stimulus of interest, while the other (the reference sensor) is protected from this stimulus. The transmitted noise, known as common noise, affects both sensors identically. Subtracting the output signals of these sensors eliminates this additive common noise.

#### Improving selectivity

In some cases, such as electrochemical sensors, it is common practice to use several sensors to accurately measure the concentration of a gas. Indeed, some electrochemical sensors are

sensitive to two or more gases at the same time. As a result, the output signal from these sensors, a single value, contains the sum of the concentrations of the gases measurable by that sensor.

One technique for improving the selectivity of a gas sensor is to combine it with one or more other sensors to subtract the gases between them in order to recover the desired concentration. For example, AlphaSense's *OX-A431* [40] sensor captures both ozone ($O_3$) and nitrogen dioxide ($NO_2$). It is customary to use the *NO2-A43F* [41] sensor in parallel to subtract the $NO_2$ concentration measured by the second sensor from the first in order to recover the ozone concentration.

Another example is the measurement of infrared radiation via a pyroelectric transducer, a transducer with the ability to change its polarity under the effect of radiation [42]. The major problem with this type of detector is that it also has a piezoelectric effect, i.e. a certain sensitivity to mechanical vibrations and voltages. The differential circuit is a solution to this problem. By placing two pyroelectric sensors side-by-side, one of which is the main radiation sensor, and the other which serves as a stimulus-protected reference, the piezoelectric effect can be subtracted from the output signal to improve the overall selectivity of the detector.

### Relative measurement

Some detection techniques require the removal of an unnecessary part of the input signal. This is particularly the case in interferometric detection, where the differential setup enables direct recovery of the values impacted by the presence of the target sample, without having to manipulate the input signal. A concrete example is shown in Fig. 1.6.

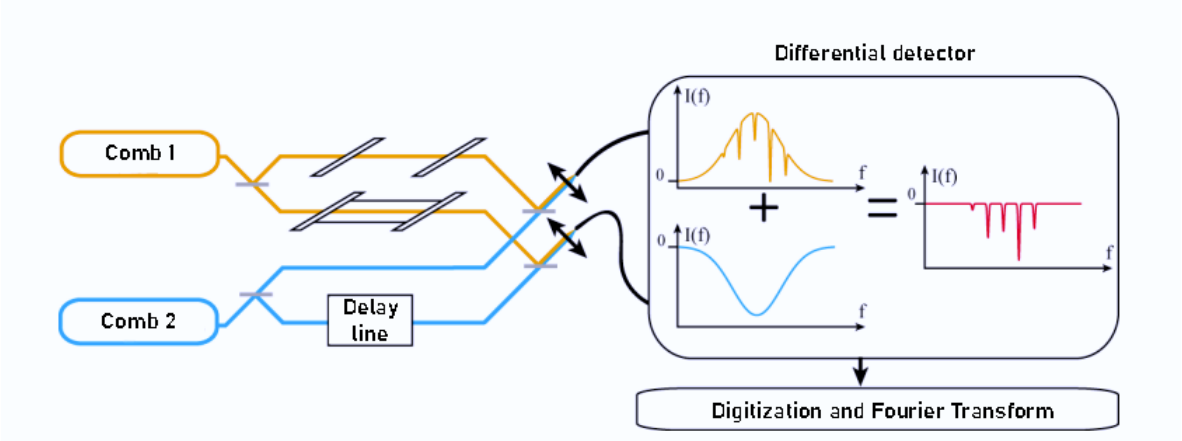


Figure 1.6 – Differential circuit diagram of two interferometers [43]

By subtracting the signal from the reference interferometer from the signal from the main interferometer, two identical interferometers can be used to recover the frequencies impacted by the presence of gas in the frequency domain [43]. This technique highlights an amplitude difference on two input signals, but it is perfectly possible to do the same to recover a phase difference [12].

## 1.2 Magnetic nanoparticles in biosensors

Most biosensors can be relatively improved by the use of nanoparticles, including magnetic nanoparticles (MNP). In particular, these nanoparticles are used in particular to label biological components (bacteria, DNA, viruses, etc.), improving detection both qualitatively and quantitatively. An example is gold nanoparticle (AuNP), which can be used for sample colorimetry and

amperometric detection [44].
A « nanoparticle » is defined as a particle with a size between 1 to 100 nm. At this scale, the particle possesses particular chemical, electrical and magnetic properties [45], with different types of potential applications.

After several studies by other students and PhD students [7, 6, 8, 46], one possible design is the addition of MNP in a LFA. This work takes place in the design of a magnetic nanoparticle sensor respecting the « ASSURED » standards dictated by World Health Organization : Affordable, Sensitive, Specific, User-friendly, Rapid and robust, Equipment-free and Deliverable to end-users.

This section focuses on magnetic nanoparticles, whose properties make them much more effective than other conventional detection methods for reading the concentration of a given sample.
Where, for example, an optical reading will only read the surface at a thickness of around 10 µm, marking with magnetic nanoparticles enables in-depth reading (Fig. 1.7) of the concentration of the sample, which can be between 150 and 200 µm thick [47]. As the lateral-flow test holder has no magnetic element, the contrast of the MNP readout is quite high, providing a much higher SNR than conventional detection methods such as optical detection, which can be affected by scintillation, absorption and/or autofluorescence within samples [48].

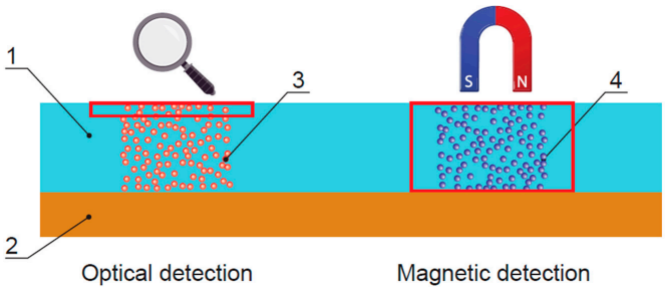


Figure 1.7 – Comparison between optical and magnetic reading (**1**) Contact membrane, (**2**) Plastic support (**3**) Latex or gold colloid particles, (**4**) Magnetic particles [47]

In addition to their attractive physical properties for detection, magnetic nanoparticles have the advantage of being economical to produce, stable and compatible with biological materials, depending on the type of nanoparticle used. Some of them, such as iron oxide, have an ecological dimension, and they continue to offer a non-invasive, non-destructive method of sample analysis [49].

### 1.2.1 Design

In order to be used to detect biological material such as bacteria or viruses, magnetic nanoparticles need to undergo various operations (Fig. 1.8) to be fully usable for biodetection.

First of all, we need to select the desired characteristics of our particle, choosing its size, the analyte at the center of detection, constraints such as the environment or available resources, and so on. Next, we need to produce the basic material, designing the shape and structure of our particle starting from a magnetic material such as gold or iron. The third step is to functionalize the nanoparticle. **Functionalization** focuses on chemically modifying nanoparticles to give them new properties to facilitate compatibility for its primary use : binding to a target

biomolecule to make it detectable via the properties of the magnetic nanoparticle. The final step is **bioconjugation**. From this new functional surface, particles acquire the ability to form a covalent bond with biomolecules for targeting purposes. Covalent conjugation refers to the formation of a strong chemical bond between nanoparticles and biomolecules, enabling the creation of complex assemblies capable of specifically targeting certain cells or molecules [50, 51].

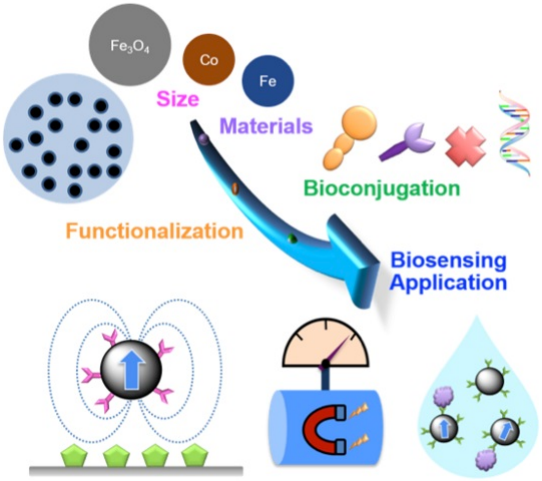


Figure 1.8 – Summary of the design of a magnetic nanoparticle for biosensing applications [52]

### 1.2.2 Toxicity

Of all the characteristics of magnetic nanoparticles, it is important to consider their potential toxicity. MPNs, mainly composed of transition metals, can release metal ions and generate reactive oxygen species, which can cause adverse effects. Exposure to nanoparticles can lead to inflammation, impaired mitochondrial function, DNA damage and severe toxicity at high doses. The coating of magnetic particles (MP) can limit the generation of reactive species. For example, iron oxide MP can be made biocompatible by coatings such as silica, gold or polyethylene glycol. The toxicity of particles depends on their size, chemical composition, surface charge and reaction with cells. Smaller nanoparticles have a larger surface-to-volume ratio and are therefore more chemically reactive than larger ones. Hydrodynamic size [53] also affects the interaction of MNP with biological systems. Coating and surface loading can modify this size and optimize the functionality of the MP. The interface between MP and biological systems is a crucial factor for nanoparticle biosafety. In conclusion, a suitable coating on MP, depending on their size and shape, will determine their interaction with biological molecules and their biocompatibility [52].

### 1.2.3 Magnetic properties

The detection of magnetic nanoparticles enables quantitative measurement of the concentration of the target sample via their functionalization. The various detection techniques are based on properties specific to all magnetic materials, but also to nanoscopic samples. Before reviewing the state of the art in magnetic detection techniques, it is worth defining some of the properties on which current magnetic detectors are based.

Magnetic susceptibility is the first property to be discussed. It refers to the magnetizing capacity of a material, and characterizes its behavior when interacting with a magnetic field. The second property highlighted is magnetic remanence, i.e. the characterization of the residual

magnetic field produced by magnetic nanoparticles after magnetic excitation of the material. This remanent field can last to a greater or lesser extent. The decrease in the remanent field over time is called magnetic relaxation. Then we have magnetoresistance : this property is defined as the variation in resistance of the material as a function, once again, of the external magnetic excitation to which it is subjected.

### Magnetic susceptibility

Magnetic susceptibility characterizes the magnetizing behavior of a material, i.e. its ability to become a magnet and generate its own magnetic field when subjected to an external field [54]. The Lorentz law of electromagnetic forces defines the magnetic field as one of the vector components exerting a force on an electric charge [55] :

$$\mathbf{F} = \underbrace{q\mathbf{E}}_{\text{Electric force}} + \underbrace{q(\mathbf{v} \times \mathbf{B})}_{\text{Magnetic force}} \tag{1.13}$$

with

— q : the electric charge of the particle [C]

— $\mathbf{F}$ : the force vector applied to the charge [N]

— $\mathbf{E}$ : the electric field [V/m].

— $\mathbf{B}$ : magnetic field [T]

— $\mathbf{v}$ : particle velocity vector [m/s]

If the electric field $\mathbf{E}$ $[\frac{V}{m}]$ can be seen as the force granting uniform displacement to our charged particle, then the magnetic field $\mathbf{B}$ $[T = V \cdot \frac{m}{s^2}]$ can be seen as the acceleration applied if this particle crosses a magnetic field perpendicular to its velocity. The field $\mathbf{B}$ varies as a function of its medium, and can be redefined by :

$$\mathbf{B} = \mu_0 \mathbf{H} \tag{1.14}$$

Where $\mu_0$ is defined as the magnetic permeability in vacuum, i.e. $4\pi \cdot 10^{-7}$ $[T \cdot \frac{m}{A}]$. The literature describes $\mathbf{B}$ as magnetic induction, and $\mathbf{H}$, measured in $[\frac{A}{m}]$, as the exciting or external magnetic field, in order to better differentiate them. $\mathbf{B}$ varies differently from $\mathbf{H}$ depending on the medium in which it evolves.

Magnetism, on the other hand, originates in the magnetic moments caused by the movement of electrons. These form tiny loops of current, called spins, which generate their own magnetic fields. This induction is explained by Lorentz's law (Eq. (1.13)). In most materials, these currents are randomly oriented and create no net magnetic field. However, in some materials, the application of an external magnetic field (generated by currents outside the material) can cause these loops to align themselves preferentially with the field, resulting in the addition of their magnetic fields to the external field. This is when the material is said to be magnetized [56].

Depending on the properties of the atoms making up the material, an additional magnetic field generated by the alignment of magnetic moments can be added to the external magnetic field. The total field in the material can be defined as [57] :

$$\mathbf{B}_m = \mathbf{B}_0 + \mathbf{B}_i \tag{1.15}$$

$B_0$ being the magnetic field in vacuum defined by the (1.14) and $B_i$ the field induced by the orientation of the magnetic moments under the constraint of the field $B_0$. By adding the property of **magnetic susceptibility** $\chi_m$ characterizing the magnetization of the material, we can redefine (1.15) by :

$$\mathbf{B}_m = \mu_0\mathbf{H} + \mu_0 \underbrace{\chi_m\mathbf{H}}_{\text{Magnetization}} \tag{1.16}$$

$$\mathbf{B}_m = \mu_0\mathbf{H}\ (1 + \chi_m) \tag{1.17}$$

where the second term is defined as the magnetization $\mathbf{M}$ of the same unit as the field $\mathbf{H}$ in $[\frac{A}{m}]$. In addition, magnetic permeability is defined by :

$$\mu = \mu_0(\chi_m + 1) = \mu_0\mu_r \tag{1.18}$$

as well as

$$\mu_r = \ (\chi_m + 1) \tag{1.19}$$

where $\mu_r$ is the **relative permeability** such that

$$B_m = \mu_0\mu_r H \tag{1.20}$$

We can characterize three great magnetic behaviors based on their magnetization relationship and magnetic susceptibility : diamagnetic, paramagnetic and ferromagnetic behavior. Two other behaviors, ferrimagnetic and antiferromagnetic, can be compared with ferromagnetic behavior, subject to certain differences, and will not be developed in this document.

**Diamagnetism** Diamagnetism characterizes materials composed of non-magnetic atoms, making them extremely insensitive to the external magnetic field (Fig. 1.9). Their magnetization is weak and opposed to the exciting magnetic field. Typical susceptibility values are of the order of $-10^{-5}$, such as gold with $-2.74 \cdot 10^{-6}$ susceptibility or copper with $-7.7 \cdot 10^{-7}$.
This behavior can be explained by **Lenz-Faraday's law**, which indicates that the temporal variation of a magnetic flux induces an electromotive force of the form :

$$\epsilon = -\frac{d\Phi}{dt} \tag{1.21}$$

This force resulting from the exciting magnetic field can be seen as the behavior of electrons tending to oppose the exciting magnetic field.

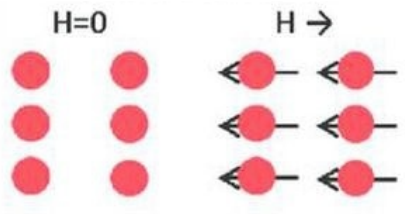


Figure 1.9 – Diamagnetic behavior of magnetic moments [58]

**Paramagnetism** In many cases, the magnetism of paramagnetic substances derives from the permanent magnetic moments of some or all of the constituent atoms or ions. When these moments have negligible interactions with each other and can orientate freely in any direction, we speak of free-atom paramagnetism. When a magnetic field is applied, the average direction of the moments is altered (Fig. 1.10), resulting in an induced magnetization parallel to the field. Magnetic susceptibility values generally range from $10^{-5}$ to $10^{-3}$.

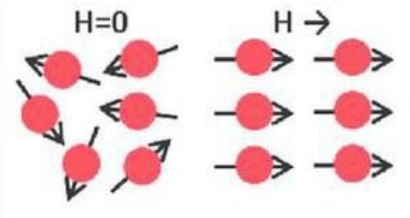


Figure 1.10 – Paramagnetic behavior of magnetic moments

**Ferromagnetism** Ferromagnetic behavior describes materials with interacting magnetic moments that tend to align with each other (Fig. 1.11a). These moments will therefore be more inclined to align themselves according to an external magnetic field. By removing this exciting magnetic field, the material's moments will retain their alignment and thus their magnetization. Some materials have a natural magnetization, such as magnetite ($Fe_3O_4$).

In addition to this remanent magnetization, ferromagnetic materials also possess **magnetic hysteresis**. When the material is magnetized, the relationship between **H** and **B** (or **M** according to the literature) is non-linear (i.e. the magnetic susceptibility $\chi_m$ varies as a function of **H**).
At a certain value $\mathbf{H}_{sat}$, the field inside the material is said to be saturated ($\mathbf{B}_{sat}$). When the exciting magnetic field is removed or reduced, the decrease in the field inside the material will not follow the same curve as its magnetization, a phenomenon known as hysteresis. In the absence of an external field, the material retains an induced field after magnetization, known as the remanent field ($\mathbf{B}_r$). In order to demagnetize the material, an external field must be applied which is the inverse of the induced field, known as the coercive field ($\mathbf{H}_c$). All this is illustrated in Fig. 1.11b.

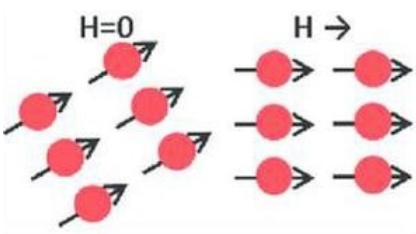


(a) Behavior of magnetic moments [58]

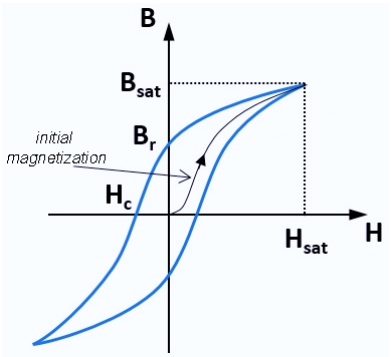


(b) Magnetic hysteresis cycle [59]

Figure 1.11 – Illustration of ferromagnetic behavior

### Magnetic relaxation and superparamagnetism

Introduced in 1949 by Louis Néel, **superparamagnetism** defines a particular state of ferromagnetic materials. This type of material, in the form of very small particles, may have the capacity to naturally reverse, i.e. to **relax**, naturally its magnetic moments under thermal energy input [60] towards a different magnetic orientation, known as easy magnetization, different from the exciting magnetic field, if the latter is present. In other words, if ferromagnetic particles, for example, are subjected to a magnetic field, their moments will align themselves according to the field. If the magnetic field is removed, the thermal energy required for a change in oscillation is sufficiently high to counteract the stored magnetic energy and thus reorient the particle in a direction other than that of the initial exciting field. This magnetic behavior can be likened to paramagnetic behavior.

Where ferromagnetic materials normally become paramagnetic above the Curie temperature (limit temperature at which the material's magnetic behaviour changes), nanoparticles will be considered superparamagnetic below this temperature. This property derives from the magnetic domains of the grains, which are so small, in the order of tens/centuries of nanometers, that they can be considered monodomain. The thermal energy required for this change is much lower in the nanoparticle domain, enabling a change in magnetization orientation in the material [61].

This phenomenon of demagnetization due to the reorientation of particles after removal of the exciting magnetic field is called **magnetic relaxation**.

### Hall effect

The Hall effect is an electromagnetic effect that describes the generation of voltage within a material through which a current flows in a magnetic field, the voltage generated being perpendicular to the field. This effect was discovered by Edwin Herbert Hall in 1879, and has given rise to numerous applications, including the detection of magnetic nanoparticles [62].
The Hall voltage is defined in relation to the width of the surface of the material immersed in the magnetic field :

$$\mathbf{V}_H = -w \cdot \ (\mathbf{v} \times \mathbf{B}) \tag{1.22}$$

### Magnetoresistance

The magnetoresistance (MR) is the property of certain materials that their resistance varies according to the applied magnetic field. Discovered at the same time in 1988 by two physicists, Albert Fret (France) and Peter Grünberg (Germany), they were awarded the Nobel Prize in Physics for their discovery, which has had a significant impact on current technologies. This phenomenon is at the root of our computers' hard disks, for example.
This relationship can be defined mathematically by the ratio :

$$\delta_H = \frac{R(H) - R(0)}{R(0)} \tag{1.23}$$

With R, the electrical resistance of the material and H, the exciting field. Three effects whose proportion $\delta_H$ exceeds several percent derive from magnetoresistance and are used in magnetic field detection technology : Giant magnetoresistance (GMR), Anisotropic magnetoresistance (AMR) and Tunnel magnetoresistance (TMR). These sensors use ferromagnetic thin films such as soft magnetic alloys with a thickness of less than 10 nm [62, 63, 64].

### 1.2.4 Detection techniques and examples

To round off this section on magnetic nanoparticles, here's a non-exhaustive and very brief overview of some possible detection techniques based on the effects previously highlighted.

#### Semiconductor-based

**Giant magnetoresistance (GMR) and spin valve** Giant magnetoresistance (GMR) uses alternating thin ferromagnetic and non-magnetic layers to amplify the magnetoresistance phenomenon (Fig. 1.12). This increasingly popular method offers improved sensitivity, portability and accuracy for medical detection [65].
A more advanced technology based on this principle is called spin valve detection, where manipulation of the magnetic field and magnetoresistance can modify the very spin of electrons across the structure. This method offers better characterization of nanoparticles, their concentration, but above all their magnetization. [66, 67].
These methods can improve the magnetoresistive variation by up to 20 % compared with just a few per cent for natural magnetoresistance, making it possible to measure nanoparticles as small as around twenty nanometers [52].

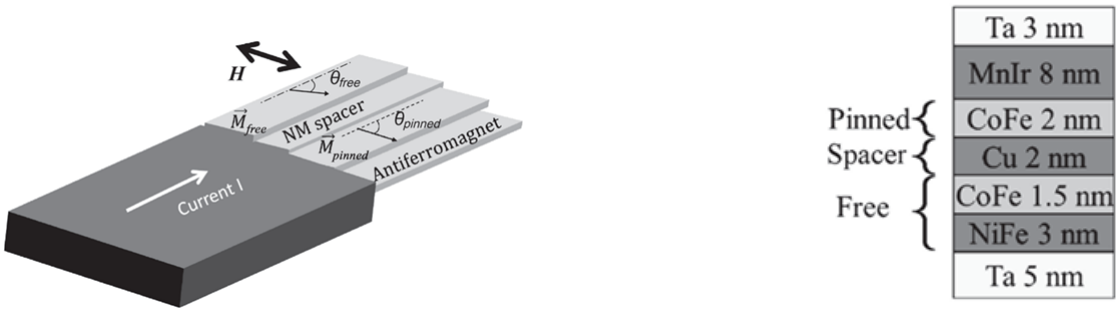


(a) Detector structure (b) Sensor layer

Figure 1.12 – Application based on the spin valve concept [62]

**Anisotropic magnetoresistance (AMR)** AMR is based on the variation of a material's resistance as a function of the angle of an exciting magnetic field. As with the other two effects of GMR and TMR, depending on the response of the resistance variation with respect to the angle of the magnetic field incident on the sample placed between two electrodes, the concentration of MNP can be measured using the anisotropic magnetoresistance [68] method. In the same range as the two previous magnetoresistance-based detection methods, the AMR is easy to set up and inexpensive, enabling the measurement of magnetic nanoparticles down to 20 nm.

**Tunnel magnetoresistance (TMR)** Tunnel magnetoresistance is another technique derived from the measurement of resistivity variation as a function of magnetic field. This technique is based on the quantum tunneling effect. An example of a possible detection method with TMR is based on a differential system of two Wheatstone (Fig. 1.13) bridge TMR fixtures [69]. A lateral flow assay (LFA) is immersed in a constant magnetic flux. This magnetic flux will impact the MNP and generate a tunnel magnetoresistance in the sensors on either side of the strip test line. Via the induced variation, we can then measure the concentration proportional to this variation [70]. This technique, like its counterpart, enables detection of magnetic nanoparticles down to less than 15 nanometres in diameter, thanks to magnetoresistance amplification of up to 70 %, or even 300 % for the most sophisticated machines. But this sophistication makes TMR

detection costly and less robust, since it is based on a quantum phenomenon that is sensitive to material imperfections and environmental conditions [52].

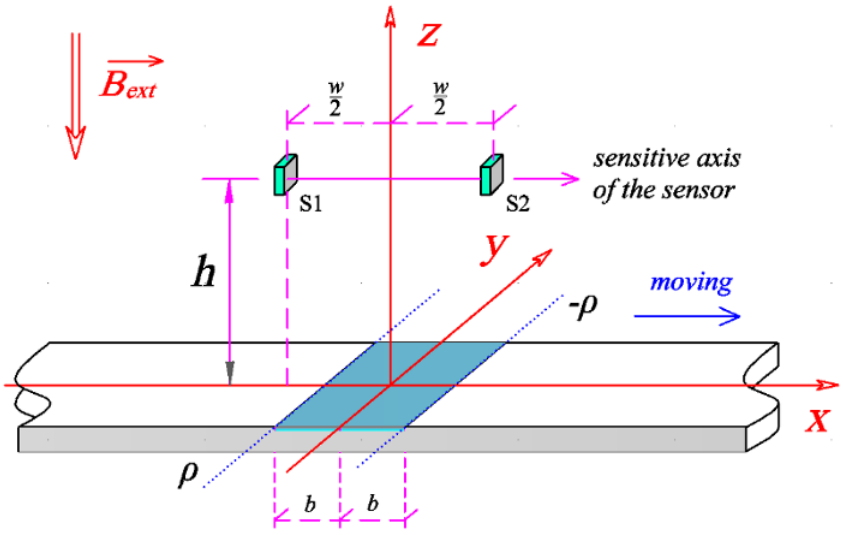


Figure 1.13 – Illustration of TMR differential detection assembly [70]

**Superconducting quantum interference device (SQUID)** The superconducting quantum interference device is a highly accurate low-frequency magnetic field detection system. It also detects relaxation, remanence and magnetic susceptibility. The SQUID operates on the basis of superconductivity and the Josephson effect. It consists of two superconductors separated by thin insulating layers to form two parallel Josephson junctions. The electric current flowing through these junctions depends on the phase difference between the wave functions of the superconductors. This phase difference is influenced by the magnetic flux through the SQUID. We can therefore measure our sample containing magnetic nanoparticles via the influence of the magnetic field on the current flowing through the SQUID. We can measure nanoparticles up to 20 nm in diameter, but unfortunately this detection system is expensive, requires experience in use and is not very portable [52, 71].

### Coil-based

**Search coil** One of the simplest techniques is to use the variation in magnetic susceptibility brought about by a magnetic material such as nanoparticles. The value of the inductance, and therefore the induced voltage, will vary according to the presence of the sample [72]. Like fluxgate, this technique is easy to set up and requires few resources.
What's more, it's possible to combine several magnetic nanoparticle parameters to detect and even characterize them. For example, researchers were able to easily highlight the concentration of 25 nm nanoparticles using a search coil set-up coupled to frequency mixing detection [73].

**Fluxgate sensor** Fluxmeter detection can be enhanced by using the saturation property of a ferromagnetic core (Fig. 1.14) by a first exciting coil, and then measuring the voltage induced by the variation in the total magnetic field in a second detection coil. In fact, magnetically saturating the core will induce a zero voltage in the detection coil, but if an external magnetic field is approached, this field will create a difference desaturating the material in certain directions (Fig. 1.15) [74, 75, 76].

This type of magnetometer can be used to measure the variation of magnetic fluxes produced by MNP in a sample, or to measure their magnetic relaxation. The system is affordable,

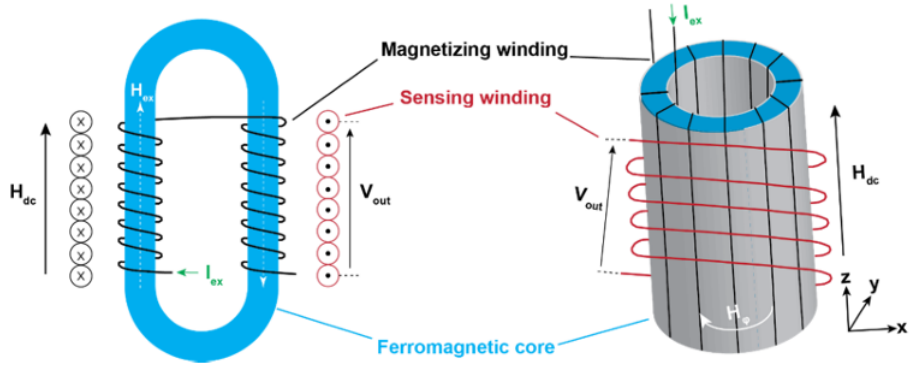


Figure 1.14 – Basic structure of a fluxgate magnetometer [74]

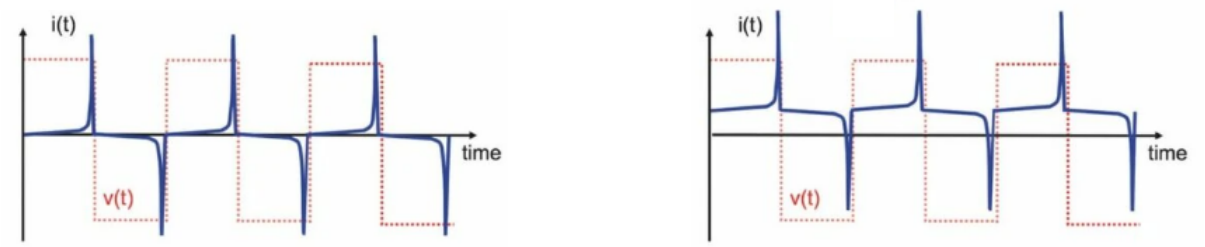


(a) Without sample (b) With sample

Figure 1.15 – Exciting signal and saturated output signal [77]

portable and still easy to manufacture. Detection is possible down to the hundred-nanometer level [52, 78, 79].

### Other means of detection

**Planar Hall Effect (PHE)** For the past twenty years or so, the Hall effect coupled to a microscopic substrate (Fig. 1.16) or CMOS technology has been used to detect the magnetic relaxation of superparamagnetic nanoparticles. Indeed, some techniques such as detection via SQUID are not sufficiently reactive to correctly measure the magnetic relaxation of magnetic nanoparticles, unlike some systems using the Hall effect [62, 80, 81, 82].

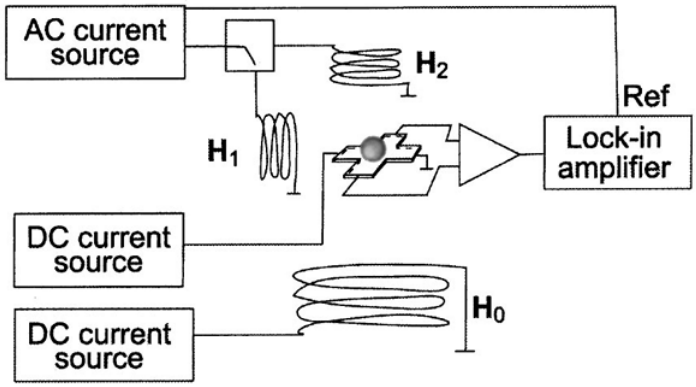


Figure 1.16 – Detection of a single superparamagnetic particle using the Hall effect [80]

**Switching detection by magnetic relaxation (MRS)** Derived from the principle of nuclear magnetic resonance (NMR) describing a phenomenon where certain atomic nuclei possess a magnetic moment sensitive to external excitation produced at a certain frequency, magnetic relaxation switching detection enables the detection of biological material by creating aggregations of particles around target samples and measuring their magnetic relaxation following external magnetic excitation. Despite good resolution down to 25 nm, this technique is not very affordable in terms of equipment POC [49, 83, 84].

**Magnetic detection techniques using frequency mixing** A detection technique based on magnetic resonance, where nanoparticles are excited at several frequencies, including the magnetic resonance frequency of the nanoparticles and a detection frequency. The contribution of magnetic nanoparticles will influence the output frequency, enabling us to measure its concentration. Nanoparticles as small as twenty nanometers can be detected, but this technique requires more or less expensive and less portable equipment [85].

**Non-electromagnetic detection** The above-mentioned detection techniques are just a small sample of all possible detection methods. Only detection methods based on magnetic or electrical phenomena have been mentioned, but magnetic nanoparticles can have many other applications than just inducing a voltage or influencing a nearby magnetic field. These include optical sensing such as plasmon-enhanced fluorescence [86], Raman spectroscopy [87], dynamic light scattering [88] or atomic magnetometry [89], but also mechanical sensing techniques such as piezoelectric or magnostrictive sensing [90, 91]. We won't even mention electrochemical impedance spectroscopy (*IES*), whose scope extends much further than simply measuring the concentration of magnetic nanoparticles, but whose presence can improve measurement [27, 92].

### Summary and comparison

Several detection methods have been put forward, but some do not meet the « ASSURED » standards defined earlier. Here's a summary Table 1.1 highlighting the various advantages and disadvantages of each detection technique.

| Technique | Sensitivity | Magnetic properties | Advantages | Disadvantages |
|---|---|---|---|---|
| GMR [65, 66, 67] | Up to 12.8 nm | Magnetoresistance | • Inexpensive<br>• Robust<br>• Good resolution | • Microfabrication |
| AMR [68] | Up to 50 nm | Magnetoresistance | • Inexpensive<br>• Robust | • Microfabrication<br>• Low resolution |
| TMR [69, 70] | Up to 12 nm | Magnetoresistance | • Good resolution | • Microfabrication<br>• Expensive<br>• Fragile |
| SQUID [71] | Up to 11 nm | Josephson effect | • Extremely sensitive<br>• High resolution<br>• Low-frequency | • Extremely expensive<br>• Complex (requires cryogenics, for example)<br>• Sensitive to external magnetic fields |
| Search coil [72, 73] | up to 25 nm | Relaxation and susceptibility | • Simple mounting<br>• Portable<br>• Low power consumption<br>• Good resolution if coupled with other techniques | • Sensitive to noise and other external interference<br>• Requires a combination of techniques to improve resolution |
| Fluxgate [74, 75, 76] | up to 100 nm | Relaxation and susceptibility | • Compact<br>• Portable<br>• Low power consumption<br>• Inexpensive | • Low sensitivity<br>• Sensitive to magnetic noise<br>• Non-linear |
| PHE [62, 80, 81, 82] | Up to 50 nm | Hall effect | • Robust<br>• Low power consumption<br>• Environmentally resistant (dust, humidity, etc.) | • Sensitive to magnetic noise<br>• Microfabrication |
| MRS [49, 83, 84] | Up to 21 nm | Relaxation | • Polyvent<br>• Possibility of coupling with magnetic resonance imaging | • Complex<br>• Limited resolution<br>• Sensitive to magnetic noise |
| Frequency mixing [85] | up to 20 nm | Relaxation and susceptibility | • Good sensitivity<br>• Versatile | • Signal processing<br>• Limited resolution<br>• Sensitive to magnetic noise<br>• Expensive |

Table 1.1 – Summary of the various techniques for detecting MNP

Bearing in mind that we need a system that is affordable, sensitive, specific, easy to use, fast, robust, requires no special equipment and can be used close to the user, we conclude that only fluxgate and search coil techniques are feasible. Indeed, any technique that is complex or requires microfabrication, which adds to the cost of the system and its development, should be avoided.

With this in mind, the study of a pair of search coil-type exciting and sensing inductors that can be easily printed on PCB was envisaged in order to study the variation in magnetic susceptibility brought about by magnetic nanoparticles.

## 1.3 Inductors

As we saw in the previous chapter, flux meters can be a simple and effective solution for measuring the concentration of magnetic nanoparticles for medical purposes. Based on the phenomenon of induction, which describes the relationship between the magnetic field and the voltage within a conductive material, inductors can be used for many applications, including the detection of magnetic nanoparticles. These inductors exploit the magnetic properties of nanoparticles to create measurable changes in magnetic flux, revealing their presence and characteristics.

With this in mind, the following section explores the fundamental principles of inductors, and introduces some of the theoretical concepts that are key to understanding the following chapters.

### 1.3.1 Electromagnetic reminders

As a reminder, the movement of an electron, the origin of current, is closely linked to magnetism. It was first put forward by Michael Faraday and Heinrich Lenz in the 1830s as the **Lenz-Faraday law** (Fig. 1.17b) describing the phenomenon of induction, i.e. the generation of an electromotive force $\epsilon$ inducing a displacement in electrons if they have the possibility :

$$\epsilon = -\frac{d\Phi}{dt} \ [\mathbf{V}] \tag{1.24}$$

With $\Phi$, the magnetic flux [Wb $= T \cdot m^2$], i.e. the magnetic field passing through a given surface (Fig. 1.17a) :

$$\Phi = \iint \mathbf{B} \cdot d\mathbf{S} \ [\mathbf{Wb}] \tag{1.25}$$

These laws explain the operation of electronic elements called inductors, i.e. components built around the principle of induction [56].

### 1.3.2 Induction

Induction is therefore defined as the generation of an electromotive voltage across an inductor immersed in a variable magnetic field. The value of the inductance can be defined as the ratio between the variation in magnetic flux and current, such that :

$$\epsilon = -\frac{d\Phi}{dt} = -L\frac{di}{dt} \ [\mathrm{V}] \tag{1.26}$$

The inductance value measured in Henry is therefore linked to the magnetic flux measured in Weber. The inductance value depends solely on the physical parameters of the structure (geometry, material, etc.) in which the current flows, since the magnetic field is directly

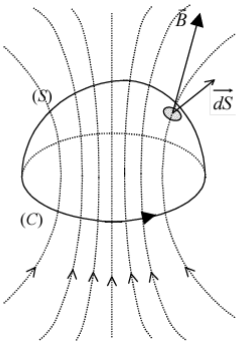


(a) Magnetic flux illustrated [93]

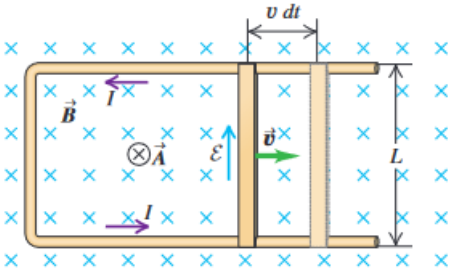


(b) Illustration of Lorentz and Lenz-Faraday laws. Displacement of a conducting bar generates an electromotive force perpendicular to the magnetic field [56]

Figure 1.17 – Illustration of electromagnetic laws

proportional to the current. If we add turns to this structure, the magnetic field intercepted is multiplied by the number of turns present. For example, N turns of length $l$ conducting a current I, of surface area S and generating a field will have the following inductance value [94] :

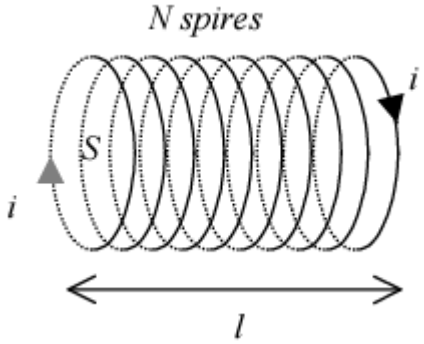


$$L = \frac{\mu_0 N^2 S}{l} \; [H] \qquad (1.27)$$

Figure 1.18 – Solenoid diagram [93]

As can be seen, $L$ depends not only on geometric parameters, but also on the magnetic permeability of the medium through which the magnetic field passes. Indeed, one way of improving the inductance value is to add a core within it, as illustrated Fig. 1.19, multiplying this value by the relative magnetic permeability $\mu_r$ of the inductor (Eq. (1.28)).

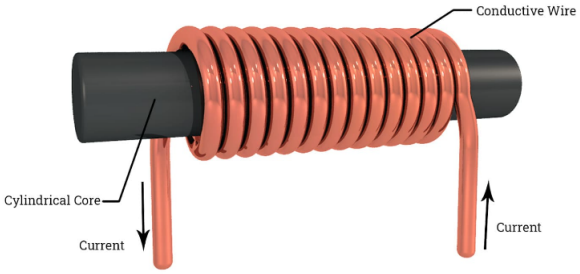


$$L = \frac{\mu_0 \mu_r N^2 S}{l} \; [\mathrm{H}] \qquad (1.28)$$

Figure 1.19 – Adding a magnetic core [95]

### 1.3.3 Mutual induction

If we add a second circuit of conductive turns not far from our first circuit, the second circuit will intercept the magnetic field $B_1$ of the first and generate its own current $i_2$. The current of the second circuit will then generate its own magnetic flux $B_2$, which will increase the value of its current, but will also be intercepted by the first circuit, which will also see its current $i_1$ increased (Fig. 1.20). This principle is called **magnetic coupling**.

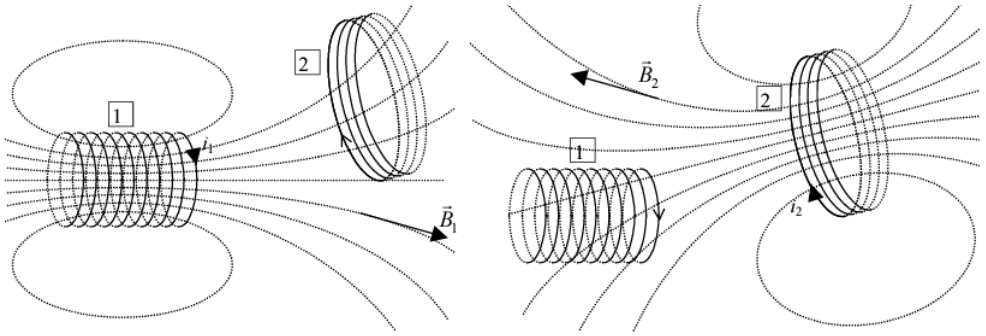


Figure 1.20 – Illustration of mutually intercepted magnetic field [93]

The flux generated by $i_1$ and intercepted by the second circuit is defined by $\Phi_{12} = B_1 S_2$ and, conversely, the flux generated by $i_2$ and intercepted by the first circuit is defined by $\Phi_{21} = B_2 S_1$. Or, by introducing the value of **mutual inductance** $M$ :

$$\Phi_{12} = M_{12} i_1 \tag{1.29}$$

$$\Phi_{21} = M_{21} i_2 \tag{1.30}$$

$$M = \frac{\Phi_{12}}{i_1} = \frac{\Phi_{21}}{i_2} \text{ [H]} \tag{1.31}$$

The value of mutual inductance $M$ measured in Henry, like $L$, depends only on the geometry and permeability of the total assembly, but can be negative, since the influence of one assembly on another can increase or decrease the current induced in the other, depending on the direction of the magnetic field, and therefore of the current.

Any additional flux variation captured by the inductor is a voltage contribution to the electrical system. If we place a second winding next to the first, the mutual inductance will influence the voltage of our initial assembly, and so on if we add $M$ assemblies. Each flux variation can be summed up as follows :

$$\epsilon_n = \frac{d\Phi_{0n}}{dt} + \frac{d\Phi_{1n}}{dt} + ... + \underbrace{\frac{d\Phi_{nn}}{dt}}_{\text{Auto-induction}} + ... + \frac{d\Phi_{Mn}}{dt} \text{ [Wb]} \tag{1.32}$$

With, as a reminder, $\Phi_{mn}$, the external magnetic flux $m$ intercepted by the $n$ assembly. For example, for mutual induction, we have :

$$v_1 = R \cdot i_1 + L\frac{di_1}{dt} + M\frac{di_2}{dt} \tag{1.33}$$

$$v_2 = R \cdot i_2 + L\frac{di_2}{dt} + M\frac{di_1}{dt} \tag{1.34}$$

We can define **the magnetic coupling coefficient** $k$ describing the mutual interception of magnetic fluxes by :

$$k = \frac{|M|}{\sqrt{L_1 L_2}} \tag{1.35}$$

With $L_1$ and $L_2$, the inductance values of the two circuits. A coupling worth 1 is an ideal case where the fluxes are mutually and totally intercepted such that :

$$M_{max} = \sqrt{L_1 L_2} \tag{1.36}$$

**Measuring mutual inductance** Mutual inductance can sometimes be difficult to quantify. A simple way of determining it in practice is via several measurements. Depending on the configurations available, several methods are possible [96]. Given $L_{total}$, the total inductance measured, $L_1$, the value of the first inductor in the system, $L_2$, the value of the second and $M$, the mutual inductance, we have, for a circuit where the currents flow in the same direction, indicated by a point located at the same level in Fig. 1.21, produce additive fluxes (Eq. (1.32)), called a **aiding** circuit:

$$L_{total} = L_a = L_1 + L_2 + 2M \tag{1.37}$$

And by the reciprocal in **opposing** montage :

$$L_{total} = L_o = L_1 + L_2 - 2M \tag{1.38}$$

Based on measurable values, as it is not always possible to have an accessible series/counter-series circuit or to have the measurement of self-inductances, we can easily determine $M$. For example, using the inductance values of series and counter-series circuits, if available :

$$M = \frac{L_a - L_o}{4} \tag{1.39}$$

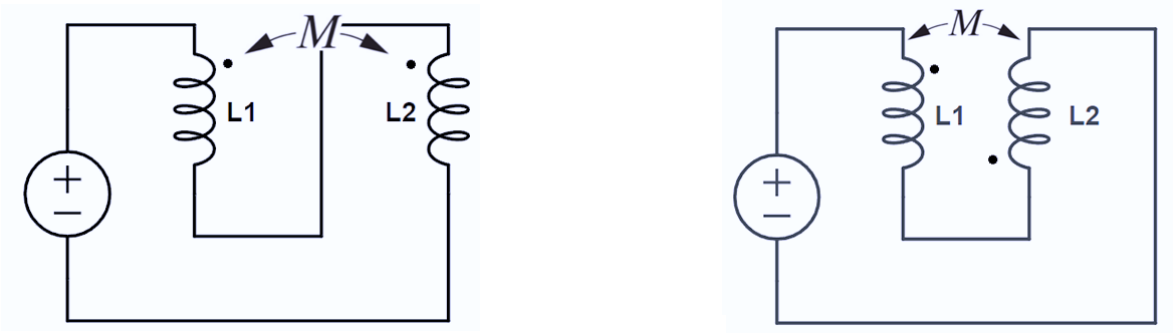


(a) Aiding montage

(b) Opposing montage

Figure 1.21 – Coil assembly for calculating mutual inductance [96]

# Chapter 2

# Objectives of this work

As part of the development of a bacteria biosensor to measure, among other things, water quality, several master's and doctoral theses are being written to study various possibilities for developing a device that complies with the « ASSURED » standards set by WHO. One of the avenues being explored is the use of magnetic nanoparticles coupled with a paper-based LFA to make the device as economical and practical as possible. The aim of this project is to develop a sensor capable of measuring the concentration of MNP in a given sample.

As we saw in the state of the art (Section 1.2.4), one simple and effective possibility would be to deploy a fluxmeter capable of measuring the magnetic **variation** induced by nanoparticle excitation. Based on the article [10] (Figure 2.1), the concept of **planar inductances** was put forward, combined with a differential system to capture the **voltage difference** produced by the excitation of MNP.

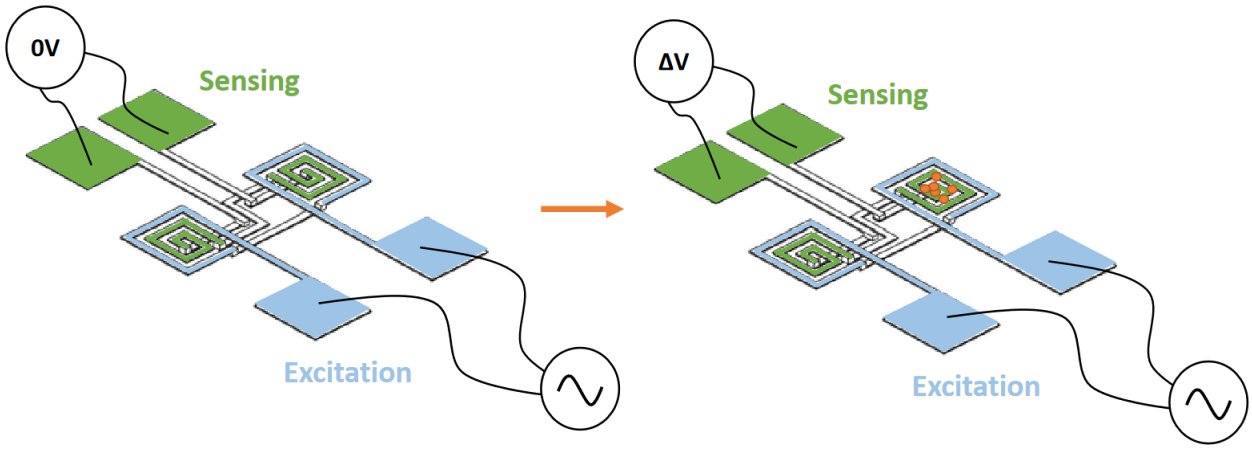


Figure 2.1 – Differential MNP sensor concept. Illustration by M. Hauwaert from [10]

Planar inductors, and more precisely, spiral and square inductors, offer the advantages of ease of manufacture, a certain robustness and simplified modeling of electromagnetic behavior. These characteristics put them in the forefront of the development of a simple, practical and economical sensor.

The aim of this work is therefore to investigate the potential applications of magnetic nanoparticles as sensors, to understand and control their behavior, and to highlight future possibilities for their use as functional biosensors.

The research will be divided into three parts :

1. The study of **planar inductors**, their characterization and behavior within a variable magnetic field will be outlined first. This section will focus on figures of merit and the

frequency response of the voltage induced by the external magnetic field (Fig. 2.2a).

2. We will then study the **pair of exciting/sensing inductors** that will make up half of the differential system. We will subject it to various ferromagnetic materials to study the variation induced by the introduction of these samples at the center of the sensitive inductor (Fig. 2.2b).
3. Finally, we will approach some prototype designs of **differential assemblies** based on the results of the previous two sections, to study their possible prospects for use. We will subject them to the same tests as the simple pair of exciting/sensing inductors, in order to compare the results of these assemblies as closely as possible (Fig. 2.2c).

Each section will highlight the equipment used and the results obtained. These will be discussed at the outset in each corresponding section. The work will conclude with a brief summary of the major observations and a discussion of possible prospects for the use of planar coils in a biosensor.

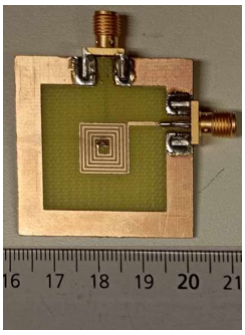


(a) First part : simple inductor

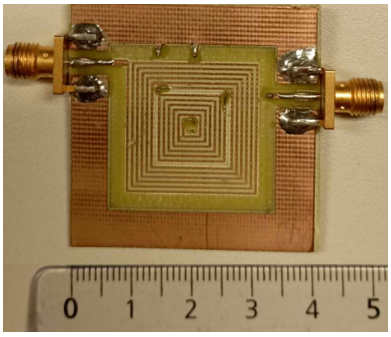


(b) Second part : pair of exciting/sensing inductors

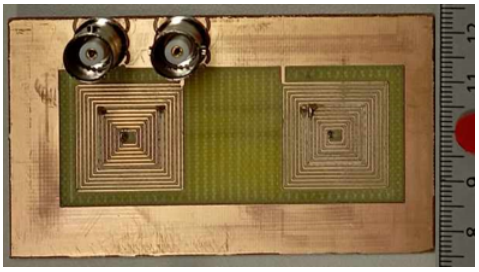

(c) Third part : Differential system

Figure 2.2 – The different parts of this research work

# Chapter 3

# Electromagnetic behavior of a square inductor

In this first chapter, before we start trying to detect magnetic nanoparticles, we first need to get to grips with the behavior of a single planar inductor. This first part will therefore highlight the theory characterizing planar inductances, followed by the various tools used to measure the parameters. We will use this to study the behavior of a square inductor printed on PCB in a controlled variable magnetic field. The electromagnetic response will then be studied and discussed at the end of the chapter.

## 3.1 Planar inductors

Planar spiral inductors are becoming increasingly popular, thanks to the ease with which they can be created on the market and their wide range of applications [97]. One notable area of study is their ability to measure the concentration of magnetic nanoparticles [98], and so are a highly suitable solution to our needs. If we can control the variation of electrical parameters in the presence of ferromagnetic samples, planar inductors are just the thing to be easily inserted into a robust, compact device manufactured for health purposes.

### 3.1.1 Structure and modeling

Inductors spread over a surface are referred to as planar, while spirals are used to describe the shape of a single wire winding on itself. These geometries allow for a number of mathematical simplifications, notably characterization via thickness, which is, by approximation, negligible in relation to other dimensions. Planar spiral inductors require at least two layers in order to be able to pass its output under its winding. Some examples of planar spiral inductors are shown Fig. 3.1.

In this study, we will confine ourselves to the description of **square** inductors. These have the advantage of being easy to design on PCBs, as well as generating certain simplifications due to the parallel nature of their branches.

#### Geometric parameters

These inductances can be modeled via six arbitrary parameters (Fig. 3.2) :

— $d_{out}$ : the outside diameter [m].

— $N$ : number of loops

— $s$ : the space between two loops [m].

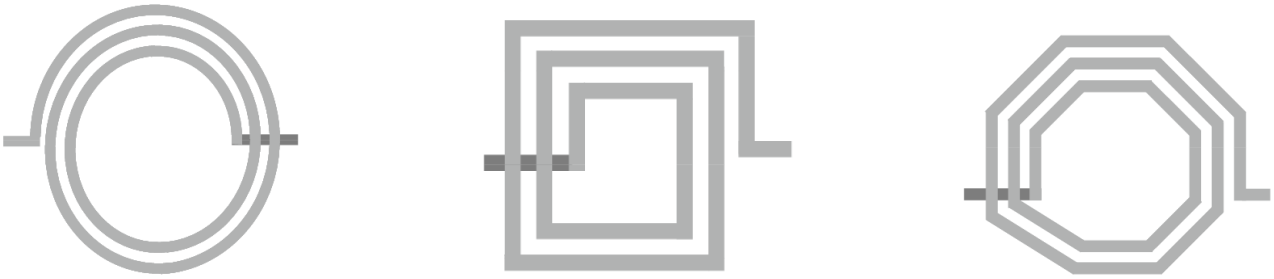

(a) Circular inductance (b) Square inductance (c) Octagonal inductor

Figure 3.1 – Different planar spiral inductances [99]

— $w$ : the bandwidth of a loop [m].
— $t$ : thickness [m]
— $\rho$ : material resistivity $[\frac{\Omega}{m}]$

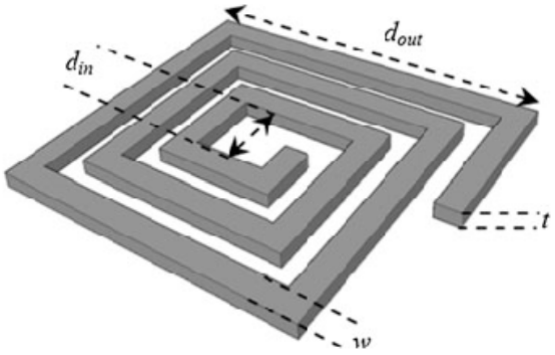


Figure 3.2 – Parameters of a planar square inductance [100]

From these parameters, we can derive other dimensions such as the length of the wire [101] making up the inductance :

$$l = 4Nd_{out} - 4Nw - (2N-1)^2(s+w) \tag{3.1}$$

We can also derive the inside diameter [102] :

$$d_{in} = d_{out} - 2[Nw + (N-1)s] \tag{3.2}$$

**Electrical parameters**

Our inductance, via its geometry, has electromagnetic parameters that can be determined by certain approximations. Its equivalent circuit is given Fig. 3.3 and is determined by its series resistance and inductance $R_s$ and $L_s$ and its parasitic capacitance $C_p$ arising from the capacitance between wires occurring significantly at high frequency.

From this model, we can derive the equivalent impedance :

$$Z_t = \frac{R_s + j\omega L_s}{1 + j\omega RC - \omega^2 LC} \tag{3.3}$$

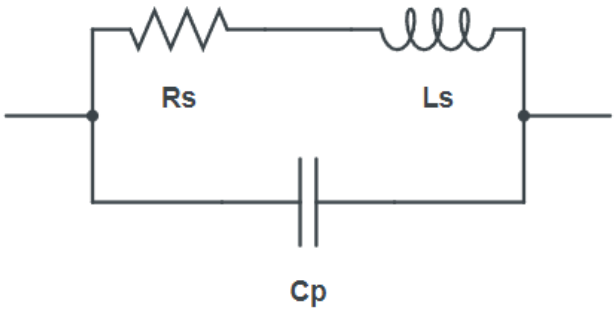


Figure 3.3 – Equivalent circuit of a planar inductor [99]

**Resistance** DC resistance can be calculated as follows [99] :

$$R_{dc} = \frac{\rho \cdot l}{w \cdot t} \tag{3.4}$$

At high frequencies, however, the conductor falls victim to skin [99] effects, a phenomenon caused by eddy currents tending to amplify the movement of electrons on the surface of the conductor and cancel it out at its center. (3.4) then becomes :

$$R_s = \frac{\rho \cdot l}{w \cdot \delta \cdot (1 - e^{\frac{-t}{\delta}})} \tag{3.5}$$

With the skin depth given by :

$$\delta = \sqrt{\frac{\rho}{\pi f \mu}} \tag{3.6}$$

As we have already explained, the skin effect occurs mainly at high frequencies (around ten MHz for our study), characterized by a distribution of current on the surface, with the conductor's resistance increasing as a function of frequency.

**Inductance** Its inductance is a little more complicated to calculate. Several models [103] have been established [104] but it's the Greenhouse model developed in 1974 [105] that remains the most widely used in the scientific literature. It is based on geometric approximations, such as the reduction of the wire to an infinitesimal thickness, and on equations solved numerically.

The model is given by the (3.7) :

$$L_s = \frac{\mu N^2 d_{avg} K_1}{2} \left[ ln(\frac{K_2}{\rho_r}) + K_3 \rho_r + K_4 \rho_r^2 \right] \tag{3.7}$$

With the following parameters and constants related to a square inductance. Other constants are determined numerically as a function of the shape of the indutance; here, we only specify those for a square inductance :

$$\begin{aligned} K_1 &= 1.27 \\ K_2 &= 2.07 \\ K_3 &= 0.18 \\ K_4 &= 0.13 \end{aligned} \tag{3.8}$$

With $d_{avg}$ and $\rho_r$ respectively the mean diameter and the fill ratio defined by :

$$d_{avg} = \frac{d_{out} + d_{in}}{2} \tag{3.9}$$

$$\rho_r = \frac{d_{out} - d_{in}}{d_{out} - d_{in}} \tag{3.10}$$

This modeling, based on numerical iteration, only works for inductances with an integer number of loops. Calculations are based on assumptions such as the length of an inductance arm being much greater than its width or thickness [106].

**Capacitance** For the parasitic capacitance $C_p$ produced by interaction between branches, between branches and substrate, and between superimposed circuits, several models and studies have been made to determine it [107]. We will simply formulate the parasitic capacitance of the circuit [108] by :

$$C_p = \frac{2l\epsilon_0}{\pi} ln\left(\frac{w + \frac{s}{2}}{\frac{s}{2}}\right) \tag{3.11}$$

With $\epsilon_0$ being the permittivity of vacuum and $\frac{1}{\mu_0 c^2}$ with $c^2$, the speed of light, $c = 3 \cdot 10^8$.

### 3.1.2 Specifications

Let's talk about the specifications of our planar inductor. As described in section 1.1, sensors have various limits, such as sensitivity, dynamic measurement range, saturation and so on. These limits are defined by both the geometric and electrical characteristics of our inductor.

**Theoretical sensitivity** The sensitivity of our detector, in a linear approximation model, can be described as the ratio between the magnetic field and the measured induced voltage. The article [109] gives us the sensitivity by extracting it from the Lenz-Faraday law (Eq. (1.24)) as :

$$s = \frac{V}{B} = \frac{2\pi S_{eq}}{\sqrt{(1 + \frac{R_s}{R_0})^2 + \left[(CR)^2 + (\frac{L}{R_0} - 2LC)^2\right]\omega^2 + (LC)^2\omega^4}} \tag{3.12}$$

With $R_0$, the load of the measuring device. As this is theoretically infinite for a voltmeter, (3.12) becomes :

$$s = \frac{2\pi S_{eq}}{\sqrt{(1 - \omega^2 LC)^2 + (\omega CR)^2}} \tag{3.13}$$

**SNR** We can calculate the theoretical SNR based on the geometrical parameters using (1.11) and (3.13) previously presented as :

$$SNR = \frac{s}{2\sqrt{k_B T \Delta f R}} = \frac{piS_{eq}}{\sqrt{(1 - \omega^2 LC)^2 + (\omega CR)^2}} \cdot \frac{1}{\sqrt{k_B T \Delta f R}} \tag{3.14}$$

We could translate each electrical component into geometric parameters, then maximize the formula to find out how each parameter behaves in relation to noise. Unfortunately, the study due to SNR will not be pursued further in this document [110].

**Measurement domain** Our measurement domain can be considered to extend from resistive noise to sensor saturation. But is the sensor saturable? We can assume that the only limits to the induced voltage are the physical limits of the copper used to design our sensor. For the lower limit, the resistive noise given by (1.11) gives us for an arbitrary resistance value between 1 Ω and the characteristic resistance of 50 Ω over a bandwidth ranging from 1 Hz to 1 MHz :

$$\overline{v_n} = \sqrt{4k_bTR\Delta f} = \sqrt{4k_bcdot293.15 \cdot 50 \cdot 10^9} \approx 1.27 \cdot 10^{-7} \text{ V} \tag{3.15}$$

This noise is a purely illustrative value to give us a certain detection limit for the magnetic field produced by our samples. In practice, there are many other factors besides resistive noise, such as external electromagnetic noise, voltage source noise and measuring instrument noise.

### 3.1.3 Figures of merit

Figures of merit represent the performance of a system. For the characterization of our inductor, we find the quality factor $Q$ describing the ratio between stored magnetic energy and lost energy, the max frequency $f_{Q_{max}}$ at which the factor $Q$ is maximum and the resonant frequency $f_{res}$ (or *SFR* depending on the literature) at which the parasitic capacitance and the induction balance [111, 99].

#### Q-factor

The quality factor Q will depend on the electronic parameters of our inductor and characterizes the energy utilization efficiency of our system as a function of frequency [112] :

$$Q = \frac{E_{stored}}{E_{dissipated}} = \frac{Im[Z_t]}{Re[Z_t]} = -\frac{\omega(C_pR_s^2 - L_s + C_pL_s^2\omega^2)}{R_s} \tag{3.16}$$

The figure of merit is maximum at a given frequency $f_{max}$, i.e. it is at this frequency that the inductance is most effective, and minimum at the resonant frequency $f_{res}$ and takes the form shown Fig. 3.4a.

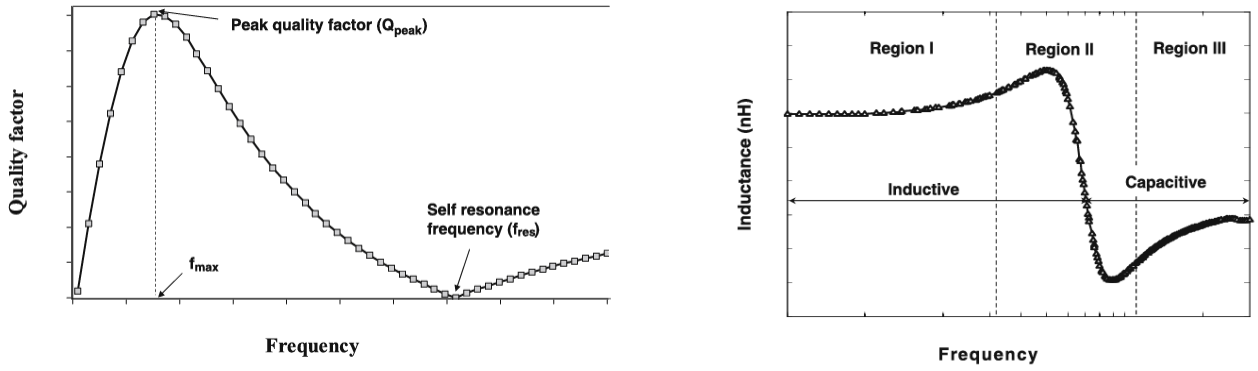


(a) Quality factor modeling $Q$

(b) Modeling apparent inductance as a function of frequency

Figure 3.4 – Illustration of figures of merit [99]

**Resonance frequency**

This frequency characterizes RLC circuits such as :

$$f_{res} = \frac{1}{\sqrt{L_s C_p}} \tag{3.17}$$

At resonant frequency, impedance is at a maximum, but for all frequencies above this, parasitic capacitances override the system's inductance, making it capacitive. Above this frequency, most simplified models no longer prevail.

In practice, the inductance value of the system is not constant, only its self-inductance, i.e. the inductance defined by the physical parameters of the system, is constant, but the apparent inductance, depending both on the current flowing in the system and the magnetic field intercepted by the inductor, is frequency-dependent (Fig. 3.4b).

### 3.1.4 Parameters influence

Thanks to [113] highlighting the optimization of parameters for the design of a planar spiral inductor **circular**, we can, by analogy, understand the impact of the parameters of a coil **square** on the quality factor and on the inductance, thus allowing us to best design optimized square inductors.

The various parameters vary one by one, leaving the others at fixed values : $d_{in} = 40$ µm, $w = 20$ µm, $s = 10$ µm and $N = 2.5$ loops. We will confine ourselves to a purely qualitative analysis.

**Number of loops** $N$

As shown in (3.7), the number of turns quadratically increases the number of times the self-magnetic flux is intercepted by the inductance, the higher the number of turns, the higher the inductance (Fig. 3.5b). Figure 3.5a shows the effect of the number of turns on the quality factor.

Increasing the number of turns lengthens the spiral inductor, resulting in an increase in the parasitic capacitance between inductor and substrate, thus contributing to a reduction in the quality factor. On the other hand, a large surface area implying a large inductance also implies a higher resonant frequency.

Furthermore, we note that the Q factor does not rise once the resonant frequency is passed, contrary to Fig. 3.4a. The Q-factor is defined as absolute, and theoretically becomes negative after the resonant frequency, if we rely solely on the study of inductance. Some literature therefore decides not to display the Q factor beyond the resonant frequency, as this reflects the capacitive nature of the system under study.

**Inside diameter** $d_{in}$

Increasing the inside diameter directly increases the surface area, increasing parasitic capacitive effects and reducing the quality factor spectrum (Fig. 3.6a). On the other hand, a larger surface area provides greater inductance (Fig. 3.6b).

**Space between loops** $s$

Increasing the space between the loops increases the surface area intercepting the magnetic flux, and as with the other parameters, it increases the value of the inductance (Fig. 3.7b).

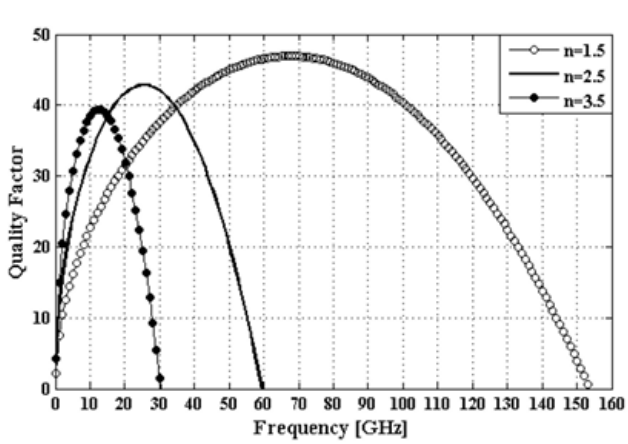


(a) Variation in $Q$

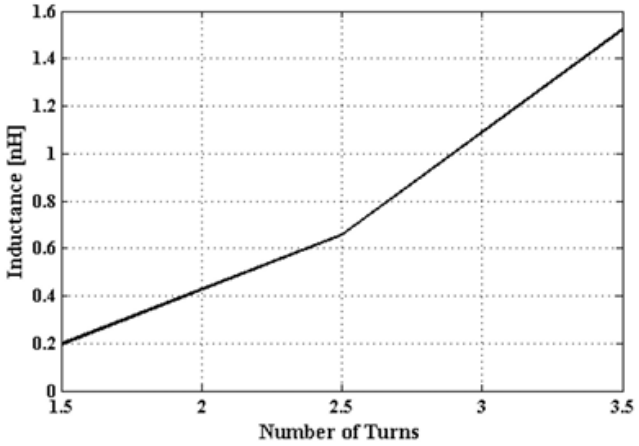


(b) Inductance variation

Figure 3.5 – Variation on N worth 1.5, 2.5 and 3.5 loops with $d_{in} = 40$ µm, $w = 20$ µm and $s = 10$ µm

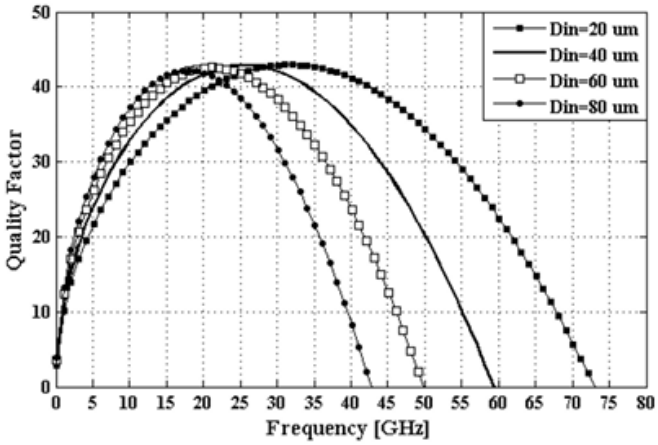


(a) Variation in $Q$

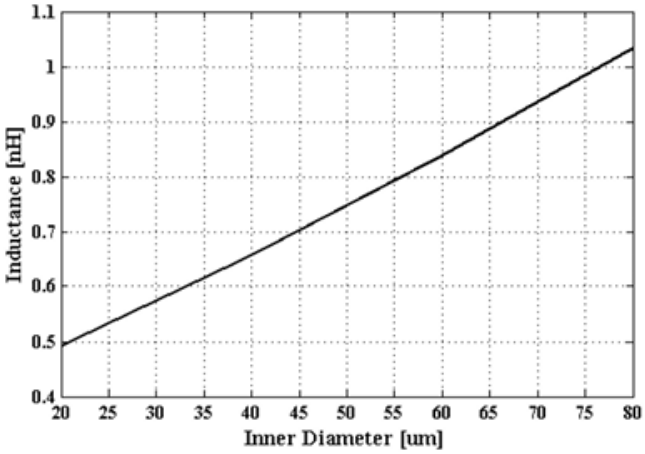


(b) Inductance variation

Figure 3.6 – Variation on $d_{in}$ worth 20, 40, 60 and 80 µm with $w = 20$ µm, $s = 10$ µm and $N = 2.5$ loops

On the other hand, the $s$ parameter does not significantly change the $Q$ factor. Varying the space $s$ only results in an increase in length, and therefore an increase in resistivity, as well as an increase in parasitic capacitance. This in turn reduces the quality factor (Fig. 3.7a).The small variation of the Q factor with respect to the $s$ space indicates that the parasitic capacity is greater between the branches and the substrate, or between the superposition of branches passing over or over each other, than the parasitic capacity between spiral inductors.

**Wire width** $w$

Reducing the inductance wire width (Fig. 3.8a) results in a spread and a reduction in quality factor. A wider wire width means less resistance (Eq. (3.4)), and therefore fewer resistive losses at low frequencies. As shown in Fig. 3.8b, this reduction in wire width, and therefore resistance, leads to an increase in inductance. As a result of these facts, we end up with a more constant quality factor over the frequency band with a high wire width, but we obtain a better quality factor over a smaller spectrum at low frequencies if we reduce this width.

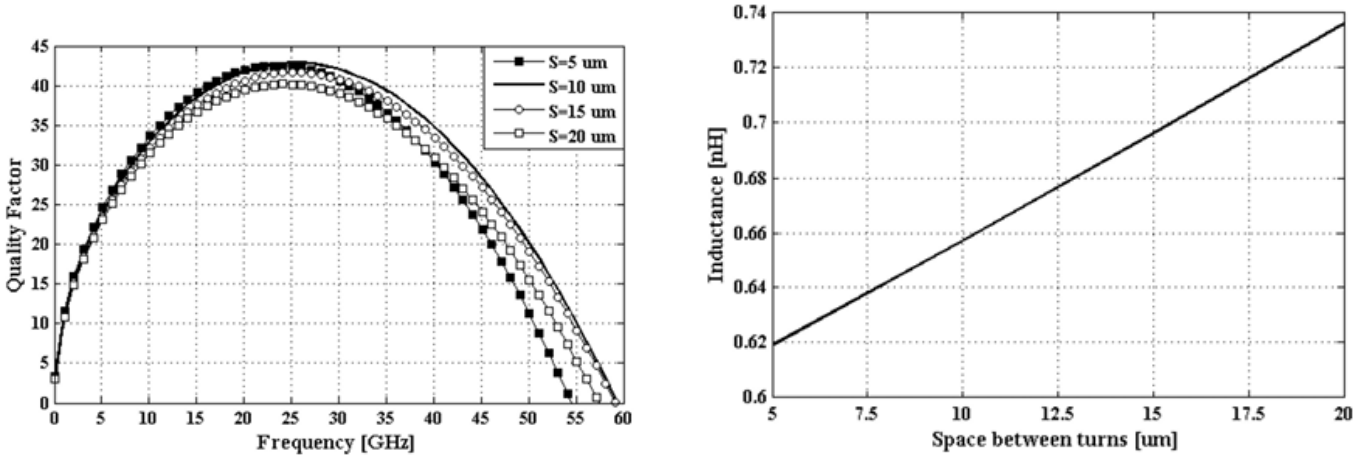


(a) Variation in $Q$ (b) Inductance variation

Figure 3.7 – Variation on $s$ worth 5, 10, 15 and 20 µm with $d_{in} = 40$ µm, $w = 20$ µm and $N = 2.5$ loops

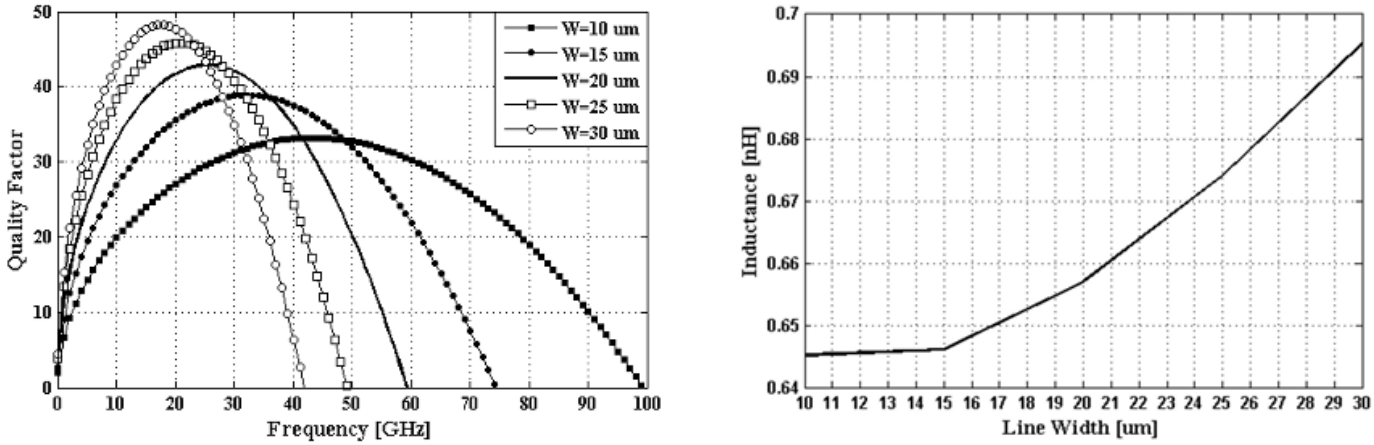


(a) Variation in $Q$ (b) Inductance variation

Figure 3.8 – Variation on $w$ worth 10, 15, 20, 25, et 30 µm with $d_{in} = 40$ µm, $s = 10$ µm and $N = 2.5$ loops

In conclusion, if you want to quickly increase the inductance value, you need to increase the number of loops of the coil, but this will have the effect of reducing the quality factor. A wide wire width reduces the resistivity of the track, resulting in a higher quality factor and increased inductance.

## 3.2 Material

Several tools will be used to characterize our sensitive inductance : first of all, we will use Helmholtz coils to fully control the magnetic field incident on the inductance, then the magnetic field will be measured using a Hall probe to check that the field is well controlled on our inductance, which will be connected to a multifunction meter including a Lock-In amplifier. All inductances will be characterized using a VNA.
Some of these devices will be used throughout the study to monitor and study the various behaviors of our systems.

### 3.2.1 Helmholtz coils

Helmoltz coils are an assembly of two circular coils arranged face to face (Fig. 3.9) to generate a uniform magnetic field at its center. They are notably used to counteract the Earth's natural magnetic field to create a neutral volume [114].

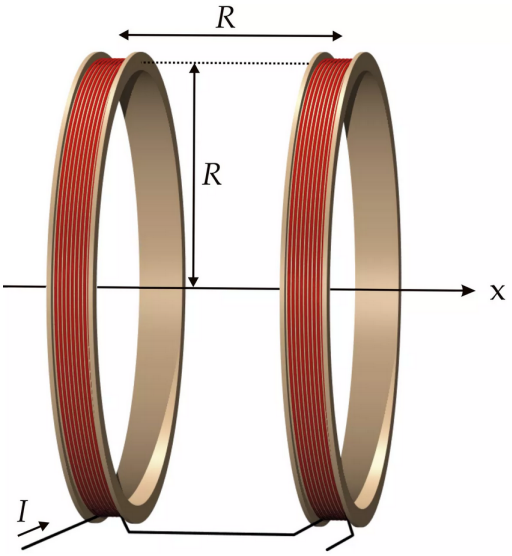


(a) Coil diagram [115]

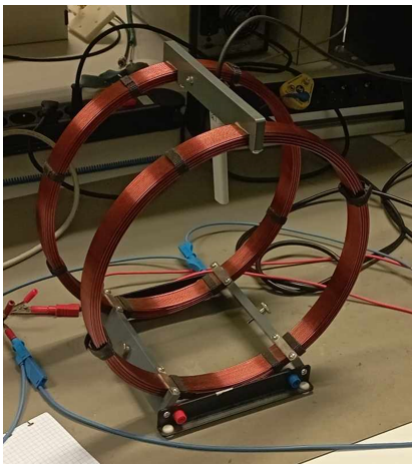

(b) Picture of laboratory coils

Figure 3.9 – Helmholtz coils

The coil datasheet **B Scientific® Physics** *3U8481500* tells us that for an average radius of $\approx$ 15 cm, with a gap of the same size between the two coils and 124 loops per inductance, we get 1.2 Ω per coil. The magnetic field, as a function of current, and with the given parameters, is according to datasheet [116] :

$$\begin{aligned} B(I) &= \left(\frac{4}{3}\right)^{\frac{3}{2}} \cdot \mu_0 \cdot \frac{N}{R} \cdot I \text{ T} \\ B(I) &= 7.433 \cdot 10^{-4} \cdot I \text{ T} \end{aligned} \tag{3.18}$$

### 3.2.2 Hall probe

To measure the magnetic field generated by the coils and confirm Eq.(3.18), we use the three-axis Hall effect magnetometer probe *THM1176-LF* (Fig. 3.10) from **Metrolab®** [117], capable of measuring variations of up to 8 mT with a resolution of 2 µT and an accuracy of $\approx \pm$ 20 µT. The probe can be positioned to measure the magnetic field at the center of the coils on its axis, thanks to a hook located on the structure of the Helmholtz coils (Fig 3.9b). The probe has a built-in acquisition system enabling communication with a computer at a frequency of up to 2300 samples per second.

Figure 3.10 – Hall effect probe

### 3.2.3 MFLI

The Multifunction Device with Lock-In Amplifier or MFLI (Fig. 3.11) from **Zurich Instruments®** offers, in addition to digital synchronous latching detection, voltage and current measurement, as well as the generation of oscillating signals up to 5 MHz.


Figure 3.11 – MFLI device

Synchronous detection [118, 119] is an amplification technique which, via a reference signal synchronized with the input signal, enables the latter's amplitude and phase to be recovered despite the very high noise impacting it (Fig. 3.12). The input signal and output signal are of the theoretical form :

$$s(t) = V_s cos(\omega_s t + \phi_s) \tag{3.19}$$
$$r(t) = V_r cos(\omega_r t + \phi_r) \tag{3.20}$$

In practice, the input signal is distorted by noise, hence the interest of the Lock-in amplifier, and may include several other frequency components, but the principle remains the same. The only condition is that the input signal must be a periodic signal whose amplitude and phase shift relative to the reference signal are to be extracted.

By multiplying the two signals that allow us to down-convert our signal to DC frequencies (Fig. 3.13a), we obtain :

$$s(t)r(t) = \frac{V_s V_r}{2} cos([\omega_r - \omega_s]t + \phi_s - \phi_r) + \frac{V_s V_r}{2} cos([\omega_r + \omega_s] + \phi_s + \phi_r) \tag{3.21}$$

We can quickly see that at the same frequency $\omega_s = \omega_r$, and by applying a filter (Fig. 3.13b), we can easily recover the amplitude (Fig. 3.13c) and phase of our input signal :

$$\frac{V_s V_r}{2} cos(\phi_s - \phi_r) \tag{3.22}$$

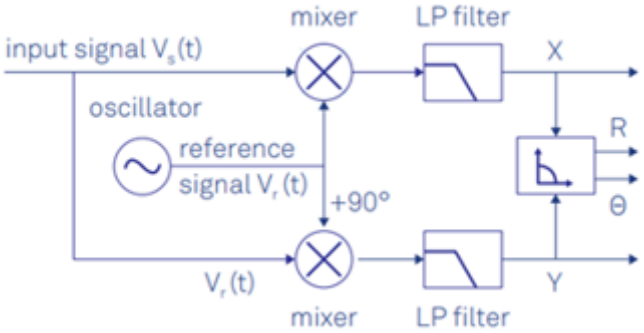


Figure 3.12 – Lock-in amplifier system diagram

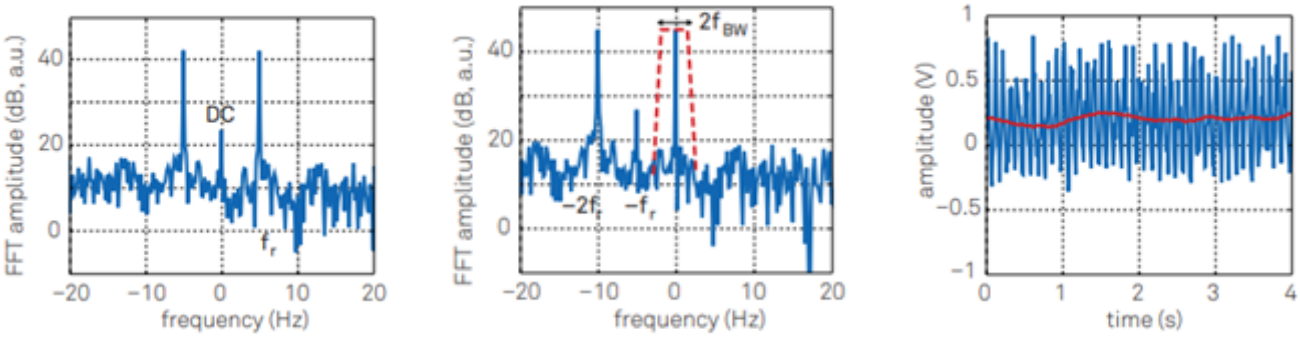


(a) Frequency spectrum of input signal

(b) Frequency shift 0 Hz and low-pass filter

(c) Temporal low-pass filter

Figure 3.13 – Illustration of the lock-in amplifier principle [119]

Note that the bandwidth and order of the low-pass filter will determine the extent of noise reduction and the filter response time. In a measurement context, one can afford to have a narrow bandwidth and a high order.

### 3.2.4 VNA

A vector network analyzer (VNA) is a measuring device for recovering the **amplitude** and **phase** of a system's S parameter via one or two ports over a given frequency range. For the purposes of this work, we will be using the *ENA E5061B* device from the **Keysight®** brand, which has the ability to scan the spectrum from 5 Hz to 3 GHz. This VNA is used each time after a calibration made with the kit **Anritsu®** *3652-series*.

When using the scattering parameters, or S-parameter, to perform a two-port measurement using a VNA, we can retrieve the impedance values $Z$ of the components connected to it. The S parameter is a matrix that describes the linear behavior of the device under test (DUT) through its ports, two for our situation, taking into account the coefficients of incident, reflected and transmitted waves at different frequencies. More precisely, for a two-port DUT, we have :

where the matrix S is composed of four elements :

— $S_{11}$ : the coefficient of the wave from port 1 of the DUT reflected back to port 1

— $S_{12}$ : the transmission coefficient from port 1 to port 2

— $S_{22}$ : the reflection coefficient of port 2

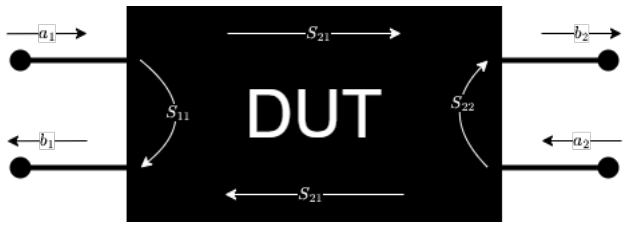


$$\begin{bmatrix} b_1 \\ b_2 \end{bmatrix} = \begin{bmatrix} s_{11} & s_{12} \\ s_{21} & s_{22} \end{bmatrix} \cdot \begin{bmatrix} a_1 \\ a_2 \end{bmatrix} \quad (3.23)$$

Figure 3.14 – Equivalent diagram of S-parameter

— $S_{21}$ : transmission coefficient from port 2 to port 1

To obtain the impedance Z of the DUT, we start with the parameter Z defined as :

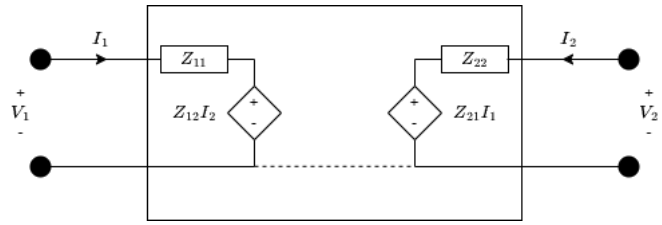


$$\begin{bmatrix} V_1 \\ V_2 \end{bmatrix} = \begin{bmatrix} Z_{11} & Z_{12} \\ Z_{21} & Z_{22} \end{bmatrix} \cdot \begin{bmatrix} I_1 \\ I_2 \end{bmatrix} \quad (3.24)$$

Figure 3.15 – Equivalent circuit for Z-parameter

$$Z_{11} = \frac{(1+S_{11})(1-S_{22})+S_{12}S_{21}}{(1-S_{11})(1-S_{22})-S_{12}S_{21}} Z_0 \quad (3.25)$$

$$Z_{12} = \frac{2S_{12}}{(1-S_{11})(1-S_{22})-S_{12}S_{21}} Z_0 \quad (3.26)$$

$$Z_{21} = \frac{2S_{21}}{(1-S_{11})(1-S_{22})-S_{12}S_{21}} Z_0 \quad (3.27)$$

$$Z_{22} = \frac{(1-S_{11})(1+S_{22})+S_{12}S_{21}}{(1-S_{11})(1-S_{22})-S_{12}S_{21}} Z_0 \quad (3.28)$$

Using the values of the Z parameters, we can determine the input impedance $Z_{in}$ and output impedance $Z_{out}$ of a DUT composed of two independent exciting/sensing inductors (Eq. (3.29) and (3.30)). This type of reading can be considered as a double reading at a single port, with $Z_{in}$ corresponding to the reading of the inductor connected to port 1 and $Z_{out}$, the reading of the inductor connected to port 2.

Alternatively, we can recover the parameters of the equivalent circuit in « T » if the circuit is said to be reciprocal and therefore $Z_{12} = Z_{21}$ (Fig. 3.16. Since our system is passive, the circuit is reciprocal, so we can determine the through impedance $Z_{th}$ (Eq. (3.31)).

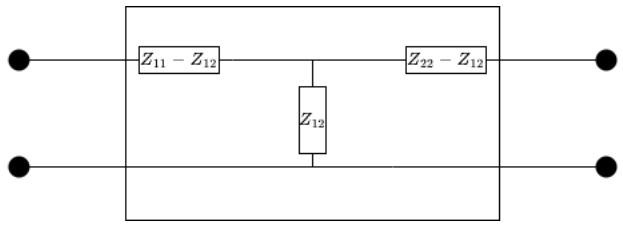


Figure 3.16 – Equivalent $T$ circuit

$$Z_{in} = Z_{11} - \frac{Z_{12}Z_{21}}{Z_{22}+Z_0} \quad (3.29)$$

$$Z_{out} = Z_{22} - \frac{Z_{12}Z_{21}}{Z_{11}+Z_0} \quad (3.30)$$

$$Z_{th} = Z_{11} + Z_{22} - 2Z_{12} \quad (3.31)$$

With $Z_0 = 50\ \Omega$, the characteristic impedance of the VNA input ports.

Thus, S-parameters provide a powerful approach to characterizing and analyzing RF [120, 121, 122] circuits and components.

## 3.3 Printed inductor

The coils are printed on a substrate **FR4**, a material used for printed circuit boards, fire-retardant in epoxy resin and reinforced with fiberglass and suitable for single- or double-layer PCB with good adhesion to **copper** [123].
The maximum resolution of the printer used is **0.4 mm**, this constraint will be our limiting dimension for designing our inductors. The connectors used will either be of the type **BNC** type, limited when venturing into high frequencies such as 3 GHz, or the **SMA** type, which is much more stable than the BNC type and therefore more suitable for frequency analysis, notably with the VNA [124].

### 3.3.1 Specifications

The first printed sensitive coil (Fig. 3.17) serves as a reference for the next prints presented in this work. It has arbitrary parameters (Table 3.1) whose only constraints are to have an integer number of loops $N$ for Greenhouse's formula to be applicable (Eq. (3.7)) as well as a size suitable for future implementation in a biosensor POC. This sensitive inductor is intended to be surrounded by a larger excitation inductor at a later date.

| $d_{out}$ [mm] | $d_{in}$ [mm] | N | $s$ [mm] | $w$ [mm] | $t$ [µm] | $\rho$ [$\Omega m$] |
|---|---|---|---|---|---|---|
| 11.2 | 2.4 | 6 | 0.4 | 0.4 | 18 | $17{\cdot}10^{-9}$ |

Table 3.1 – Dimensions of the first printed sensitive inductor

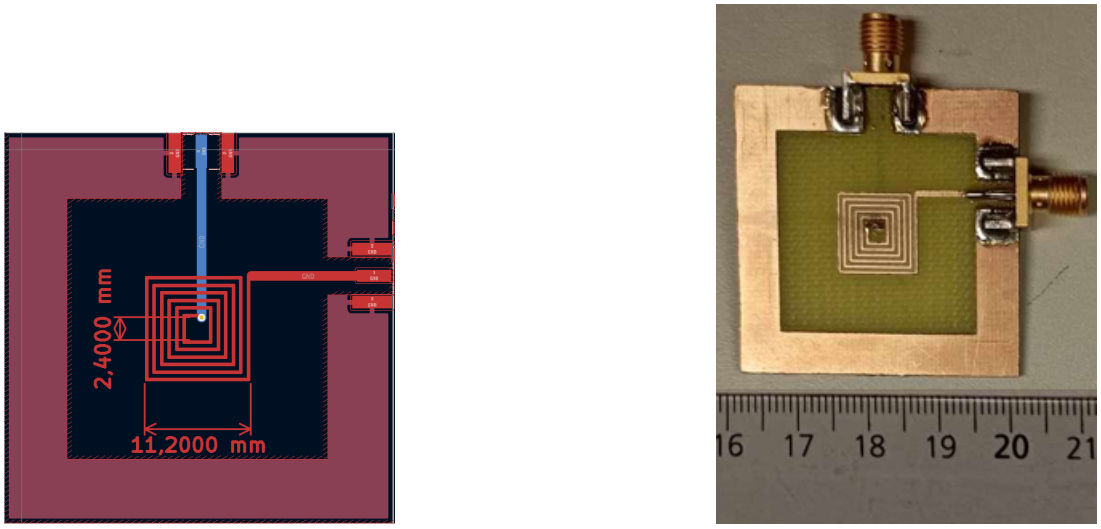


(a) Inductance design via KiCad

(b) Picture of the print

Figure 3.17 – Illustration of sensitive inductance [119]

#### Electrical parameters

Thanks to the equations presented in the theoretical part (Eq. (3.4), (3.7) and (3.11)), we can calculate geometric parameters, the electrical parameters (Table 3.2).

| $R_s$ [Ω] | $L_s$ [µH] | $C_p$ [pF] |
|---|---|---|
| 0.3 | 0.26 | 0.77 |

Table 3.2 – Electrical parameters derived from geometric dimensions

By analyzing the VNA over the entire available spectrum of the device (i.e. from 5 Hz to 3 GHZ) after calibration, we can compare our estimates with reality. Figure 3.18 shows the impedance $Z_{th}$ extracted from parameter S. From our first analysis of the real measurement, in green, we can see all the non-idealities and imperfections present, particularly around 1 kHz and in the irregular phase shift in the inductive part. These are due, among other things, to imperfections in the track (Fig. 3.17b) and in the vertical interconnect access (VIA) connecting the output at the center of the coil to the output of the PCB.

We also identify our purely inductive operating range when $R \leq 2\pi fL$. In our case, based on estimates from geometric parameters, inductance exceeds resistance at around $f_L = \frac{R_s}{2\pi L_s} = \frac{0.3}{2.6 \cdot 10^{-7}} = 189.37$ kHz, with $f_L$ giving the frequency of transition from the resistive to the inductive domain. Based on the measurements, our usable inductive range (i.e. the part evolving linearly with frequency such that $|Z| = \omega L$) lies between 1 MHz and ±200 MHz. Beyond that, we reach the resonant frequency of 324.73 MHz. Above this frequency, the behavior becomes capacitive and random, and can no longer be correctly modeled by our simplifications.

The dotted blue line represents our model (Eq. (3.3)) using the previously estimated parameters. As can be seen, it allows us to recover the general shape of our curve, but a serious difference between the estimated and measured resistance can be observed on graphs 1 and 3 of Fig. 3.18. This error is due to the resistance of the cables between the inductor and the VNA, as well as the resistance provided by the connectors and the VIA. The total resistance of the cables, connectors and system measured with a multimeter gives a value of ± 1.5 Ω.

In graphs 3 and 4, the blue dotted line represents the resistance or inductance estimated with (3.4) and (3.7). The red line represents the average of points whose variation between two consecutive points is smaller than the set threshold (here, 0.01 for resistance and $3 \cdot 10^{-9}$ for inductance), each point meeting this condition is highlighted by a blue dot on these graphs. This method makes it possible to recover resistance $R = \Re[Z]$ or inductance $L = \frac{\Im[Z]}{\omega}$ in a graph where the constant value is present only on a portion of the graph (full code available in appendix A.1).

By comparing the estimated and extracted values of impedance $Z_{th}$ measured with the VNA and listed in table 3.3 and the general appearance of the graphs, we conclude that the estimates derived from the geometric parameters are reliable. The notable difference comes from the resistance measurement, which is greater than the expected estimate, due in particular to the resistance of the cables, via and connectors, the latter contributing non-idealities to our DUT.

| | $R_s$ [Ω] | $L_s$ [µH] | $C_p$ [pF] |
|---|---|---|---|
| Estimated values | 0.3 | 0.26 | 0.77 |
| Extracted values | 1.73 | 0.24 | 1.01 |

Table 3.3 – Dimensions of the first printed sensitive inductor. The first line are the values estimated via the models defined in section 3.1.1 and the second lines are the values extracted from the Z parameter measured via the VNA.

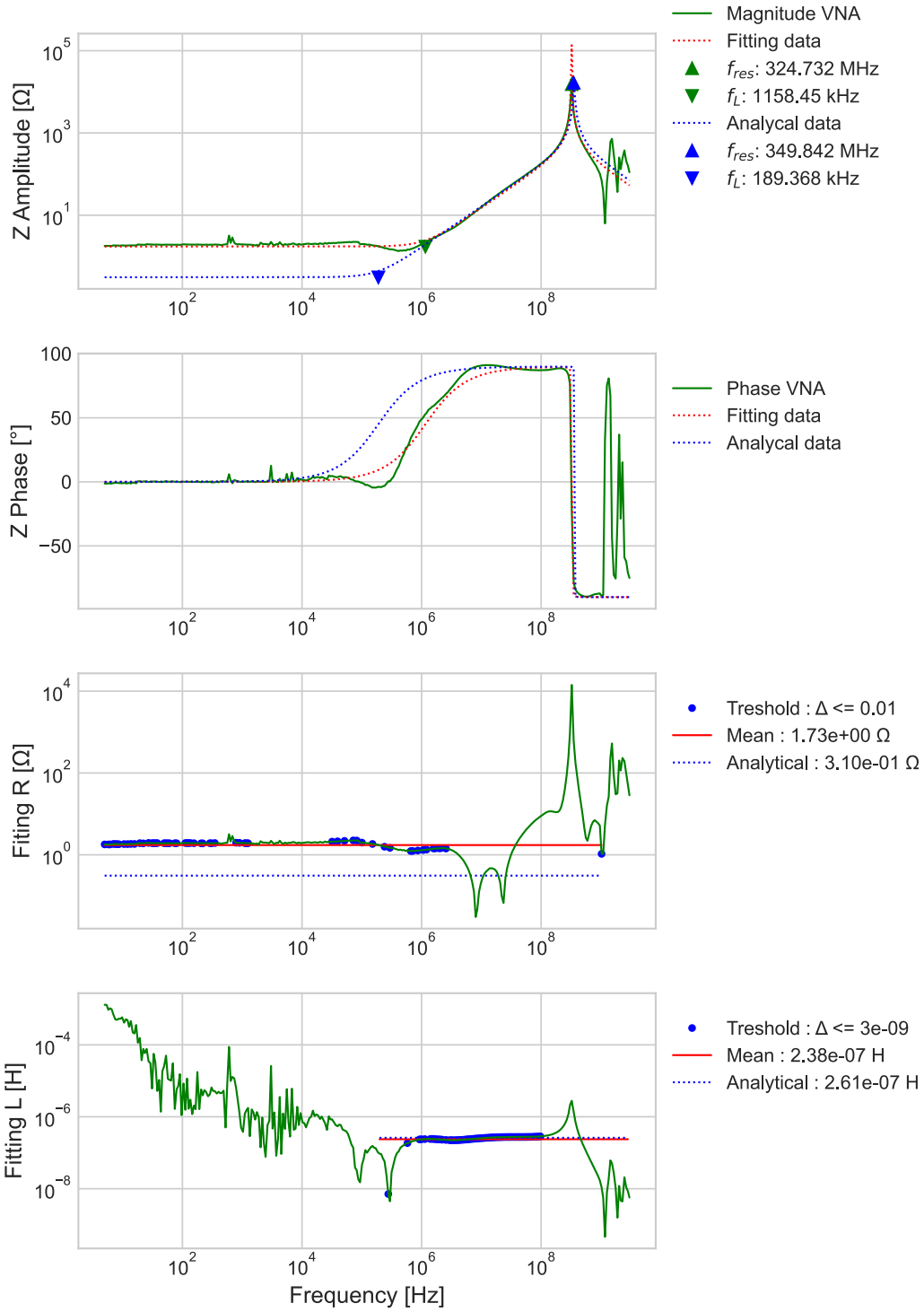


Figure 3.18 – 2 port measurement of VNA sensitive inductance. The first graph shows the amplitude of the VNA measurement $Z = Z_{11} + Z_{22} - 2Z_{12}$ in green, accompanied by the red dotted fit of the resistance (graph 3) and inductance (graph 4) values extracted from the VNA measurements. The dotted blue line represents the theoretical impedance derived from the geometric parameters. The second graph represents the phase, with the same comparisons as for the amplitude.

For the Q factor, we use (3.16) to compare 3 values: the real Q factor, the ideal Q factor via the real impedance, and the theoretical Q factor derived from the geometric parameters (Fig. 3.19).

The solid blue line represents the impedance value derived from the S parameter measurements, the solid green line represents the Q parameter calculated from the VNA measurements, and the dotted red lines represent the Q factor calculated from the theoretical impedance model (Eq. (3.3)) with the values R, L, and C values taken from the VNA measurements, and the blue dotted line represents the theoretical value based on the R,L and C values previously estimated from the **geometric** (Table 3.2) parameters.

The first surprising piece of information that jumps out is the error around 10 to 50 MHZ, where the measured Q factor drops sharply. This error stems from the resistance having the same blunder, with outliers coming from either poor VNA calibration (which seems unlikely, as the rest of the data is consistent), or poor contact within the cables or connectors. A new measurement would be interesting to confirm whether the error is repeatable or due to an irregular measurement, but as the rest of the data is consistent, we can simply consider this part as an outlier and ignore it for our observations.

Apart from that, the frequencies match: the frequencies where the Q-factor is at its maximum coincide, as does the fact that the Q-factor drops sharply at the resonant frequency, illustrated by the impedance spike on the blue curve. As for the divergent maximum Q-factor values, this again stems from resistance-induced errors and non-idealities between the theoretical model and actual measurements.

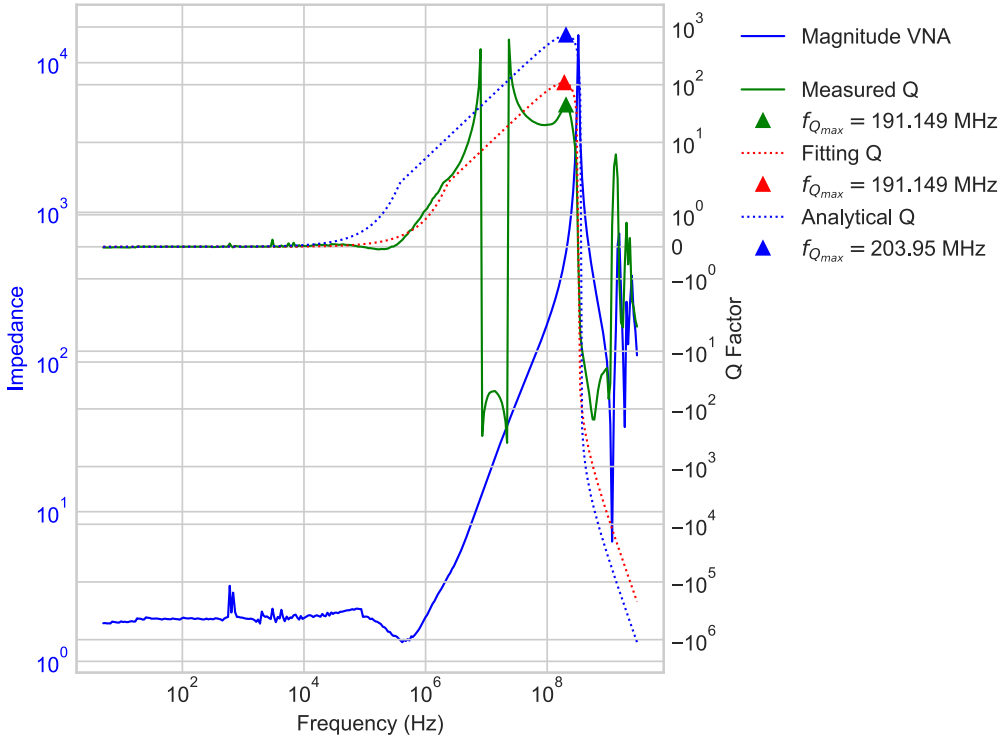


Figure 3.19 – Quality factor Q. In blue, the impedance measurement; in green, the Q factor extracted from the VNA measurement; in dotted red, the Q factor from the theoretical model based on the previously measured R and L values; and in dotted blue, the Q factor estimated via the geometric parameters.

From this first sensitive inductance, we derive specific frequencies such as the resistive-to-inductive transition frequency ($f_L$), the maximum quality factor frequency ($f_{Q_{max}}$) and the resonant frequency ($f_{res}$). The table 3.4 compares analytically predicted and measured frequencies.

| | $f_L$ [kHz] | $f_{Q_{max}}$ [MHz] | $f_{res}$ [MHz] |
|---|---|---|---|
| Estimated values | 189.368 | 203.95 | 324.732 |
| Extracted values | 1158.45 | 191.15 | 349.842 |

Table 3.4 – Comparison of sensitive indutance singular frequencies. The first line are the values estimated via the models defined in section 3.1.1 and the second lines are the values extracted from the Z parameter measured via the VNA.

Apart from a large discrepancy in the $f_L$ frequency due to the difference in resistance between the estimated and actual frequencies, the variation of which is due to the cables, the VIA and the connectors, the other frequencies are correctly estimated. We can therefore rely on the models presented above to predict the inductive behavior of our printed material.

## 3.4 Magnetic variation

### 3.4.1 Theory

In addition to detecting the magnetic field induced by the nanoparticle sample, the sensitive coil will also detect the excitation magnetic field. To better control the behavior of planar inductors, we need to anticipate the behavior of the induced voltage.

Figure 3.21 shows the simplified block diagram representing the transfer function between the excitation voltage $V_{in}$ and the induced voltage $V_{out}$. Figure 3.20 details the equivalent circuit of an excitation/sensitive coil system.

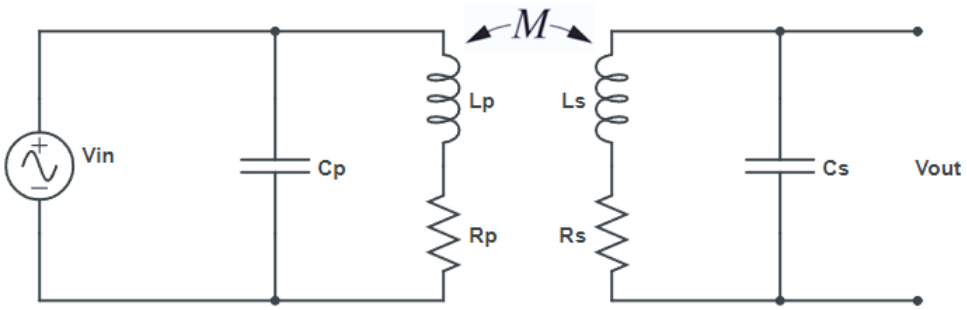


Figure 3.20 – Equivalent diagram of the excitation coil and sensitive coil system

1. First, we have the impedance behavior of the primary circuit (the excitation coil) shown in Fig. 3.22a. Impedance will increase linearly with frequency once it has exceeded the value of the resistance at frequency $f_L = \frac{Rp}{2\pi Lp}$.

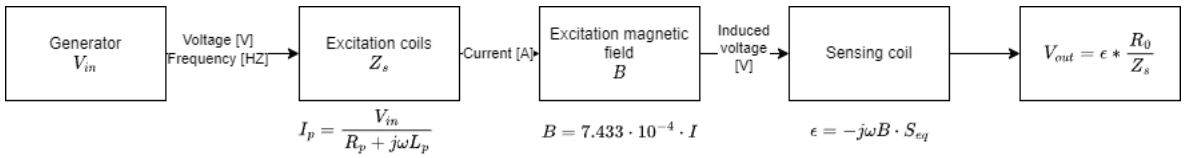


Figure 3.21 – Block diagram of the various physical quantities, including B, the magnetic field produced by the Helmholtz coils (Eq. (3.18))

2. The current, shown in Fig. 3.22b, will decrease as a function of impedance and constant generator voltage $V_{in}$. The magnetic field, inducing a voltage at the sensitive coil, is directly proportional to the generator current, and will therefore decrease in the same way, while undergoing the identical 90° phase shift typical of inductances.
3. The induced voltage $\epsilon$ depends directly on the external magnetic field (Fig. 3.22c), and can also be seen as the mutual contribution such that $\epsilon = -j\omega B \cdot S_{eq} = -j\omega M \cdot I_p$, depends directly on the geometry of the inductor as well as the current in the excitation coil. The induced voltage is initially 90° out of phase below $f_L$ and drops to -180° when the current in the excitation coil is completely 90° out of phase.
4. The final voltage $V_{out}$ (Fig. 3.22d), taking into account the internal resistance $R_0$ of the voltmeter, adds a new limiting frequency $f_H$ depending on the parameters of the sensitive coil, such that $f_H = \frac{R_s}{2\pi L_s}$. Interestingly, since the phase shift is linear, if $f_L$ defines the frequency at which the phase shift is -90° and $f_H$, the phase shift at 90°, then the jump between -180° and 180° lies in the middle of the frequencies $f_L$ and $f_H$ and can therefore be used as a benchmark for future measurements.

The various diagrams shown are only a simplified illustration of the electromagnetic behavior of our system. One important point to note is that the voltage induced in the coils becomes constant above the frequency $f_L$, as the decreasing current counteracts the increasing induced voltage. The expression for induced voltage as a function of frequency and generator voltage is given by :

$$\epsilon = -j\omega B \cdot S \tag{3.32}$$
$$= -j\omega M I_p \tag{3.33}$$
$$= -j\omega M \frac{V_{in}}{Z_p} \text{ V} \tag{3.34}$$

If we take into account the voltmeter load $R_0$ :

$$V_{out} = \epsilon \cdot \frac{R_0}{Z_s} \tag{3.35}$$
$$= -j\omega M \frac{V_{in}}{Z_p} \cdot \frac{R_0}{Z_s} \text{ V} \tag{3.36}$$

### 3.4.2 Results

First of all, we need to check the magnetic behavior of the Helmholtz coils. To do this, we use the Hall probe presented in section 3.2.2. This probe has certain limitations, notably a sensitivity of up to ± 2 µT, and a sampling frequency of 2300 Hz. In addition, thanks to the VNA and datasheet, we know that Helmholtz coils have a resistance of 2.4 Ω, an inductance of 19.45 mH and a resonant frequency of 100 kHz. By applying the various parameters and formulas described above, we can predict the behavior of the magnetic field and induced voltage

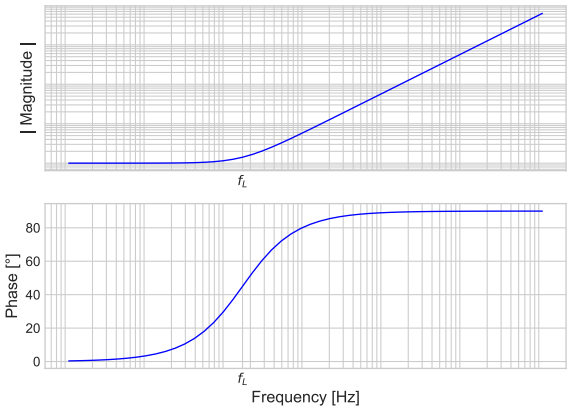


(a) Primary impedance variation

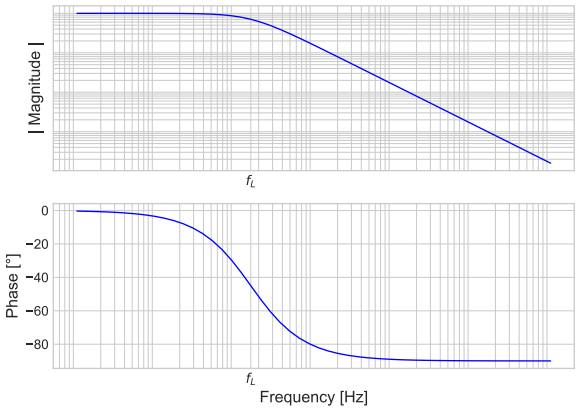


(b) Current variation in the excitation coil

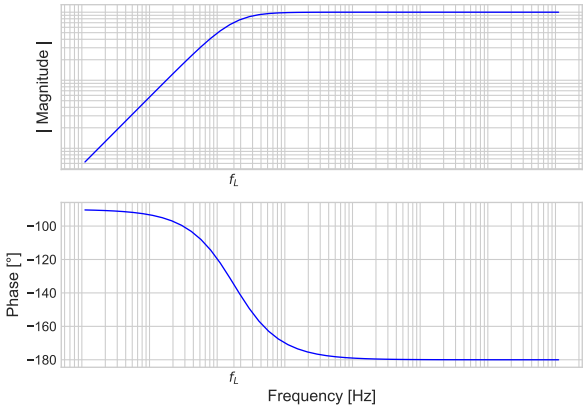


(c) Variation of the voltage induced in the sensitive coil

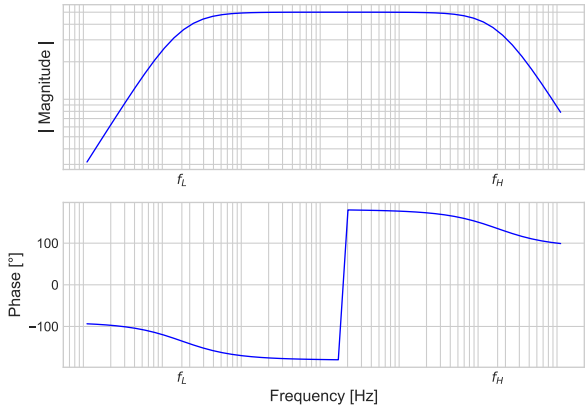


(d) Variation of output voltage

Figure 3.22 – Logarithmic representation of the behavior of the excitation/sensitive coil system. The frequency $f_L$ corresponds to the frequency when $R_p \leq \omega L_p$ and $f_H$ correspond to $R_s \leq \omega L_s$.

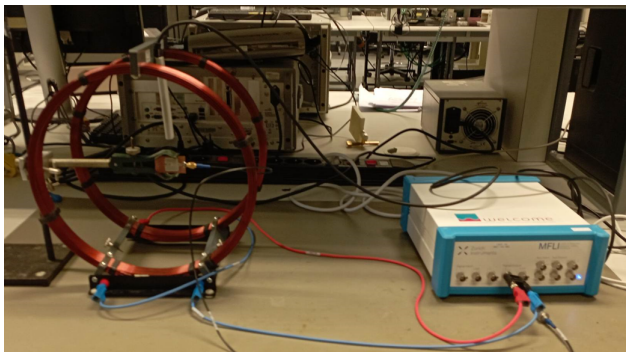

Figure 3.23 – Picture of induced field measurement setup

within a square inductance immersed in the magnetic field (Fig. 3.23).

The MFLI presented in section 3.2.3 will scan the maximum frequency range at maximum voltage, i.e. from 1 kHz to 5 MHz at 3 V. For the clearest possible reading, we need maximum current in the coils to generate a large magnetic field. In addition, we've added a 100 Ω series resistor to get a frequency $f_L$ closer to the spectrum under study.

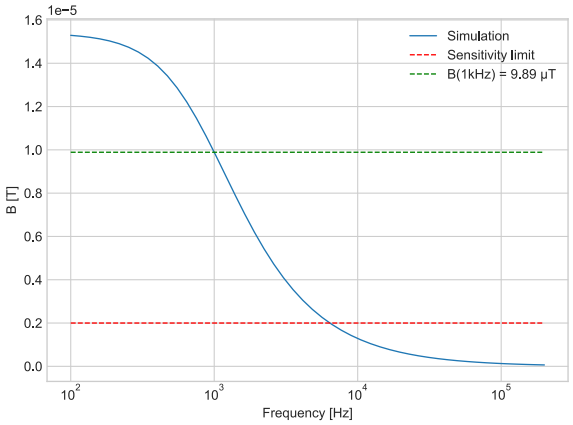


(a) Magnetic field simulation

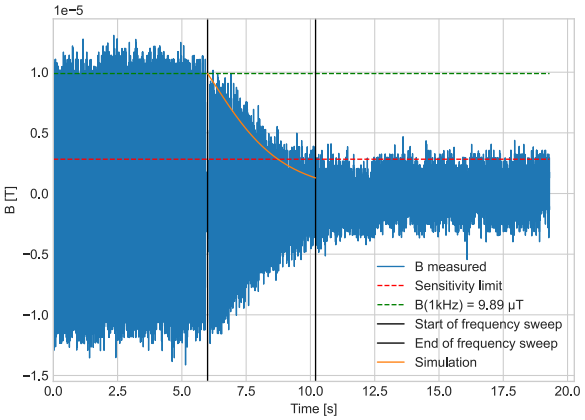


(b) Time measurement of the magnetic field generated by the MFLI. Frequency sweep from 1 kHz to 5 MHz starts at 6.9 seconds. Before the scan, the highly noisy magnetic field is at 1 kHz frequency.

Figure 3.24 – Magnetic field generated by Helmholtz coils

Figure 3.24a shows the theoretical value of the magnetic field generated. Figure 3.24b shows the magnetic field measured by the probe. As we can see, apart from some noise and a sensitivity limited to ± 2 µT, the estimates hold up well. Unfortunately, hardware limitations prevent us from obtaining a cleaner signal and better measurements of the magnetic field produced. As the probe measurement is in the time domain, markers have been placed to delimit the frequency sweep. The sweep time indicated by the MFLI is 3.2 seconds, and since we know when the sweep began, we can delimit the frequency sweep temporally. It starts at 1 kHz around 6.9 seconds, marked by the first black line, and stops at 5 MHz around 10.1 seconds, marked by the second black line.

Figure 3.25 compares the voltage measured via the MFLI with the estimated voltage. As we can see, below the 100 kHz resonant frequency of the Helmholtz coils, our estimates are fairly reliable. But as we get closer to this frequency, the predicted behavior diverges from our measurement. One of the hypotheses would come from certain simplifications made during the development of the calculations presented above, as well as non-idealities around the resonant frequency.

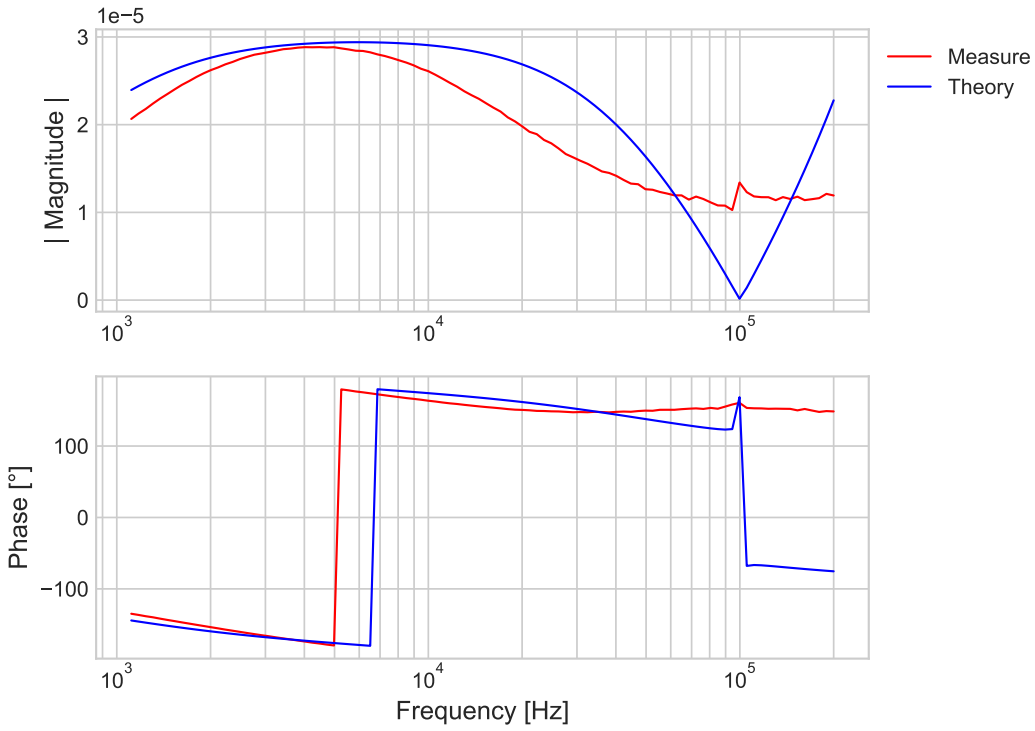


Figure 3.25 – Simulation using 3.36 and measurement of the voltage induced in the internal coil using the MFLI.

# Chapter 4

# Electromagnetic behavior of a pair of inductors

Now that we have seen that it is possible to detect a magnetic field based on a simple planar inductor, we are going to expand our system to include a second inductor whose role will be to excite the magnetic nanoparticles. Indeed, as explained above, these nanoparticles have superparamagnetic behavior (Section 1.2.3), i.e., as a reminder, despite their magnetic susceptibility classifying them as ferromagnetic, their size means that they demagnetize as soon as an exciting external magnetic field is removed. This is why they need to be magnetized with a first exciting coil, and then, to facilitate detection, the magnetizing field produced by them needs to be received with a second sensitive coil.

This chapter introduces the dual exciting/sensing inductor system. Initially, as in the previous chapter, we present the printed inductors and the samples that will be used to highlight the magnetization producing a variation in inductance. We will then analyze the results of the frequency response of the induced voltage as a function of the presence of these samples.

## 4.1 Material

### 4.1.1 Pair of printed inductors

We are going to take the inductance presented in the previous chapter and add an external coil, known as the primary coil, independent of the internal coil, known as the secondary coil. Like Helmholtz coils, the external coil will act as a magnetic field generator. The generated field will magnetize the ferromagnetic sample, which will vary the inductance and therefore the voltage induced in the internal coil, also known as the sensitive coil.

#### External inductance parameters

Figure 4.1 shows the system printed under the same conditions as in the previous chapter. Tables 4.1 and 4.2 detail the physical and electrical parameters of the external coil, respectively, compared with theoretical estimates. As with the internal coil, a shift in resistance due to the cables is noticeable. A multimeter measurement of the circuit including the cables confirms this theory by giving us a value of 1.12 Ω. Our estimates are therefore correct. All this is shown graphically once again in Fig. 4.2.

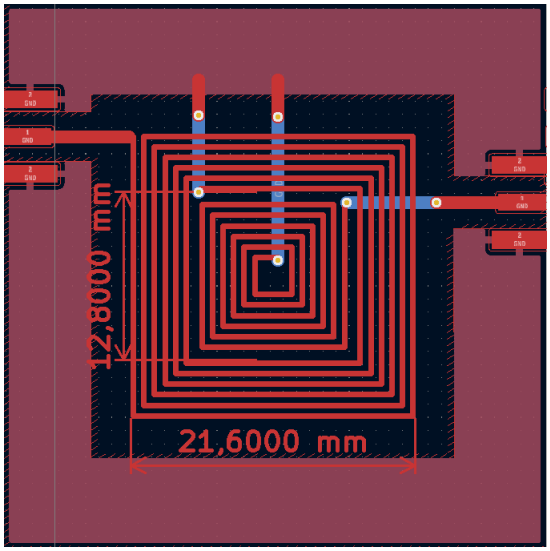


(a) Designing the pair of inductors using KiCad

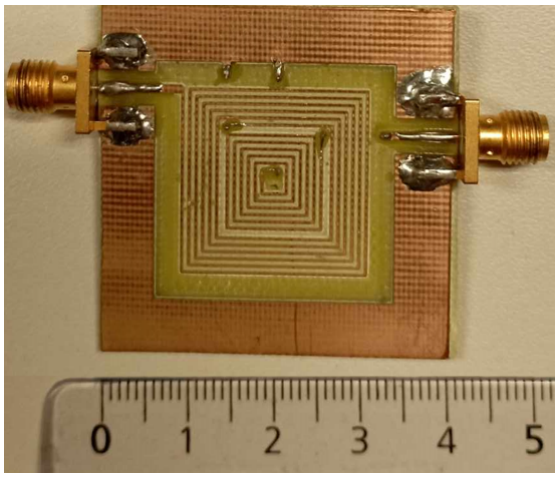


(b) Picture of the print

Figure 4.1 – Introducing the exciting/sensing inductor pair

| $d_{out}$ [mm] | $d_{in}$ [mm] | N | $s$ [mm] | $w$ [mm] | $t$ [µm] | $\rho$ [$\Omega m$] |
|---|---|---|---|---|---|---|
| 21.6 | 12.8 | 6 | 0.4 | 0.4 | 18 | $17{\cdot}10^{-9}$ |

Table 4.1 – External inductor dimensions

| | $R_p$ [Ω] | $L_p$ [µH] | $C_p$ [pF] |
|---|---|---|---|
| Estimated values | 0.958 | 1.10 | 2.37 heightMeasured values |
| 2.07 | 0.837 | 1.62 | |

Table 4.2 – Electrical parameters of the external inductance. The first line are the values estimated via the models defined in Section 3.1.1 and the second lines are the values extracted from the Z parameter measured via the VNA.

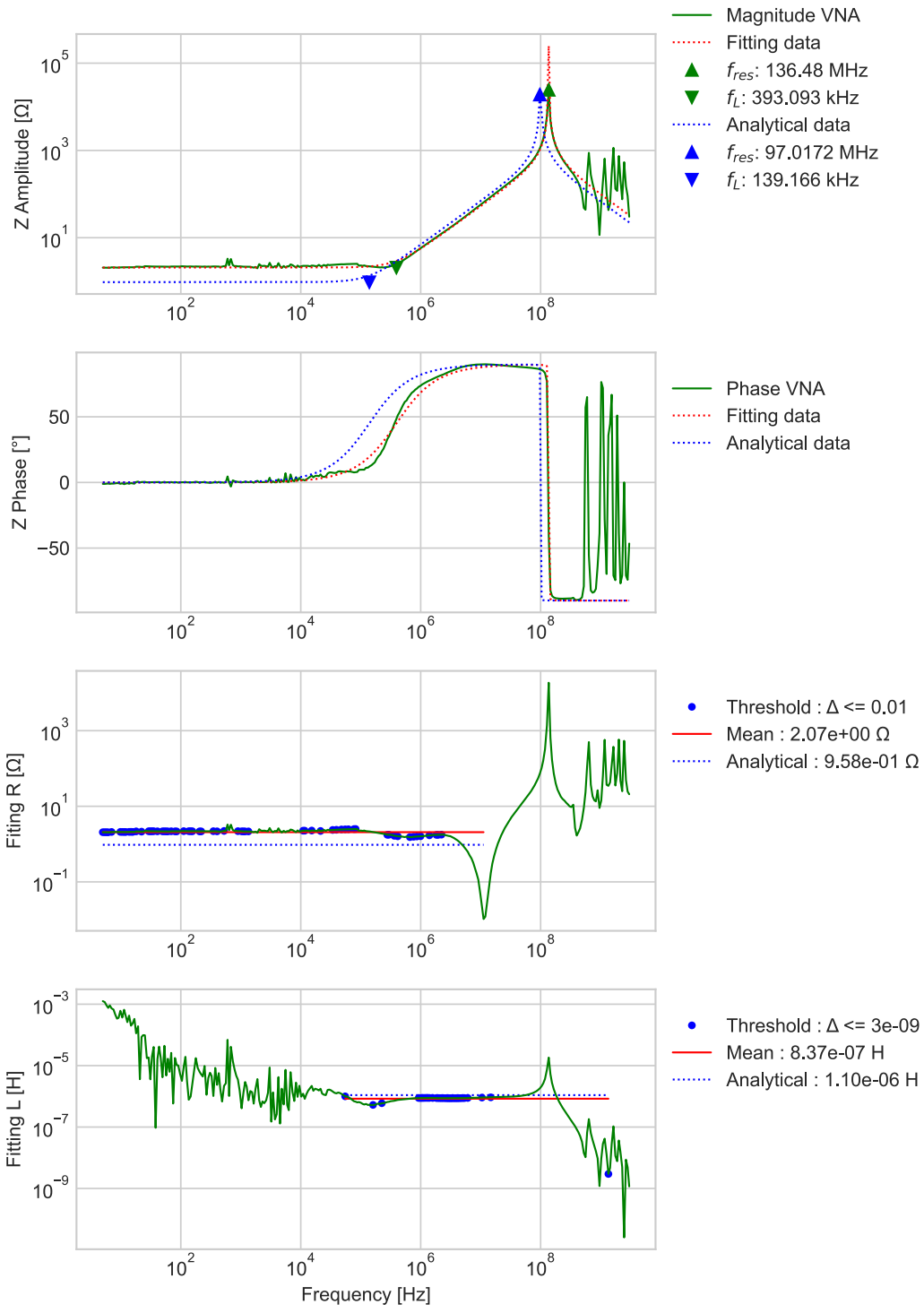


Figure 4.2 – Two port measurement of exciting inductance at VNA. Display of amplitude, phase, comparison with estimated values and measurement of resistance and inductance.The threshold gives the minimum difference required between two consecutive points to be considered « constant » and part of the « average » measurement for resistance and inductance.

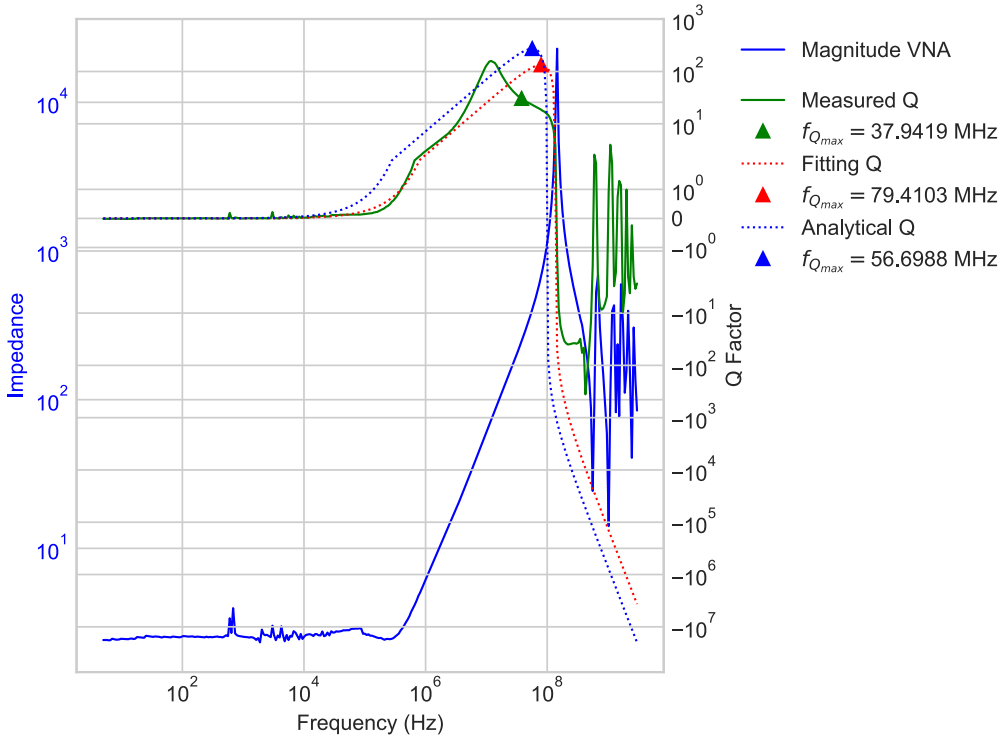


Figure 4.3 – Quality factor Q of the exciting coil

Table 4.3 shows the estimated and measured specific frequencies. Same analysis as for the internal coil, the differences between estimates and reality stem from cable resistance, as well as from vias and connectors. Once again, we note a singularity in the Q factor measured around 10 MHz (Fig. 4.3), due to the singularity in the resistance.

| | $f_L$ [kHz] | $f_{Q_{max}}$ [MHz] | $f_{res}$ [MHz] |
|---|---|---|---|
| Estimated values | 139.166 | 37.94 | 97.0172 |
| Measured values | 393.093 | 79.31 | 136.48 |

Table 4.3 – Comparison of exciting inductance specific frequencies. The first line are the values estimated via the models defined in section 3.1.1 and the second lines are the values extracted from the Z parameter measured via the VNA.

### 4.1.2 Mutual inductance parameter

To determine the mutual inductance between the external coil and the inner coil, 3 methods are used:

1. The classical method presented in Section 1.3.3 : we print a new inductance based on our pair, but the two coils are connected in series (Fig. 4.4) with their loops rotating in the same direction so that the mutual inductances add up.
2. The theoretical method, where we assume that our pair of coils in series amounts to a single large inductance whose number of turns is equal to the number of loops in the first inductor ($N_p$) plus the number of loops in the second inductor ($N_s$). The theoretical inductance is then calculated and the mutual inductance deduced in the same way as for the first method.

3. The direct method, where we consider the two-port measurement of our independent inductances. From this measurement, we take the parameter $Z_{12} = Z_{21}$ which is the mutual inductance [125].

### Classical method

The « classical » method is based on the measurement of a new printout of the two inductances previously presented, this time with a series connection. On Fig. 4.5a, this connection has been highlighted in green. What's more, the internal inductance has been reversed so that the two coils rotate in the same direction for positive mutual inductance, but also for ease of connection.

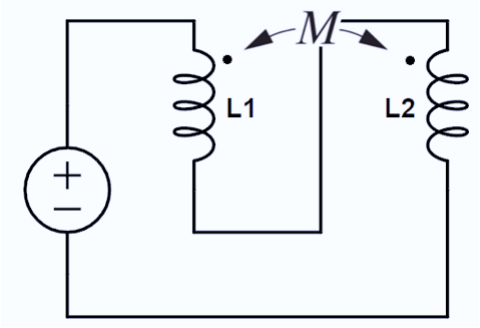


Figure 4.4 – Schematic of section 1.3.3. With $L_1$ and $L_2$, the internal inductance $L_s$ and external inductance $L_p$ whose values have already been estimated/measured.

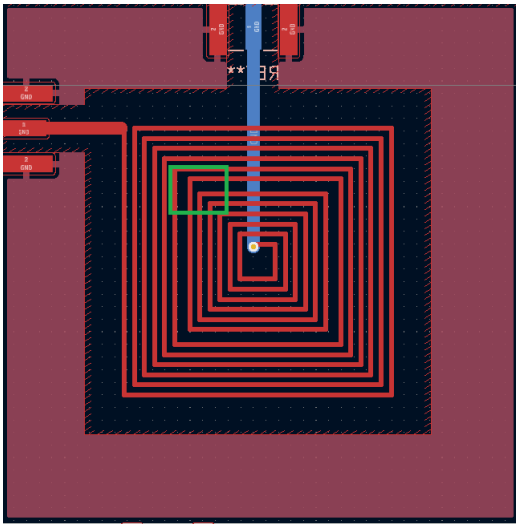

(a) Designing a pair of series-connected inductors highlighted in green.

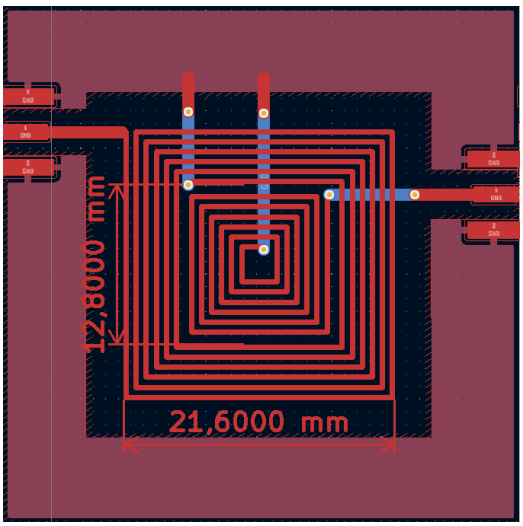


(b) The same pair without the series-connected inductors

Figure 4.5 – Comparison between the series-connected inductor and the inductors without connection. Let us note the reversed wiring direction for the internal inductor.

From these inductors in series, we derive the total induction $L_{tot} = 1.26\mu H$. Knowing the

other two inductances $L_p$ and $L_s$ already measured (Table 4.2 and 3.2), we find :

$$\begin{aligned} M &= \frac{L_{tot} - L_p - L_s}{2} \\ &= \frac{1.26 - 0.944 - 0.238}{2} \ [\mu H] \\ &= 0.0375 \ [\mu H] \end{aligned} \tag{4.1}$$

For a coupling coefficient of :

$$\begin{aligned} k &= \frac{M}{\sqrt{L_p L_s}} \\ k &= 0.21 \end{aligned} \tag{4.2}$$

**Theoretical method**

If we assume that the two series-connected internal and external inductances are equivalent to an inductance with the same inner radius $d_{in}$, but whose number of loops is the sum of the number of internal loops $N_s$ and external loops $N_p$ (Fig. 4.6), we can find the theoretical series inductance and compare it with the printed inductance presented in the previous paragraph. By applying Greenhouse's model (Eq. 3.7) to this inductance, we can find the series inductance, and therefore the mutual inductance.
Table 4.4 shows the geometric parameters of our inductances. The $L_{series}$ series inductance has a smaller outer diameter $d_{out}$ than the primary inductance, because a gap is physically present on our pair to allow our via to pass through, which is not the case for our virtual series inductance.

| | $d_{out}$ [mm] | $d_{in}$ [mm] | N | $s$ [mm] | $w$ [mm] | $t$ [µm] | $L_{Greenhouse}$ [µH] |
|---|---|---|---|---|---|---|---|
| $L_s$ | 11.2 | 2.4 | 6 | 0.4 | 0.4 | 18 | 0.26 |
| $L_p$ | 21.6 | 12.8 | 6 | 0.4 | 0.4 | 18 | 1.06 |
| $L_{series}$ | 20.8 | 12.8 | 6 | 0.4 | 0.4 | 18 | 1.59 |

Table 4.4 – External inductor dimensions

The same logic applies to mutual inductance :

$$\begin{aligned} M &= \frac{1.59 - 1.06 - 0.26}{2} \ [\mu H] \\ &= 0.135 \ [\mu H] \\ k &= 0.25 \end{aligned} \tag{4.3}$$

As with previous Greenhouse estimates, the result is overestimated in relation to reality, notably due to physical differences such as the gap between external and internal inductance. Apart from this slight overestimation, we can nevertheless conclude that this theoretical technique gives a good approximation of the mutual inductance of two concentric and coplanar square planar inductors.

From this technique, we can go even further, in particular by looking at the influence of parameters on mutual inductance. The parameters of inter-branch spacing $s$, wire width $w$ and thickness $t$ are fixed by technical means, so they will not be studied in this document. The internal diameter $d_{in}$ will not be studied here either, but we can assume that all the parameters vary the surface area in some way, and that this variation in surface area can be represented by

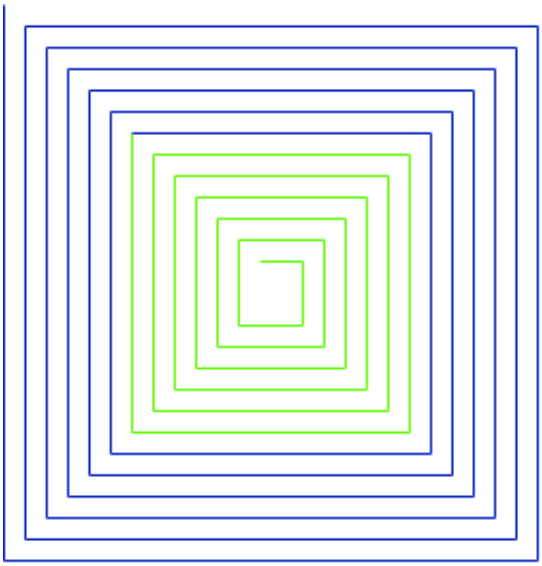

Figure 4.6 – Illustration of the theoretical series inductance. In green, the secondary inductor with $N_s = 6$, in blue, the primary inductor with $N_p = 6$, and both combined, the series inductance with $N_{series} = 12$. Note the absence of gap between internal and external inductance, unlike Fig. 4.5.

the number of loops (Fig. 4.7) : twice as many loops give twice as much surface area.

On the other hand, manipulating the number of loops can be interesting and much more representative of mutual inductance. A first study is made if we keep the ratio $N_p = N_s$. Figure 4.8 shows a constant evolution as we increase the number of loops while keeping the ratio constant. In addition, the factor $k$ has an outlier at its origin, probably due to the limitations of the Greenhouse model.

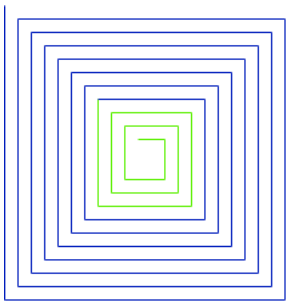

(a) Illustration of $N_p = 7$ and $N_s = 3$

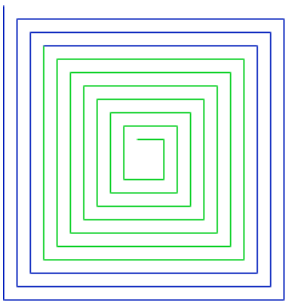

(b) Illustration of $N_p = 3$ and $N_s = 7$

Figure 4.7 – Illustration of series inductance with $N_{total} = 10$. In blue the primary inductance $L_p$, in green the secondary inductance $L_s$ and the two wires make the series indutance $L_{series}$. The inside diameter $d_{in}$, the outside diameter $d_{out}$ and the width and space between two wires $w$ and $s$ all remain constant.

Apart from that, nothing surprising. Internal and external inductances increase with the number of loops, and the mutual inductance follows this trend. The coupling coefficient decreases inversely, since the external inductance will always be greater than the internal inductance.

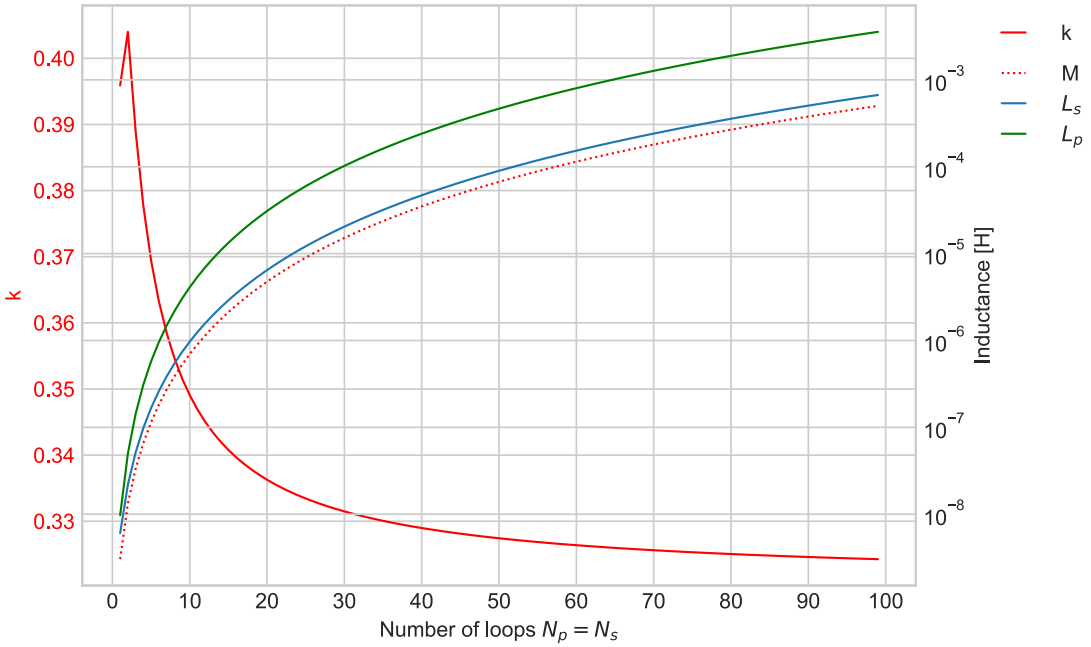


Figure 4.8 – Evolution of primary inductance $L_p$, secondary inductance $L_s$, mutual inductance $M$ and coupling coefficient $k$ as a function of the same number of loops $N_p = N_s$.

What becomes much more interesting is when we vary the ratio $\frac{N_s}{N_p}$. This ratio is illustrated in the form of a graph (Fig. 4.9) where the number of loops of the secondary inductance $N_s$ is increased from 1 to 100 while the number of loops of the primary inductance $N_p$ decreases inversely such that $N_{total} = N_p + N_s = 100$.

.

This study highlights several crucial points. Firstly, it should be noted that the mutual inductance M reaches its maximum value when the ratio $\frac{N_s}{N_p}$ is $\frac{73}{27} = 2.70$. This ratio approaches $\approx 2.42$ as the total number of loops increases. In other words, for a specific surface area, mutual inductance is optimal when there are approximately 2.42 times more loops in the secondary than in the primary. So, for a pair of 10 loop sensing and exciting inductances, taking into account the need for an integer number of loops, it is preferable to have 7 loops in the primary and only 3 in the secondary to maximize mutual inductance.

Secondly, the primary and secondary inductances are equal when the ratio $\frac{N_s}{N_p} = \frac{70}{30} = 2.33$ is reached. We might have thought that mutual inductance would be at its maximum when primary and secondary inductance are equal, but this is surprisingly not the case. We can assume that this difference is due to the constant surface ratio : as the inner diameter of the secondary inductor is equal to the outer diameter of the primary inductor, a constant appears. Unfortunately, no analytical study will be produced in this document to explain this ratio.

A third salient point is the maximum coupling coefficient, with a value of $k = 0.46$ when the ratio $\frac{N_s}{N_p}$ is $\frac{90}{10} = 9$. It may seem surprising that this maximum differs from the ratios quoted above. Although a quadratic trend can be discerned between mutual inductance and coupling coefficient, this observation does not seem robust. This study does not dwell further on an analytical explanation for this peculiarity. It is worth mentioning that values of $k$ greater than 1, physically

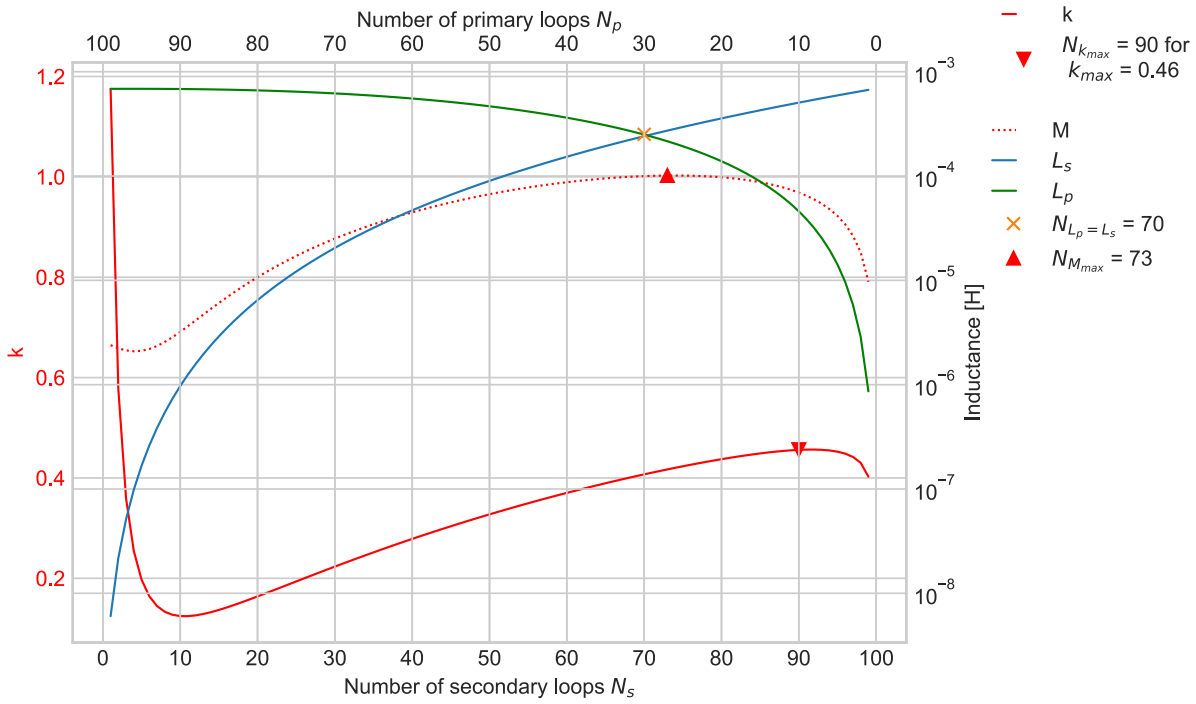


Figure 4.9 – Evolution of primary inductance $L_p$, secondary inductance $L_s$, mutual inductance $M$ and coupling coefficient $k$ as a function of the number of loops $N_s = 100 - N_p$

impossible, are outliers, artifacts of the model. Similarly, we observe that $k$ increases markedly after reaching its minimum at around $N_s = 10$. This portion of the results could also be considered an anomaly, perhaps due to the inapplicability of the Greenhouse model in this context. Nevertheless, it would be relevant to carry out inductors in order to verify whether the coupling coefficient really cannot exceed the maximum value $k = 0.46$, thus corroborating this supposition.

From the few observations we have been able to make, these various particular ratios are constant, regardless of the number of turns (Fig. 4.10a) or the value of the geometric parameters (Fig. 4.10b) as long as the inductors remain square, concentric, coplanar and the external inductor can be considered an extension of the inner inductor. The complete code for studying mutual inductance is available in Appendix A.2.

Knowing that the signal is influenced by the primary inductance at low frequency, and the mutual inductance at high frequency, and that, above all, we'll tend to want to take measurements at high frequency in order to have a sufficiently strong signal, it's the mutual inductance that we'll seek to maximize, aiming for a ratio of $\approx 2.42$ between the number of loops of the sensing inductor and the exciting inductor.

### Direct method

The direct method allows us to directly derive the mutual inductance of the S-parameter measured with the two-port VNA. Indeed, if we measure our pair of inductors with two ports with the VNA (Fig. 4.11a), the measurement $Z_{in} \approx Z_{11}$ takes the impedance measurement of the external coil, while $Z_{out} \approx Z_{22}$ takes the internal measurement, depending of course on how we connect the ports to our pair of inductors. For your information, a comparative table

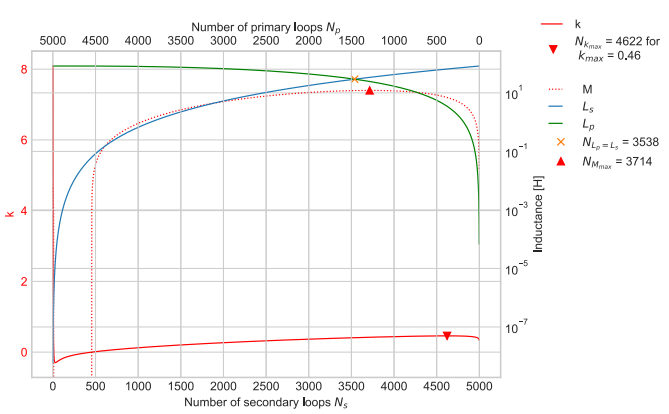


(a) Same parameters as for the 4.9 graph, but with $N_{total} = 5000$ loops.

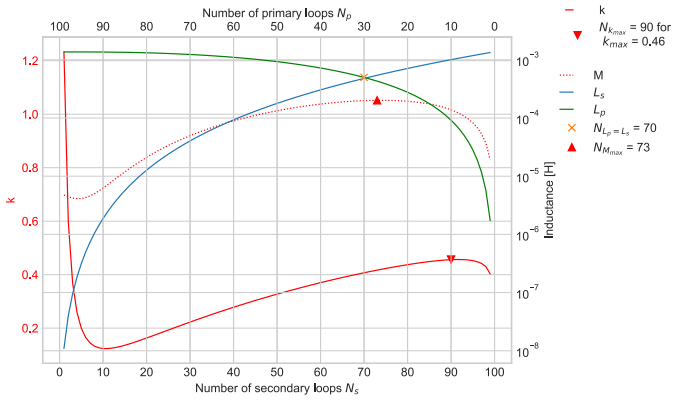


(b) $N_{total} = 100$ but the geometrical parameters have been randomly modified: $d_{in} = 4.4$ mm and $w = s = 0.8$ mm.

Figure 4.10 – Variation of the parameters of the theoretical model of series inductance. The various markers are always in the same places (i.e. we always have the same $\frac{N_s}{N_p}$ ratios on the graph regardless of the parameters).

between the VNA measurements of the pair of coils, and the coils alone is highlighted in Table 4.5.

| | $L_p$ [µH] | $L_s$ [µH] |
|---|---|---|
| Isolated inductor | 0.944 | 0.241 |
| Pair of inductors | 0.842 | 0.264 |

Table 4.5 – Comparison between VNA measurements directly on the exciting/sensing inductor pair and inductor measurements alone

If we take the equivalent circuit in « T », we can show that the measurement $Z_{12} = Z_{21} = M$ (Fig. 4.11b). For $k$, we can use the $Z_{in}$ and $Z_{out}$ values to get a good estimate for our system. We therefore find :

$$\begin{aligned} M &= Z_{12} = Z_{21} = 0.118\ [\mu H] \\ k &= \frac{M}{\sqrt{Z_{in} \cdot Z_{out}}} = 0.25 \end{aligned} \tag{4.4}$$

The mutual inductance found is different from other estimates/measurements made, but remains within the same range of values. This measurement can be considered a good estimate of mutual inductance.

### Comparison and conclusion

Let us compare our 3 methods (Table 4.6). We note that the theoretical and direct methods more or less agree on the mutual inductance, and completely agree on the coupling coefficient. In contrast, the classical method deviates from both.


(a) Classic representation

(b) « T » representation

Figure 4.11 – Two-port measurement of inductance pair

| Method | Classic | Theoretical | Direct |
|---|---|---|---|
| M [µH] | 0.0375 | 0.135 | 0.118 |
| k | 0.21 | 0.25 | 0.25 |

Table 4.6 – Comparison of conventional and direct measurements with theoretical estimates of mutual inductance

At first glance, one might assume that the **classical method** is the most reliable. However, it requires two circuit impressions to evaluate mutual inductance, which multiplies the risk of imperfections and may alter the accuracy of the measurement. A significant discrepancy is also observed between the mutual inductance obtained by this method and that measured by other techniques. However, the coupling coefficient remains within acceptable ranges. This suggests that, despite the discrepancy in mutual inductance, the relationship between the inductances, illustrated by the coupling coefficient, remains stable.

**The theoretical method** based on the Greenhouse model often tends to overestimate inductance values. Although it offers a decent estimate, it is essential to remember that this approach is strictly theoretical. It is therefore advisable to adopt a cautious attitude when using it, especially as it does not consider the concrete discrepancy between internal and external inductance caused by the vias.

**The direct method** directly evaluates the relationship between sensing and exciting inductance. The advantage of this two-port measurement on our pair is that it allows us to obtain the majority of the system's key values without the need for additional printed circuit boards. This method is therefore highly recommended for rapid characterization of such systems.

### 4.1.3 Samples

For our experiments, we will first use two types of ferromagnetic samples of known relative permeability. We will vary the size and thickness of these samples to conduct our various tests. We will then carry out tests with samples of different concentrations of MNP.

#### Ferromagnetic samples

To highlight the variation in inductance in the presence of ferromagnetic samples, we will use two types of iron (Fe) alloy foil. The first type has an amorphous structure characterized by a relative magnetic permeability of $\mu_r = 5000$. The second type has a crystalline structure with a relative permeability of $\mu_r = 80000$, i.e., 16 times greater than the amorphous structure.

Samples will therefore be classified based on three parameters:

1. Their nature: amorphous or crystalline
2. Their surfaces: three were chosen: one covering the entire internal and external inductance of $\pm 5\ cm^2$, one covering only the internal inductance of $\pm 1\ cm^2$ and one fitting into the internal diameter of the internal inductance of $\pm 1\ mm^2$.
3. Their thicknesses: the 1 and 5 cm² surfaces have thicknesses of 1, 5 and 10 layers. The 1 mm² samples are 1, 2 or 3 layers thick. Making more than 3 layers was difficult at this size without specialized tools. Each layer is 17 µm thick, but a more or less irregular air space may have crept in between layers due to the hand-made design.

Each sample is isolated with adhesive tape to avoid any false contact during measurement. Fig. 4.12 shows all the samples created. The left-hand side shows the crystalline samples, the right-hand side the amorphous samples. From the center to the sides, the surfaces are 5 cm², 1 cm² and 1 mm² respectively. From top to bottom, thicknesses range from the thickest layer (10 or 3) to one layer.

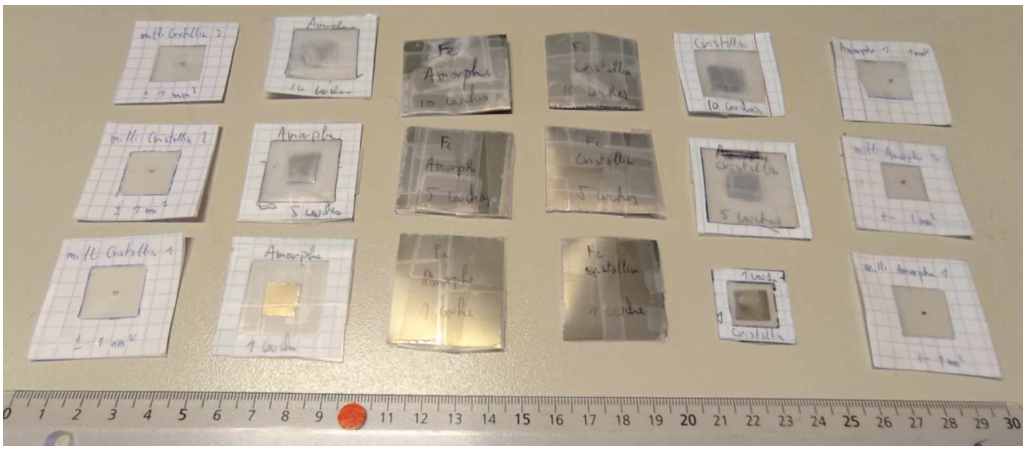

Figure 4.12 – Ferromagnetic samples used in this work

To make the graphs easier to read, sample identification is abbreviated. Following the layout Fig. 4.12, the list of abbreviations is shown Table 4.7.

| | Cristalline | | | Amorphous | | |
|---|---|---|---|---|---|---|
| | 1 mm² | 1 cm² | 5 cm² | 5 cm² | 1 cm² | 1 mm² |
| 1 layer | Cri-1mm-1L | Cri-1cm-1L | Cri-5cm-1L | Am-5cm-1L | Am-1cm-1L | Am-1mm-1L |
| 2 or 5 layers | Cri-1mm-2L | Cri-1cm-5L | Cri-5cm-5L | Am-5cm-5L | Am-1cm-5L | Am-1mm-2L |
| 3 or 10 layesr | Cri-1mm-3L | Cri-1cm-10L | Cri-5cm-10L | Am-5cm-10L | Am-1cm-10L | Am-1mm-3L |

Table 4.7 – Sample identification abbreviation

### Magnetic nanoparticle samples

The magnetic nanoparticles samples are for qualitative study only. For information, ferrite nanoparticles are between 50 and 100 nanometers in size, and rest in an ethanol solution which must be sonic in order to obtain the most homogeneous mixture possible and avoid aggregates which can deteriorate the magnetization.
We created 6 samples shown Fig. 4.13. From left to right, we have the first sample, which is the base concentration, the second contains twice as much concentration as the first, and so on up to the sixth on the right.
Each concentration was spread over an area of $\pm 10\ mm^2$ and 0.14 mm.

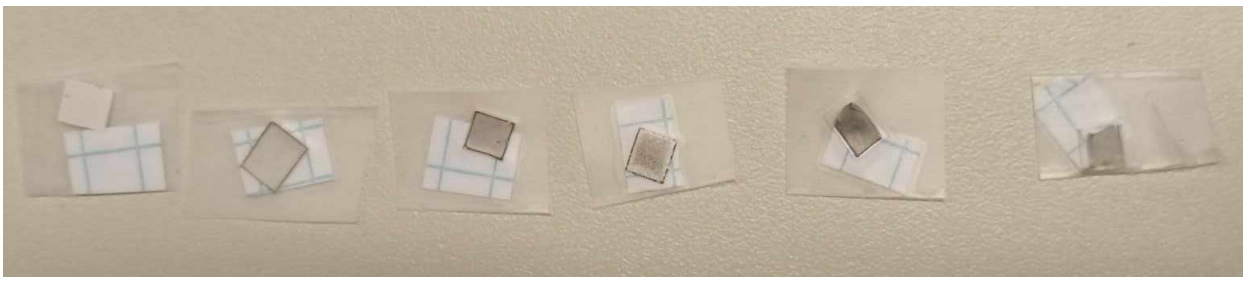

Figure 4.13 – MNP samples. The sample in the foreground, and its labeling on a simple grid in the background. Total thickness with foil and tape ≈ 1 mm.

## 4.2 Study of frequency response

In this section, we get to the heart of the matter: understanding and modeling the frequency response of our pair of inductors. We will start with an **analysis without sample** of the voltage induced across the sensitive coil under electromagnetic excitation from the external coil. We will then highlight the **impedance variation** due to the presence of a ferromagnetic sample, and finally compare the different responses produced by the different samples to study their detection efficiency, as well as the different sample parameters influencing the measured induced voltage.

### 4.2.1 No-sample frequency response

Figure 4.14 shows the measurement of the induced voltage as a function of frequency. As with previous measurements made at the MFLI, the range swept is from 1 kHz to 5 MHz. We have chosen a voltage of 1 V for the exciting coil, as our inductors will eventually be incorporated into a low-energy measuring device, and as the system is on PCB, it is in our interest to use a low voltage.

Unlike the theoretical induced voltage described in the previous chapter (Figs. 3.22c and 3.22d), this time we have a different graph shape. We can see several features: a stable initial voltage before increasing linearly with frequency as predicted theoretically, a phase shift per stage, an initial phase shift up to 90° where the phase shift becomes stable over a range of frequencies, then increases again towards 180°.

In addition, the graph in the form of error bars shows the standard deviation (vertical bars) around the mean value (solid line). Our original signal is small relative to the noise amplitude,i.e. a lower SNR (Section 3.1.2), which explains why we have a higher standard deviation at low frequencies. This is already a good parameter to take into account when choosing the frequency for future biosensor design.

Figure 4.15 shows the theoretical induced voltage based on the observations made Fig. 4.14. Seeing an initial voltage $V_0$, I add this to our model. What is more, the initial 90° phase shift indicates that the inductive nature of the sensing coil first takes over, before continuing its phase shift induced by the inductive nature of the exciting coil.

As can be seen, two key frequencies are again highlighted. The first frequency, $f_L$, marks the transition from the resistive to the inductive domain:

$$f_L = \frac{V_0}{V_{in}} \cdot \frac{R_p}{2\pi M} \tag{4.5}$$

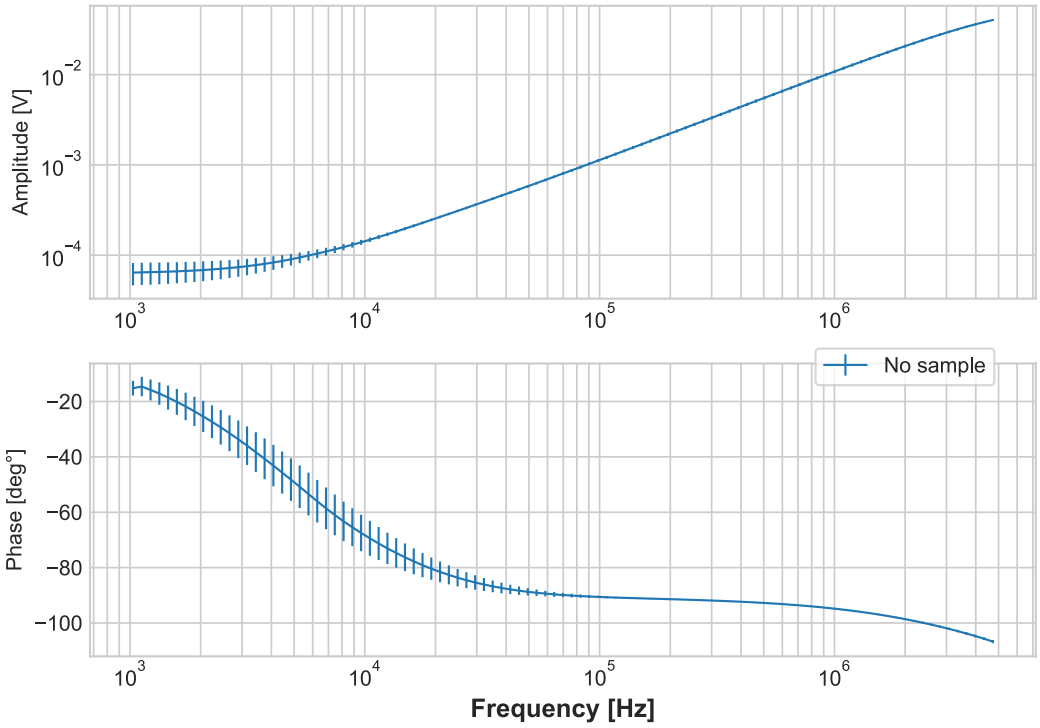


Figure 4.14 – Induced voltage measurement without sample

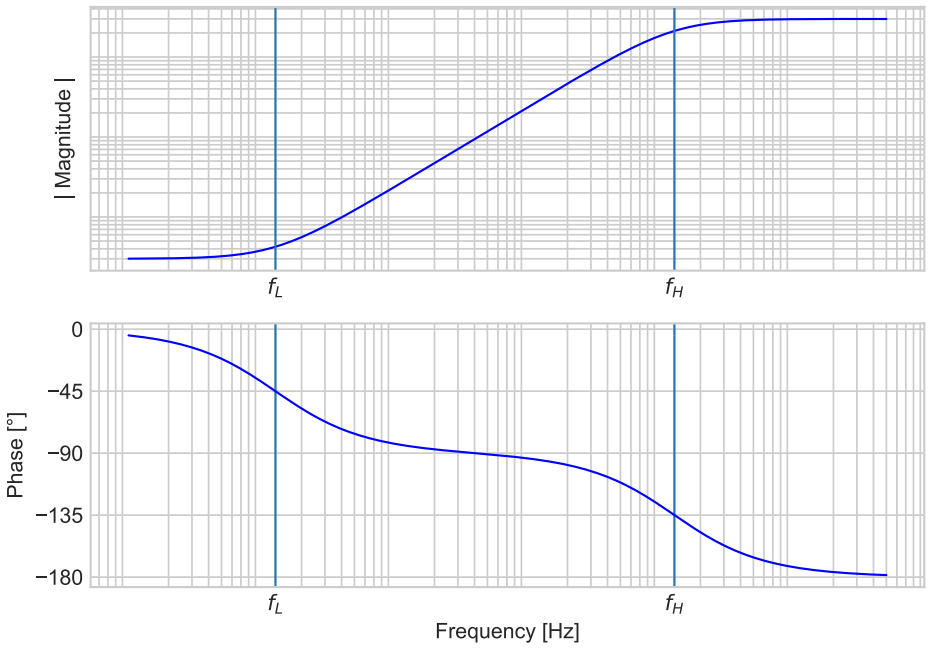


Figure 4.15 – Theoretical voltage of inductor pair

The second frequency gives the passage of the second stage from 90° to 180° as follows:

$$f_H = \frac{R_p}{2\pi L_p} \tag{4.6}$$

All the elements of the previous models highlighted (Eq. (3.34)) give the new model (Eq. (4.7)) :

$$V_{out} = V_0 - j\omega M \cdot \frac{V_{in}}{Z_p(f)} \tag{4.7}$$

If we apply the various data collected (self-inductance, mutual inductance, etc.), while taking into account generator impedance $R_0 = 50\ \Omega$, we obtain the graph depicted Fig. 4.16. The dotted line shows the predicted voltage, the solid line the measured voltage.

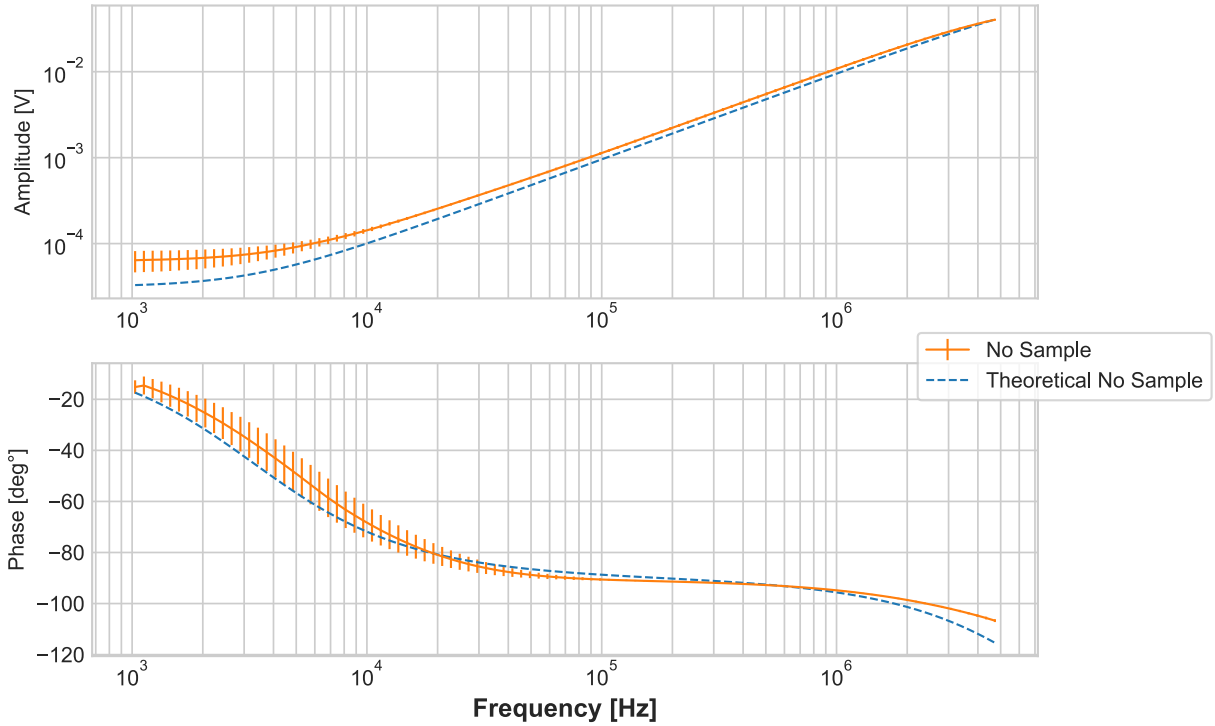


Figure 4.16 – Theoretical voltage of inductor pair

We can see that we are not far from reality, with a few differences. One hypothesis is that the voltage could be induced by an initial current generated by the magnetic field. However, this idea seems implausible, as it would not result in a stable low-frequency voltage. Even if it did, the value would be approximately $R_s \cdot \frac{V_{in}}{Z_p} \approx 23\ mV$, which is considerably higher than what we observe.
Another potential explanation could be a weak short-circuit between the exciting and sensing coils, resulting in a stable voltage of around $65\mu V$. To confirm this theory, it would be relevant to carry out measurements on the detection coil with a fixed voltage from the generator.

The models we have presented are admittedly simplified, and it is likely that certain details or constants have not been taken into account. Nevertheless, our model accurately describes the general trend in induced voltage, and provides a basis for predicting future inductance variations caused by the presence of samples.

### 4.2.2 Theoretical inductance variation

Now that we have a model to work from, we can look at what would happen with the addition of a ferromagnetic sample.

A magnetized ferromagnetic sample will produce its own magnetic field aligned with the exciting magnetic field. Thanks to (1.32), we know that this additional magnetic flux ($\Phi_s$) will induce an additional voltage such that :

$$\epsilon = -j\omega\Phi_0 - j\omega\Phi_s \tag{4.8}$$

This contribution to the general magnetic flux can be considered as a variation such that :

$$\epsilon = -j\omega\ (L_0 + \Delta L_{sample})i \tag{4.9}$$

The magnetic variation generated by the material is influenced by its magnetic permeability, its geometry, and any other factor that may modify the perception of the magnetic field it produces by the inductors. With a higher relative permeability $\mu_r$, the variation in inductance $\Delta L_{sample}$ should be greater. Note that relative permeability is not the magnetic permeability perceived by the inductance. Relative permeability describes the magnetic behavior within the material, but not the magnetic behavior around the material. In this case, we speak of apparent magnetic permeability [126].

For example, the distance between the sample and the inductor is an important factor to take into account. The impact of the distance between a ferromagnetic sample and a square inductor is indeed highlighted in [127] . In Fig. 4.17, we can see that 2 mm of distance can bring almost 20 % variation on the total inductance value.

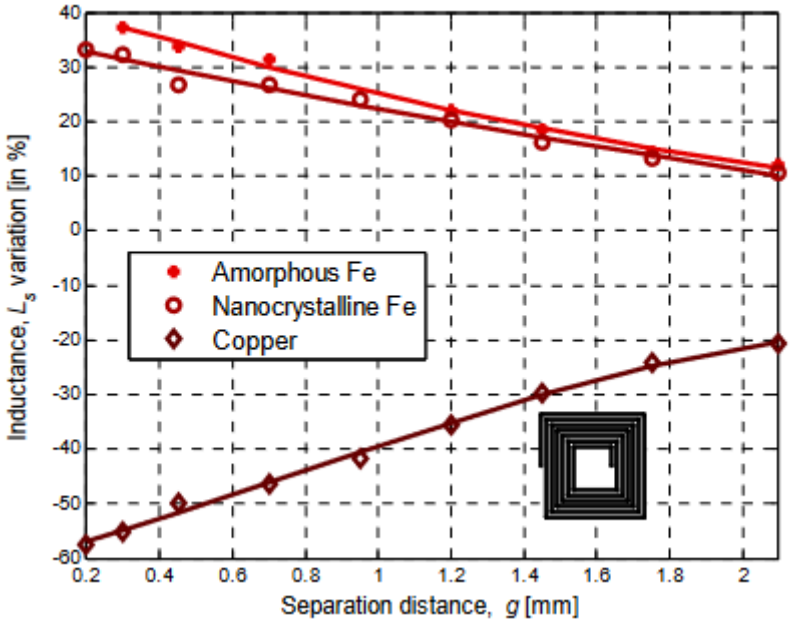


Figure 4.17 – Variation of measured inductance as a function of the deviation between a sample and a square inductance [127].

For this reason, measurements are carried out with a clamp holding the sample against the inductance, previously insulated with adhesive paper.

Other parameters such as surface area, thickness and magnetic permeability will be considered in later sections.

But what impact does this variation have on our induced voltage? As the sample will influence our two inductors, their inductance values and their mutual inductance will vary. Since our model depends only on $M$ and $L_p$, we can consider three cases:

1. $\Delta L_p = \Delta M$
2. $\Delta L_p < \Delta M$
3. $\Delta L_p > \Delta M$

With $\Delta L_p$, the sample variation impacting the primary inductance and $\Delta M$, the variation impacting the mutual inductance such that the variation is defined as the ratio between the inductance without the influence of the sample's magnetic field and the inductance with the sample's influence.

In Fig. 4.18, we find an identical variation, i.e. we vary $L_p$ and $M$ by the same ratio. This case can be encountered if the sample covers both inductances. We can see that a positive variation, i.e. when $L_s < L_s + \Delta L_s$ (conversely $M < M + \Delta M$), induces an earlier transition into the inductive domain, whereas a negative variation will delay this transition. Note that the high-frequency voltage remains unchanged.

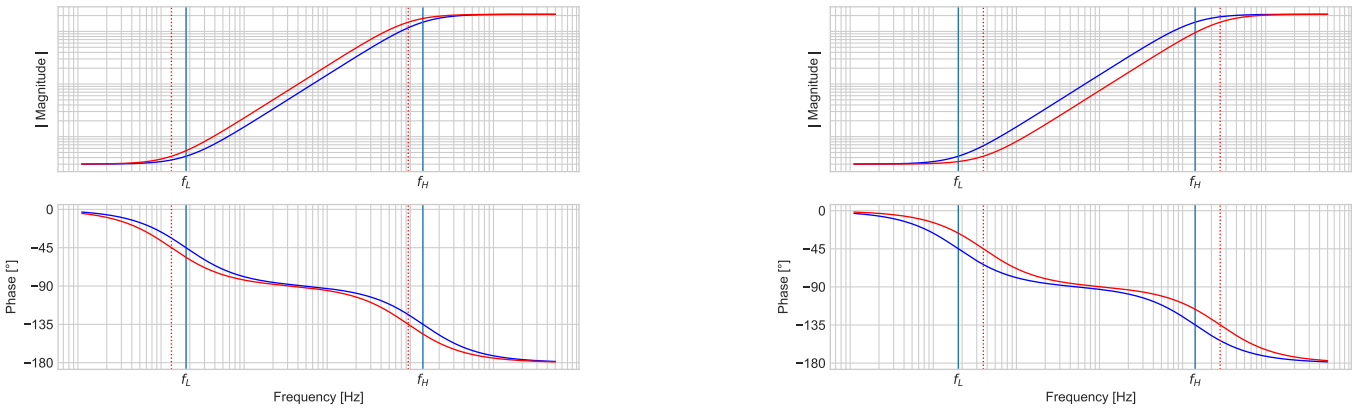


(a) Positive variation

(b) Negative variation

Figure 4.18 – **Identical** variations in inductance values $L_p$ and $M$. In blue, the signal without sample, and in red, the signal with sample.

The first Fig. 4.19a shows the case where the variation is stronger on the mutual inductance than on the primary inductance, for example when the sample covers only the central inductance. This variation induces an earlier transition into the inductive domain, but delays it towards 180°. In addition, the high-frequency voltage is greater than expected.

The second Fig. 4.19b shows the opposite case: the inductive domain is reached later and the $f_H$ frequency is reached earlier. In addition, the voltage at high frequency is lower.

In conclusion, the impact of the measured sample on primary and mutual inductances need to be monitored . If both are affected in the same way, measure at a frequency within the inductive range, i.e. between $f_L$ and $f_H$. If only one of the inductances is affected, it is best to measure the voltage at high frequencies, i.e. above $f_H$. Voltage can also be measured in the

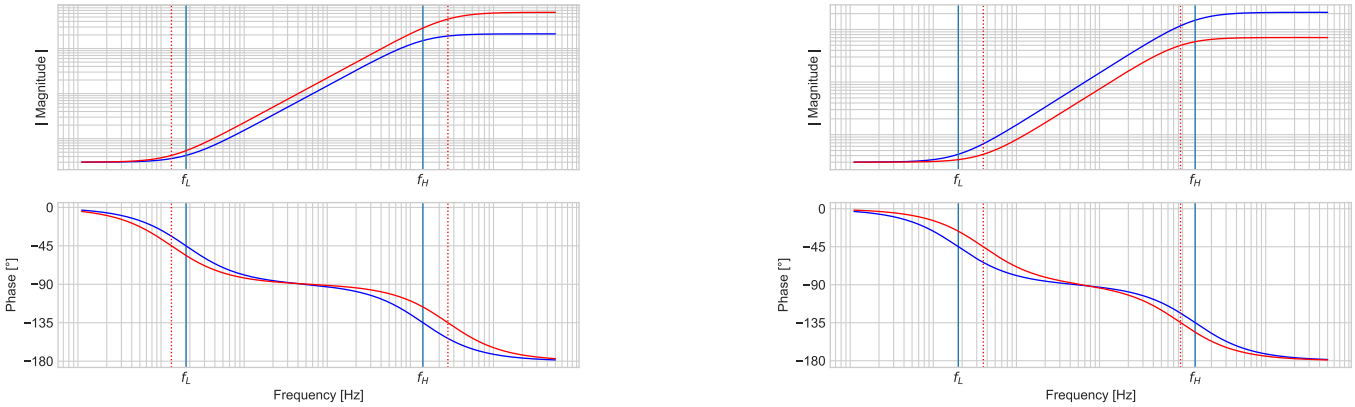


(a) Variation $\Delta L_p < \Delta M$

(b) Variation $\Delta L_p > \Delta M$

Figure 4.19 – Variations in inductance values $L_p$ and $M$. In blue, the signal without sample, and in red, the signal with sample.

inductive range, but the variation will be less pronounced.

You can also measure the impact of the sample on the phase shift, but avoid the purely inductive range (i.e. 90°) or the extremes (0° or 180°), as these ranges are less affected by the sample. Instead, we recommend measuring phase shifts around $f_L$ and $f_H$ to be sure of measuring a variation large enough to be detected.

In any case, the impact of the sample is **relative**. In other words, we are measuring a difference between the state without sample and the state with sample. This is why it is worth using a differential system for the final design of the biosensor.

### 4.2.3 Operating mode

In the next sections, we will study the frequency response of the induced voltage as a function of the different samples available. First, we will study the variation as a function of surface area, then as a function of thickness, then as a function of position on the inductance, and finally, we will highlight the measurement of the different concentrations presented in section 4.1.3.

We supply the external exciting coil with a voltage of 1 V. The voltage induced across the sensing coil is measured by the MFLI. The phase of our signal is measured relative to the input signal. The maximum frequency spectrum of the MFLI is swept for 101 measurements with logarithmic spacing from 1 kHz to 5 MHz.

For each measurement, each sample is measured 5 times, with each sample interchanged between each measurement, to highlight the repeatability of the measurements. The average of the measurements and the standard deviation are displayed as amplitude/phase graphs of the induced voltage. A large standard deviation indicates sensitivity to electromagnetic noise, or a problem of repeatability between two measurements.

In order to highlight the variation induced by the sample, 3 frequencies are chosen: the first $f_L$, the theoretical frequency based on the preliminary studies of the previous sections, where we pass into the inductive domain, $f_M$, the theoretical frequency where the induced voltage

reaches 90° and a third frequency chosen arbitrarily where the variation seems relevant to be highlighted.

The frequencies $f_L$ and $f_M$ are calculated from (4.5) and (4.6) such that:

$$f_L = \frac{V_0}{V_{in}} \cdot \frac{Rp}{2\pi M} = \frac{5.4 \cdot 10^{-5}}{1/\sqrt{2}} \cdot \frac{1.73}{2\pi 0.25\sqrt{8.37 \cdot 10^{-7} \cdot 2.38 \cdot 10^{-7}}} = 6.72 \text{ kHz} \tag{4.10}$$

$$f_M = 10^{\frac{\log(f_L)+\log(F_H)}{2}} = 257.99 \approx 258 \text{ kHz} \tag{4.11}$$

With $V_{in}$, the $\frac{1}{\sqrt{2}}$ volt generator voltage in Root Mean Square (RMS), and $f_M$ taken from the fact that $f_L$ and $f_H$ are the frequencies where the phase passes through 45° and 135° respectively, and according to a logarithmic relationship, half the distance corresponds to 90°. These frequencies are based on models and measured values. As we shall see, these will be slightly offset from the phase shifts targeted by these frequencies. In addition, we will choose as a third arbitrary frequency 50 kHz, which represents a frequency close to the true frequency $f_M$, where the phase shift is 90° and amplitude variations are greatest.

Once the measurements of the phase and amplitude of the induced voltage have been put forward, we will illustrate the relative ratio (Eq. (4.12)) of variation as the absolute difference between the induced voltage measured without samples, $V_{out_0}$, and the induced voltage measured with sample N, $V_{out_N}$, divided by the voltage without sample, thus giving the ratio of variation due to the presence of the sample.

$$Ratio = \frac{|V_{out_0} - V_{out_N}|}{V_{out_0}} \tag{4.12}$$

### 4.2.4 Variation of sample surface

In this section, we will vary the surface area of our samples. To simplify reading the results, we will confine ourselves to varying the surface area of a single layer. From Table 4.7, we have highlighted in blue the samples used (Table 4.8).

| | Cristallin | | | Amorphous | | |
|---|---|---|---|---|---|---|
| | 1 mm² | 1 cm² | 5 cm² | 5 cm² | 1 cm² | 1 mm² |
| 1 layer | Cri-1mm-1L | Cri-1cm-1L | Cri-5cm-1L | Am-5cm-1L | Am-1cm-1L | Am-1mm-1L |
| 2 ou 5 layers | Cri-1mm-2L | Cri-1cm-5L | Cri-5cm-5L | Am-5cm-5L | Am-1cm-5L | Am-1mm-2L |
| 3 ou 10 layers | Cri-1mm-3L | Cri-1cm-10L | Cri-5cm-10L | Am-5cm-10L | Am-1cm-10L | Am-1mm-3L |

Table 4.8 – Highlighting the samples used and their abbreviations

Both types of sample have a high relative magnetic permeability, suggesting an increase in total system inductance. As discussed in section 4.2.2, this increase in inductance should translate into a higher induced voltage than that measured at no load, and an accelerated phase shift in the direction of -90°, then -180°. Furthermore, a larger surface area is likely to have a greater impact on the system than a smaller one. For example, an area limited to the secondary inductance will only influence the secondary inductance and the mutual inductance. However, an extended area will also affect the primary inductance, on which the frequency $f_L$ is based, intensifying the frequency phase shift towards -90°.

#### Absolute measurements

Figure 4.20 shows the amplitude and phase measurements of the voltage induced across the sensitive inductor. Figure 4.20a shows measurements taken with crystalline samples, and

Fig. 4.20b with amorphous samples.

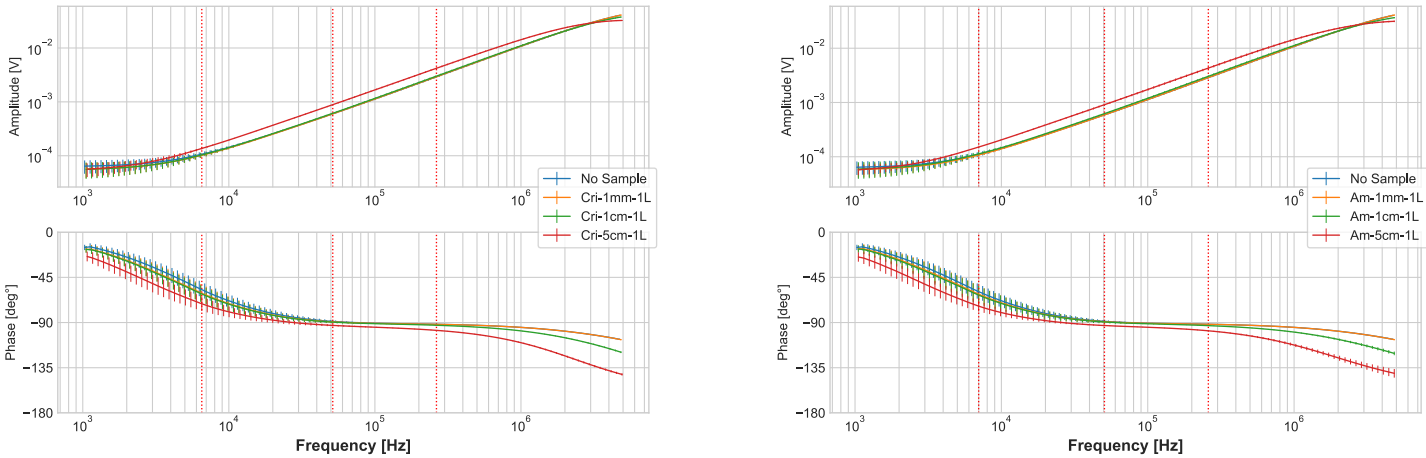


(a) Crystalline samples

(b) Amorphous samples

Figure 4.20 – Absolute measurements of induced voltage when samples with different surfaces are present. The dotted red lines represent the specific frequencies chosen for the analysis of future graphs

.

As expected, we observe a rise in voltage and an accentuated phase shift for a larger surface area. A noticeable noise is also perceptible at low frequencies, a phenomenon already detected during the no-load measurement (see Section 4.2.1).
Variation predictions appear to be consistent. In particular, the induced voltage fluctuates significantly around a 90° phase shift. In addition, a surface encompassing both inductances leads to a significant variation in mutual inductance. This is manifested by a much earlier changeover to -135°, implying a much reduced frequency.

### Absolute measurements at specific frequencies

When measuring specific frequencies, measurements are grouped by sample. The measurements in blue represent the mean and standard deviation at frequency $f_L$. The measurement in red is made at an arbitrarily chosen frequency corresponding to the greatest amplitude variation, and the last frequency corresponds to the theoretical $f_M$ frequency.

In Fig 4.21, amplitude variation is not very pronounced in absolute terms, and we can see an increase closer to a logarithmic approximation as a function of surface area than a linear variation.
In contrast, the absolute phase variation is a little more pronounced, particularly at frequency $f_L = 6.7$ kHz. But as the high standard deviation shows, this frequency is subject to a fair amount of noise.

In addition, the phase variation shows an error in the prediction of frequencies $f_L$ and $f_M$. This would normally indicate the intersection between the phase and the 45° and 90° axes.

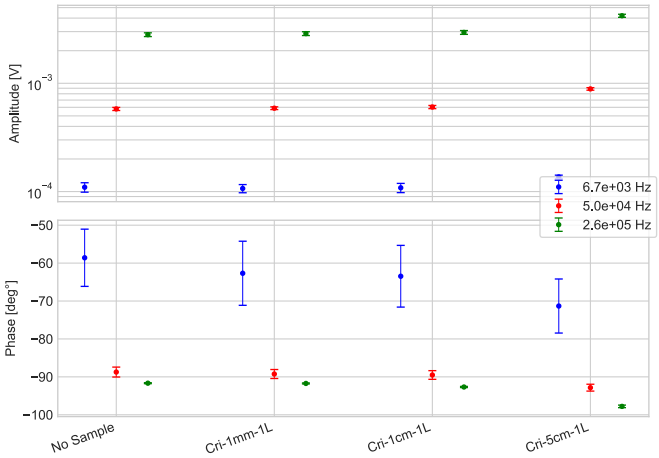


(a) Crystalline samples

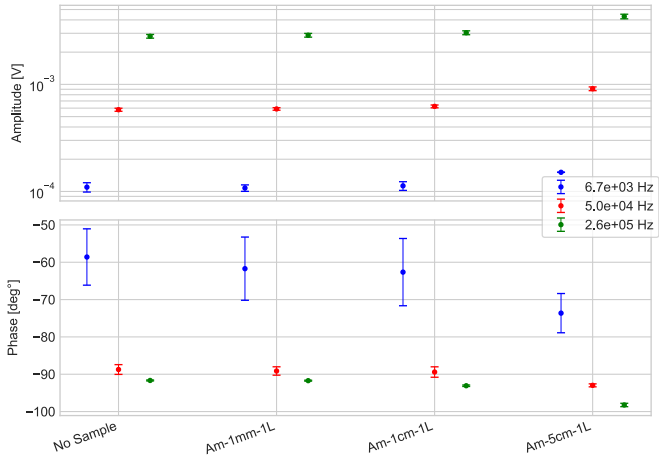


(b) Amorphous samples

Figure 4.21 – Absolute measurements at three specific frequencies : the theoretical frequency $f_L$ where the phase shift is 45°, the frequency chosen arbitrarily around the real 90° phase shift and the frequency $f_M$ corresponding theoretically to the 90° phase shift

.

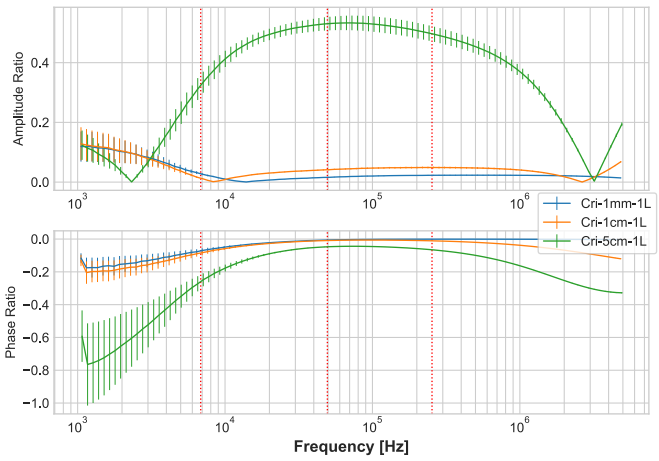


(a) Crystalline samples

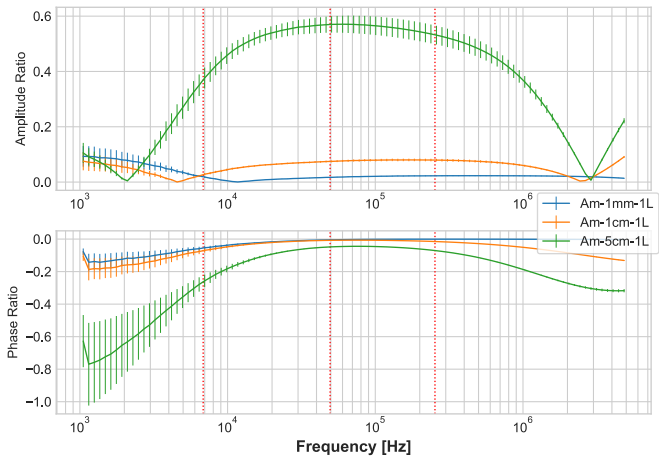


(b) Amorphous samples

Figure 4.22 – Relative measurements of samples versus induced voltage without sample: $\frac{|V_{No\ Sample} - V_{Sample}|}{V_{No\ Sample}}$. With $V_{No\ Sample}$, the measured induced voltage with no sample on the inductors, and $V_{Sample}$, the induced voltage with a sample (Cri-1mm-1L, Cri-1cm-1L or Cri-5cm-1L) on the inductors.

### Relative measurements

Relative measurements are visually more interesting than absolute ones. As can be seen in Fig 4.22, the larger surface area implies a much greater variation in amplitude. We find a relative ratio of around 0.45 against less than 0.1 for smaller surfaces.

In addition, as mentioned several times, we can also highlight the opposition between phase measurement and amplitude measurement. On the one hand, if you want to measure a strong amplitude variation, you have to look at the 90° range. But when it comes to phase variation, it is better to look at transitions, i.e. around 45° and 135°.

Another point to raise is the greater variation on the amorphous side than on the crystalline side, which contradicts the prediction made in relation to permeability, where a higher permeability translates a higher variation. This point is developed in Section 4.2.6.

### Relative measurements at specific frequencies

Figure 4.23 accentuate the exponential profile (Section 1.1) of amplitude variation in relation to surface area. Thus, between a surface of 1 mm² and 1 cm², the variation is relatively minor, even almost non-existent. However, the change becomes much more marked when comparing 1 cm² to 5 cm². This trend can be explained by the fact that the surface area of the sample also increases exponentially.

Furthermore, in terms of amplitude, although the arbitrary frequency chosen dominates the other two frequencies when measuring voltage with a large sample area, the theoretical frequencies $f_L$ and $f_M$ are not necessarily very far apart. This observation shows that, although frequency selection is essential to maximize detection, this decision is less constraining for amplitude than for phase shift. Indeed, for the phase shift, the fluctuation is much more pronounced at low frequency $f_L$. The theoretical frequency $f_M$, being underestimated, would have shown a clearer divergence from the arbitrary frequency if it had been estimated with greater precision.

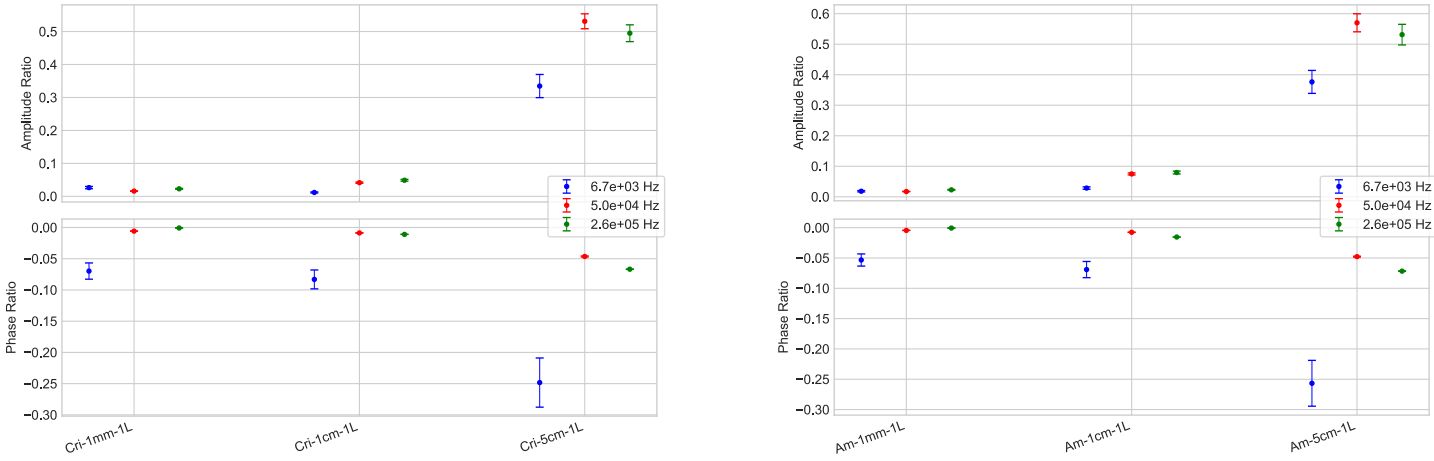


(a) Crystalline samples

(b) Amorphous samples

Figure 4.23 – Measures relating to specific frequencies

**Conclusion**

These initial observations of the surface indicate that it is better to have a larger surface area in order to achieve greater variation. Not surprisingly, the larger the surface area, the greater the impact on the primary and mutual inductances on which our frequency response depends. What's more, amplitude or phase measurement is entirely possible, depending on the frequency at which the measurement is made.

### 4.2.5 Sample thickness variation

We now turn to the variation in thickness of the ferromagnetic material. Once again, the samples used are highlighted in Table 4.9. This time, we keep the median surface, i.e. 1 cm². We expect little variation on the low-frequency side $f_L$ due to the surface not impacting the primary inductance. Logically, the greater the thickness, the greater the impact on overall inductance.

| | Cristallin | | | Amorphous | | |
|---|---|---|---|---|---|---|
| | 1 mm² | 1 cm² | 5 cm² | 5 cm² | 1 cm² | 1 mm² |
| 1 layer | Cri-1mm-1L | Cri-1cm-1L | Cri-5cm-1L | Am-5cm-1L | Am-1cm-1L | Am-1mm-1L |
| 2 ou 5 layers | Cri-1mm-2L | Cri-1cm-5L | Cri-5cm-5L | Am-5cm-5L | Am-1cm-5L | Am-1mm-2L |
| 3 ou 10 layers | Cri-1mm-3L | Cri-1cm-10L | Cri-5cm-10L | Am-5cm-10L | Am-1cm-10L | Am-1mm-3L |

Table 4.9 – Highlighting the samples used and their abbreviations

Again in this section, we will highlight 4 pairs of graphs as in the previous section: two pairs of graphs presenting the absolute measurement over the whole frequency spectrum and at specific frequencies, and two pairs of graphs of measurements relative to the no-load measurement over the whole spectrum and also at specific frequencies.

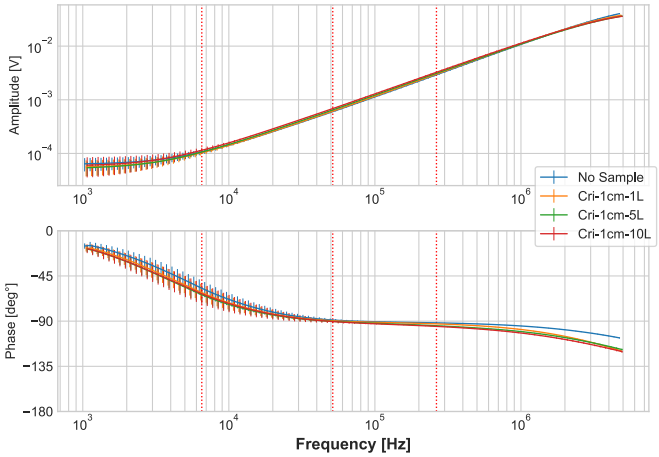


(a) Crystalline samples

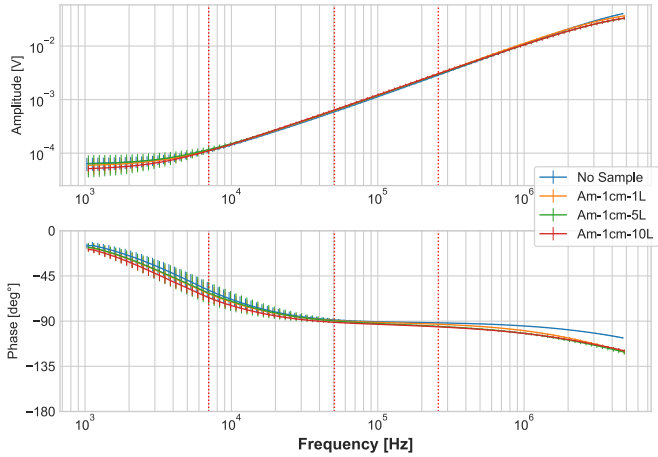


(b) Amorphous samples

Figure 4.24 – **Absolute** measurements with and without samples, varying sample thickness. Dotted vertical lines represent specific frequencies for measurement comparison

.

For this series of measurements, the variations are more subtle. Looking the graphs in Figs. 4.24a and 4.24b, a general trend can be observed when a sample is present: there is an increase in the inductance value. In other words, as mentioned earlier, there is an increase in amplitude between $f_L$ and $f_H$ and a phase shift that occurs earlier around $f_L$ and $f_H$. However, these variations are modestly perceptible on absolute measurements, particularly on Fig. 4.25. We

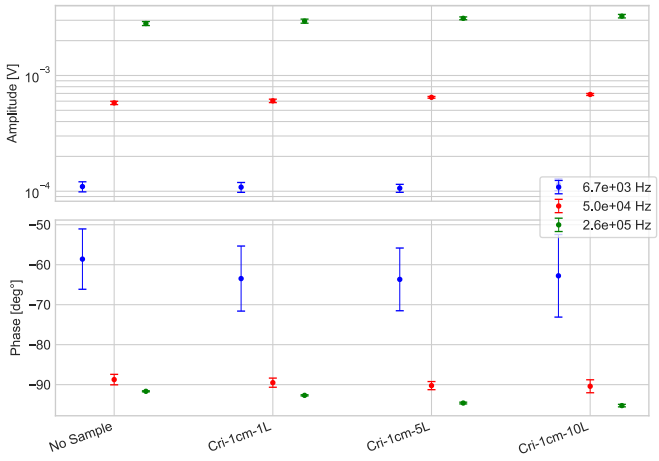


(a) Crystalline samples

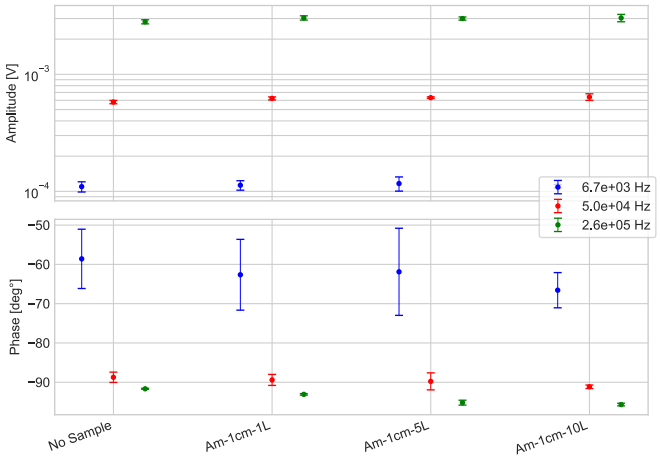


(b) Amorphous samples

Figure 4.25 – Comparisons of **absolute** measurements with and without frequency-specific samples

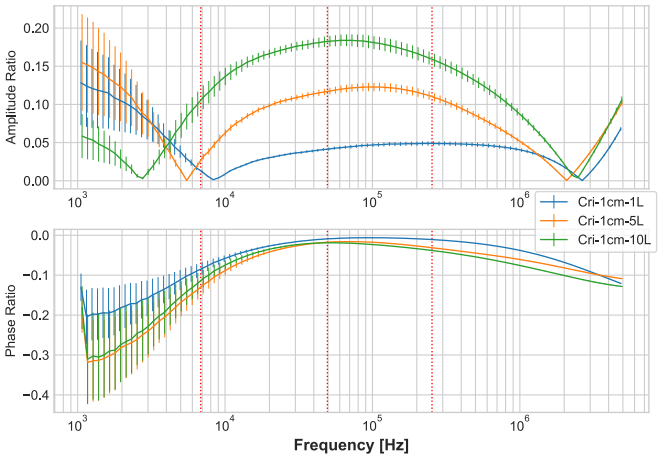


(a) Crystalline samples

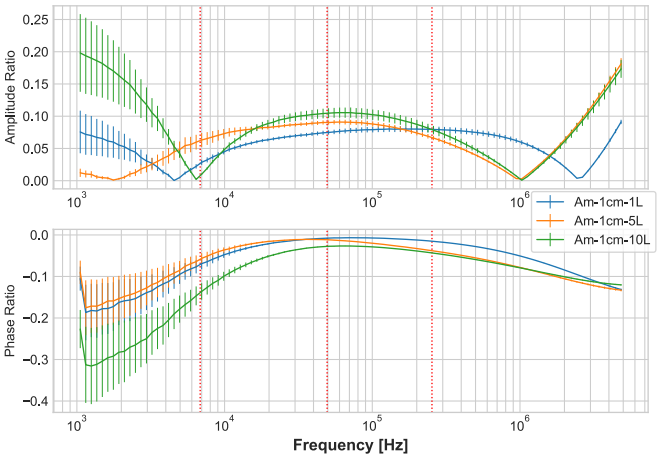


(b) Amorphous samples

Figure 4.26 – **Relative** measurements of samples by varying their thickness. Dotted vertical lines represent specific frequencies for measurement comparison

.

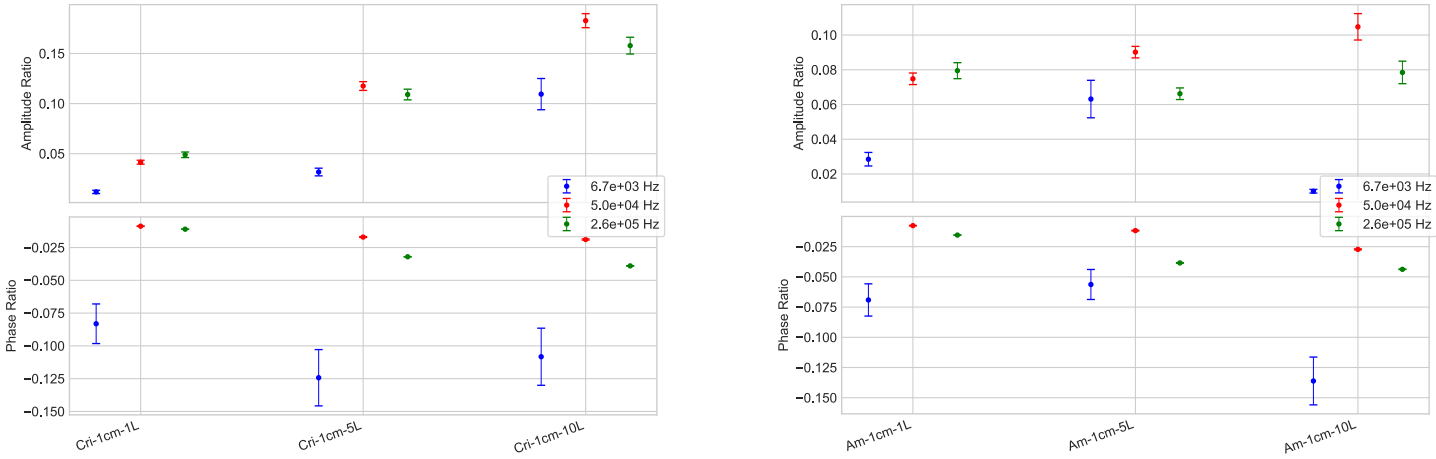


(a) Crystalline samples

(b) Amorphous samples

Figure 4.27 – Comparisons of **relative** measurements with and without frequency-specific samples

can see a slight increase, which could be likened to a linear progression, but our observations do not go any further.

On the other hand, on the graphs of relative measurements in Figs. 4.26 and 4.27, it is a little more marked.
As we assumed, increasing the thickness causes the induced voltage to vary linearly, both in amplitude and phase. This is particularly apparent in the relative amplitude variation (Fig. 4.27a) of crystalline samples.

Amorphous samples react differently. There is a limit at around the 0.10 relative ratio on the Fig. 4.26b. This can be due to two factors: an operator problem or a magnetic property problem such as saturation or magnetic penetration.
For an operator problem, a sample problem would introduce outliers and thus result in a much higher standard deviation. But here, the three curves, taken separately, seem coherent.
We're more inclined to think in terms of magnetic properties. As we vary the thickness, we could evoke a problem of magnetic penetration.

As illustrated in Fig. 4.28, the magnetic field is channeled within the sample, following the field lines created by the inductance as closely as possible. If the thickness of the sample increases, this does not necessarily mean that the magnetic field will penetrate further inside. One hypothesis is that the amorphous nature of our ferromagnetic material could limit this magnetic penetration, which would explain the curve observed on our graph. To substantiate this assumption, it would be wise to undertake an in-depth study of the fluctuation in thickness of the amorphous material, or to test other ferromagnetic materials with a lower permeability than our amorphous material. This would enable us to determine whether they respond in the same way, or even more intensely, to our set of inductances.

### 4.2.6 About magnetic saturation

Another concern is the greater variation with an amorphous sample than with a crystalline one, notably visible in Fig. 4.23 where we have a relative ratio of $\approx 0.5$ maximum for the crystalline against $\approx 0.6$ for the amorphous. As can also be seen from the graphs 4.26

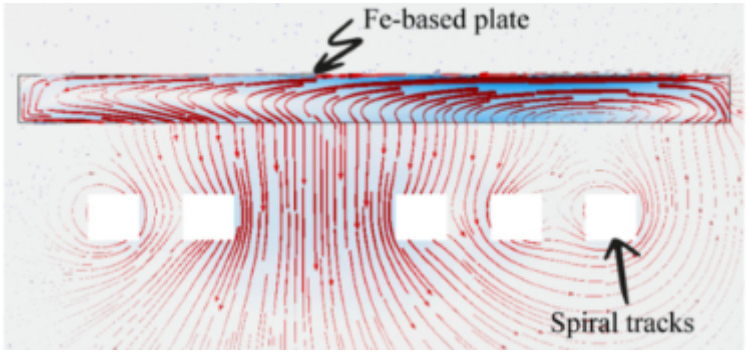


Figure 4.28 – Illustration of magnetic behavior in a ferromagnetic sample [127]

and 4.27, if we look at the measurement for the first thickness at 50 kHz, the relative measurement of the amorphous sample is much greater ($\approx 0.08$) than the crystalline sample ($\approx 0.02$).

Figure 4.29 highlights the above-mentioned differences. For the same surface area and thickness, in addition to the problem of magnetic penetration, the amorphous sample produces a greater variation in inductance than the crystalline sample, which is contrary to what was predicted in theory (Section 4.2.2).

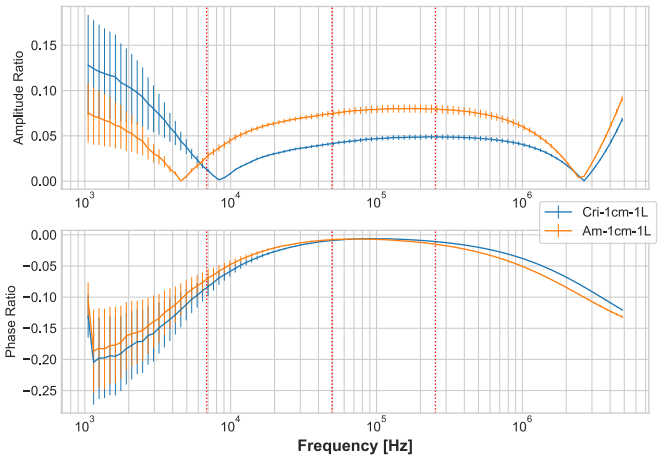


(a) **Relative** measurements of a crystalline sample and an amorphous sample

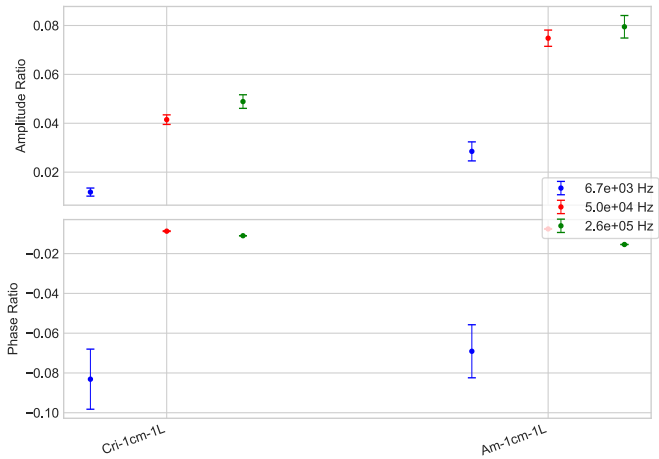


(b) **Relative** measurements with specific frequencies

Figure 4.29 – Evidence of inconsistency of amorphous sample amplitude greater than crystalline sample amplitude

This phenomenon is explained by magnetic saturation. Indeed, if we look at the characteristics of our samples as communicated by the manufacturer (Table 4.10), we discover that amorphous ferromagnetic material has a higher magnetic saturation than crystalline material.

The magnetic permeability describes the linear behavior between the exciting field and the magnetic field inside the material, as described in Section 1.2.3. In a ferromagnetic material, this behavior is linear only within a limited range, but for the sake of simplicity, let us assume that this behavior is linear.

| | Fe-based Amorphous | Fe-based Nanocrystallin |
|---|---|---|
| Saturation Flux Density Bs(T) | 1.56 | 1.25 |
| Initial Permeability µi | 5 000 | 80 000 |
| Max Permeability µm | 50 000 | 400 000 |

Table 4.10 – Magnetic characteristics of samples

Simulate the magnetic field as :

$$B_0(V_{in}, f) = \frac{i \cdot L_s}{S_{eq}} = \frac{V_{in}}{Z_p} \cdot \frac{L_p}{S_{eq}} \tag{4.13}$$

with $S_{eq}$, the equivalent surface worth $d_{avg} \cdot N$. Let us take an input voltage of 1 V for 1 MHz. Using conventional inductance data, we obtain :

$$B_0(1, 10^6) \approx 60 \text{ µT} \tag{4.14}$$

This is well below our saturation magnetic field! Let's continue by saying that this value is valid in the vicinity of the material. We know that in the material we have :

$$\mu_0 \mu_r B = \mu_r B_0 = B_M \tag{4.15}$$

If we multiply our magnetic value by the maximum relative magnetic permeability of our materials, we find :

$$B_{M_{am}} = 50000 \cdot 60 \cdot 10^{-6} = 3 \text{ T} \tag{4.16}$$

$$B_{M_{cri}} = 400000 \cdot 60 \cdot 10^{-6} = 24 \text{ T} \tag{4.17}$$

We can see that we can easily reach our saturation values within the material. This time, let us apply our various formulas with an input voltage of 0.5 V, so that the material desaturates in our frequency range of application. We obtain Fig.4.30 giving the magnetic field produced by our external inductance as well as the magnetic field within our different materials.

Figure 4.30 shows that around 1 MHz, the amorphous material is no longer saturated, and around 10 MHz, it is the crystalline material's turn to become unsaturated. So, if our calculations are correct and we apply a voltage of 0.5 V at the input, we should see a reversal of trends at around 1 MHz.

Remember that the magnetic field $B_M$ within the material is the main element influencing our inductance, and it is this magnetic field that will induce more or less voltage in our sensitive inductance. Figures 4.31 and 4.32 represent the same analyses as above, except that this time we are analyzing frequencies at 100 kHz, 1 MHz and 2.5 MHz, which represent states during saturation and after desaturation. Beyond these frequencies, the $f_H$ frequency is exceeded, and the relative ratio, because of its absolute nature, gives a truncated value.

As can be seen, the amorphous material has a higher amplitude value before 1 MHz, and above this value, the crystalline material is above, as predicted by theory. Of course, the models employed are ideal, and the predicted amorphous desaturation frequency may differ slightly from the measured one.
This phenomenon is best represented Fig. 4.32b. We can see that the blue (100 kHz) and red (1 MHz) markers in the relative amplitude ratio are lower in the crystalline case than in the amorphous, and become higher than the amorphous value with the green (2.5 MHz) markers.

This phenomenon shows that the amplitude of the magnetic field generated and the magnetic saturation of the materials studied must not be neglected. As nanoparticles behave differently from a simple ferromagnetic material, this remark may not be valid and requires further research.

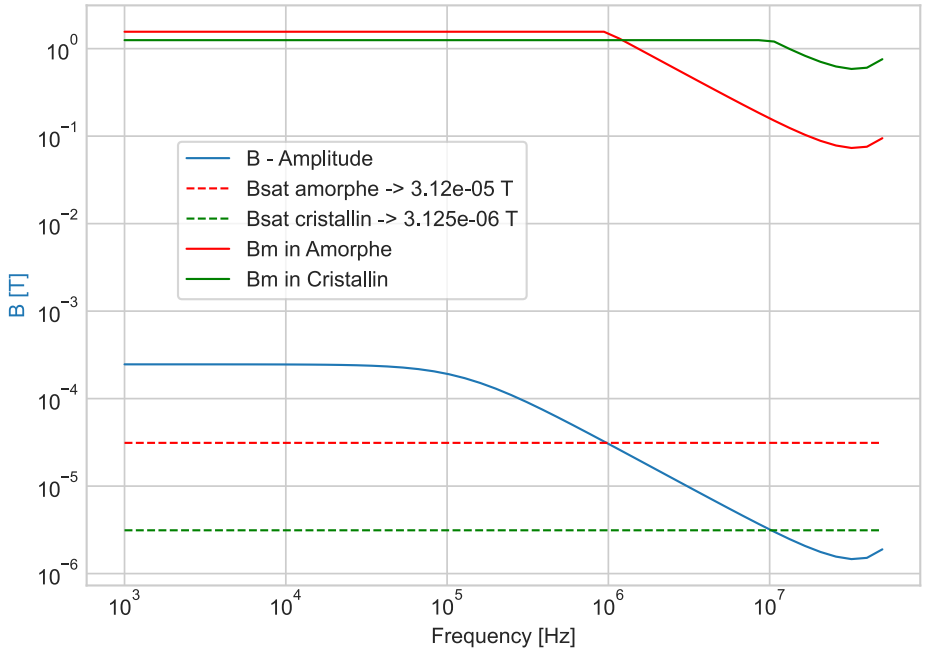


Figure 4.30 – Simulation of the magnetic field produced by inductance (blue), the magnetic field inside crystalline material (green) and amorphous material (red). The dotted lines represent the thresholds beyond which $B$ saturates the materials.

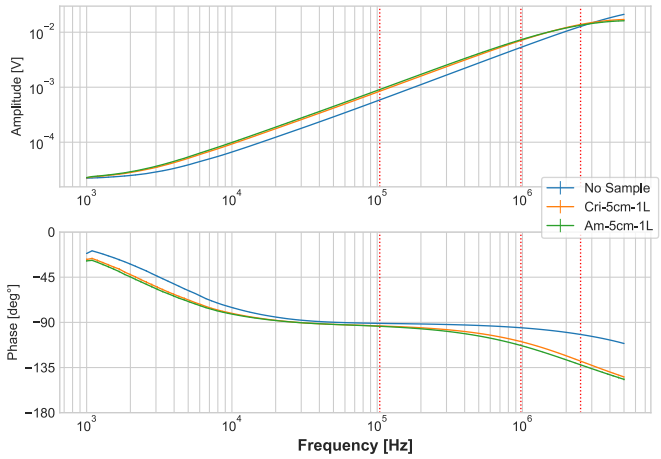


(a) **Absolute** measurements of induced voltage. The 3 vertical dotted lines represent the specific frequencies used to compare measurements

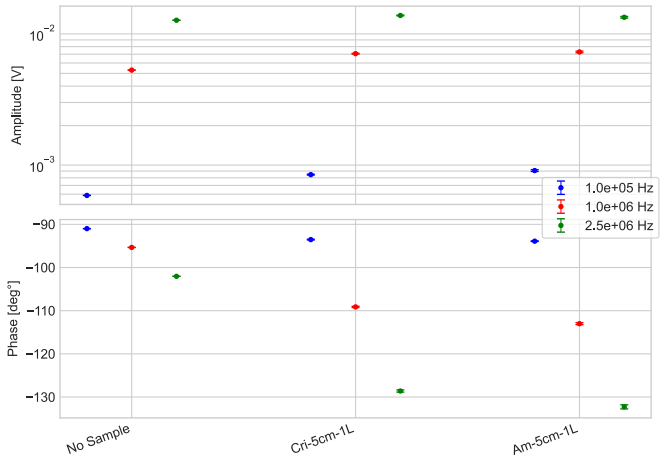


(b) Comparisons of absolute measurements at given frequencies

.

Figure 4.31 – **Absolute** measurements with and without samples at 0.5 V input voltage to highlight magnetic saturation

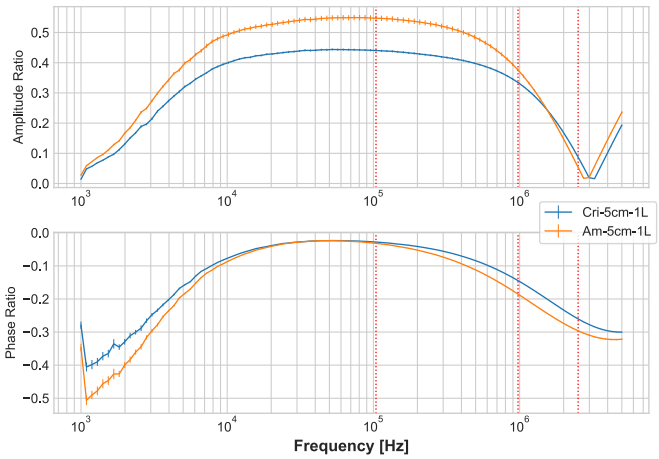


(a) **Relative** measurements of induced voltage

.

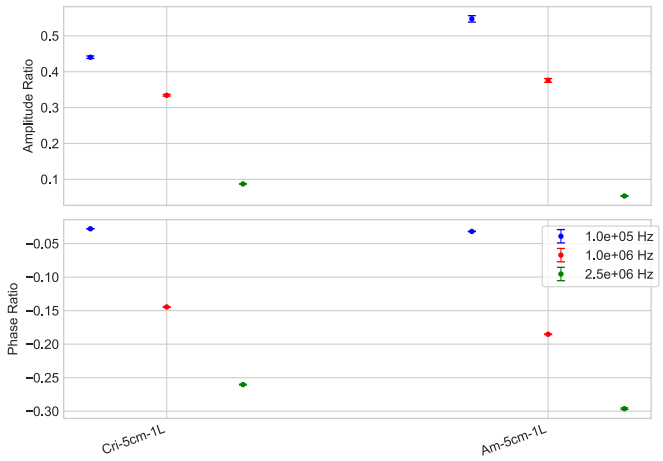


(b) Comparisons of **relative** measurements relating to specific frequencies

Figure 4.32 – **Relative** measurements of samples at 0.5 V input voltage to highlight magnetic saturation

### 4.2.7 Variation of sample position

The final modification explored for our planar inductors concerns the positioning of the samples on them. For this purpose, we use a nanocrystalline sample with a surface area of 9 mm² and composed of a single layer (Fig. 4.33a). This size was chosen because it is large enough to guarantee a meaningful measurement without being too cumbersome, and to overlap several positions studied simultaneously. The choice of material and number of layers is arbitrary.

We also use a different set of inductors (Fig. 4.33b) from the one initially presented. This new pair of inductors features an outer inductor with a larger inner diameter, making it easier to measure the sample when placed between the two inductors. Apart from this change of equipment, the experimental procedure remains unchanged.

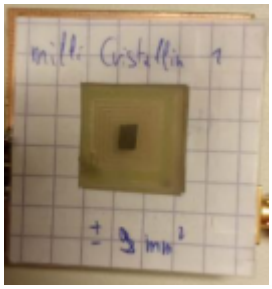

(a) 9 mm² crystalline sample

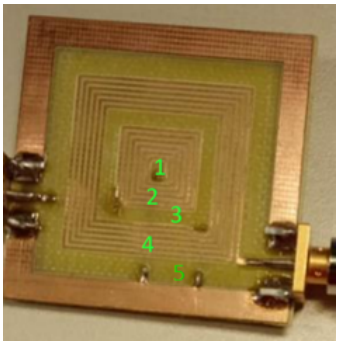


(b) A pair of inductances whose separation is greater than the pair previously presented. Five positions are highlighted

.

Figure 4.33 – Presentation of the material used to highlight the variation in position

For this experiment, we move the sample to five different positions:

1. The center of the two inductors

2. On the loops of the internal inductance
3. Between the internal and external inductances
4. On the outer inductance loops
5. Outside inductances

The samples are too small to see any variation in the absolute measurements, so we won't show them here. On the other hand, Figs. 4.34a and 4.34 show the variation in induced voltage as a function of sample position.

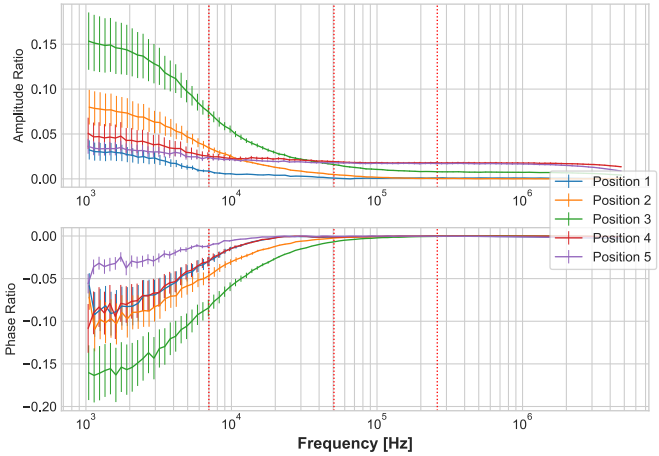


(a) **Relative** measurements of induced voltage

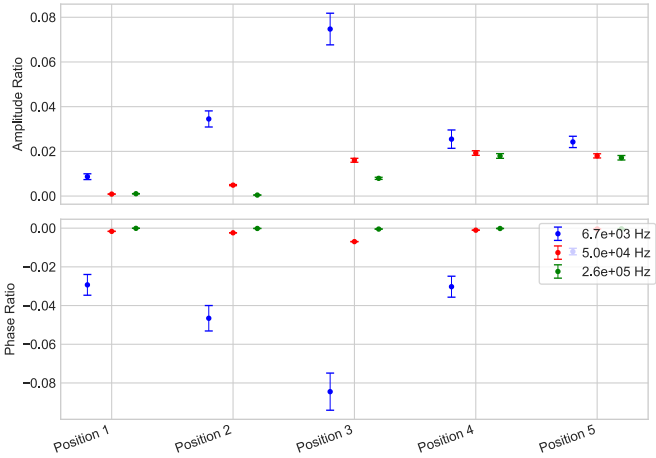


(b) Comparisons of **relative** measurements to specific frequencies

Figure 4.34 – **Relative** measurements of sample displacement at five different positions

It is clear that position mainly influences low frequencies. At high frequencies, the impact is marginal. Furthermore, it should be noted that the sample positioned outside the inductors (position 5) generates almost the same voltage variation as the other positions.

At low frequencies, the position with the greatest effect on the inductance value is the one between the two inductances (position 3). A plausible interpretation would be that energy exchange between the two inductors is maximized at this position.

But why is the position only relevant at low frequencies? To tell the truth, we have no concrete hypothesis on this subject. Is it related to wavelength versus material thickness? Or is there a capacitive effect of the material on the inductances? More detailed analysis of the ferromagnetic properties of our samples and the magnetic behavior of our inductors would be needed to decide. A finite element simulation of the device as a whole could probably shed some light on the matter.

## 4.3 Conclusion and perspectives

In conclusion, the first major point to remember about measuring ferromagnetic samples on a system of coplanar and concentric exciting/sensing inductors is that it is possible to measure the induced voltage, and therefore the variation in inductances produced by these samples, in both **amplitude**and **phase**.

It is essential to note that this measurement is **relative**. In other words, a sample-free voltage measurement is required for quantitative detection of magnetic samples.

For amplitude measurement, we recommend inductive range at frequency $f_M$, where the offset is **-90°**. As for phase detection, it is preferable to measure either close to voltage $f_L$, resulting in a phase shift of **-45°**, or at frequency $f_H$, where the phase shift is **-135°**.

As far as sample dimensions are concerned, we recommend choosing a sample that covers the entire surface of the inductor and is of optimum thickness, thus guaranteeing maximum variation.

If the sample cannot cover the entire inductance, it can be positioned between the two inductances for low-frequency measurement, or close to or even on the external inductance for high-frequency measurement.

## 4.4 Measuring MNP concentration

Let us move on to the measurement of magnetic nanoparticle concentration. Figure 4.35 shows the absolute measurement of the various concentrations presented in Section 4.1.3. As you can see, the induced variation is far too small to be seen by the naked eye; all we see is the base voltage induced by the external coil.

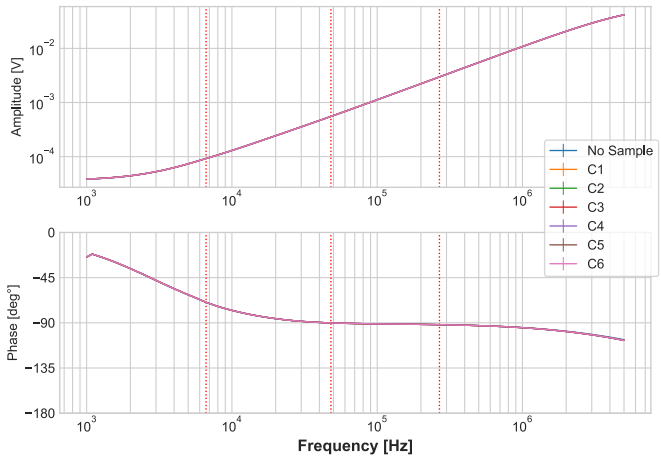


(a) **Absolute** measurements on the frequency spectrum

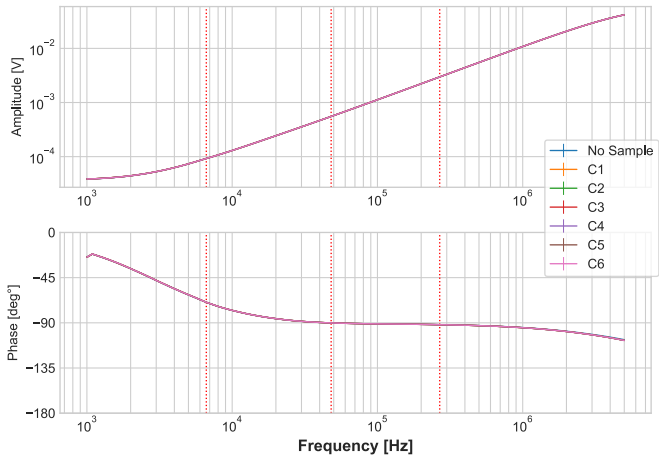


(b) **Absolute** measurements at specific frequencies

Figure 4.35 – **Absolute** measures of the concentration of samples of magnetic nanoparticles

So we move on to relative measurements in Fig. 4.36. Our first observation is that we are indeed detecting something, but this conclusion may be a little strong in view of the significant noise present in our measurements.
In Section 3.1.2, we talked about the average noise of a $10^{-7}$ V magnitude. If we look around the frequency $f_L = 6.7$ kHz, our relative ratio of $\approx 0.\ 001$ (Fig. 4.36b) and the absolute signal amplitude of $\approx 10^{-4}$ V (Fig. 4.35b) gives us a variation of around $0.001 \cdot 10^{-4} = 10^{-7}$ V, of the same order of magnitude as our resistive noise. This initial conclusion suggests that we need to work at higher frequencies, so that the basic induced voltage allows a variation greater than the

intrinsic noise.

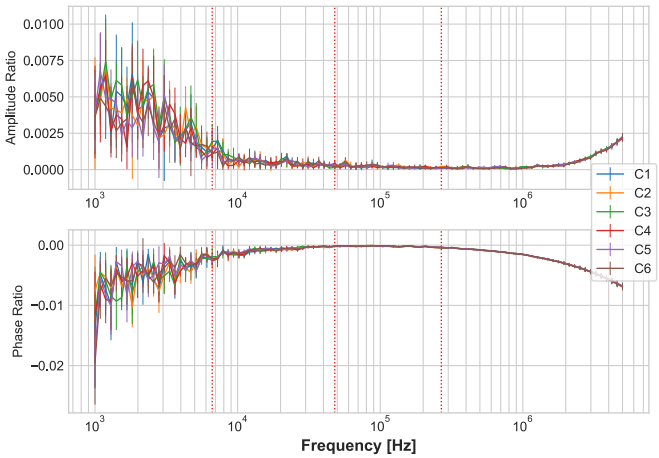


(a) **Relative** measurements on the frequency spectrum

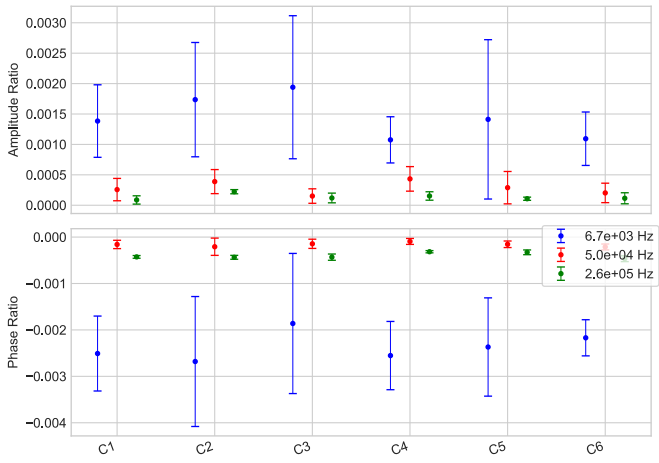


(b) **Relative** measurements to specific frequencies

Figure 4.36 – **Relative** measurements of the concentration of samples of magnetic nanoparticles

Indeed, looking at frequencies at 50 kHz (Fig. 4.37a) and 260 kHz (Fig. 4.37b), the standard deviation is much smaller than at the low frequency. Once again, the measurements prove that we do detect something, whether in phase or amplitude, but this detection is really low and remains highly noisy. What is more, no real linear, exponential or other trends can be confirmed. At present, therefore, our system is based on a simple **qualitative** measurement, and even this can be called into question by the presence of significant noise.

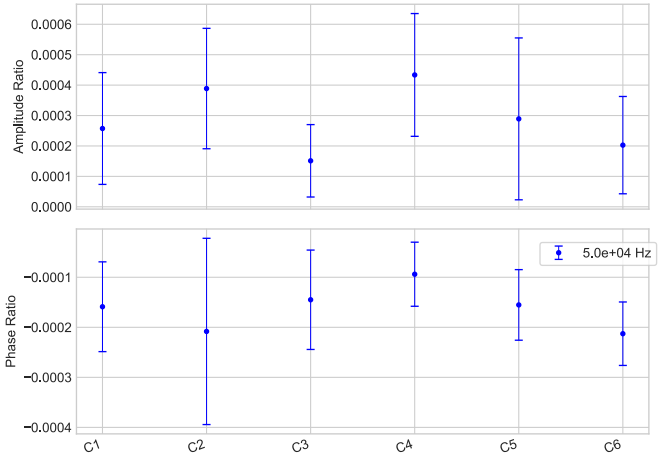


(a) **Relative** measurements to 50 kHz

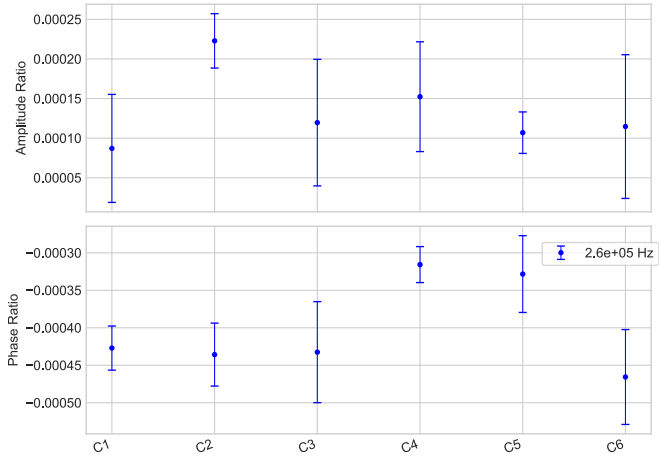


(b) **Relative** measurements to 260 kHz

Figure 4.37 – **Relative** measurements of the concentration of magnetic nanoparticles samples at high frequencies

One way of improving our results would be to optimize the mutual inductance (Section 4.1.2) on which our high-frequency detection depends (i.e. towards $f_H$, the frequency at which the signal phase shift is 135°), notably by changing the ratio of the inductance loops. The theoretical model predicts that mutual inductance is maximum for a ratio of plus or minus 3 loops of

external inductance to 7 loops of internal inductance.

A second possible way of improving nanoparticle detection is to apply the advice given in the previous section 4.3, notably by increasing the surface area and thickness of the sample under the guarantee that the sample has a homogeneously distributed concentration. In addition, we can further optimize our detection by placing the samples between our two inductors, rather than in the center of the sensitive inductor.

A third possible approach would be to modify the geometrical parameters to improve the inductance value (Section 3.1.4), but also to reduce resistive noise, for example, by increasing the width of the wires. Beware that increasing wire width also increases the parasitic capacitance between substrate and inductor.

And of course, the best thing to do is to increase the frequency range studied, in particular by working around the frequency $f_{Q_{max}}$ where the quality factor is maximum, as well as working more around the frequency $f_H$ where the sample induces the most variation. Unfortunately, the MFLI device used in this work restricts us to frequencies below 5 MHz.

# Chapter 5

# Electromagnetic behavior of a differential system

To improve the detection of magnetic nanoparticles, we considered the use of a differential system. As we noted earlier (Section 4.3), the measurement is said to be **relative**, i.e., the measurement of the voltage induced by a magnetic sample is compared with the measurement without a magnetic sample in order to be able to correctly detect a **variation**. In this context, the use of a differential system becomes more than relevant.

The original idea comes from [10], whose equivalent circuit and schematic are shown in Figs. 5.1a and 5.1b.

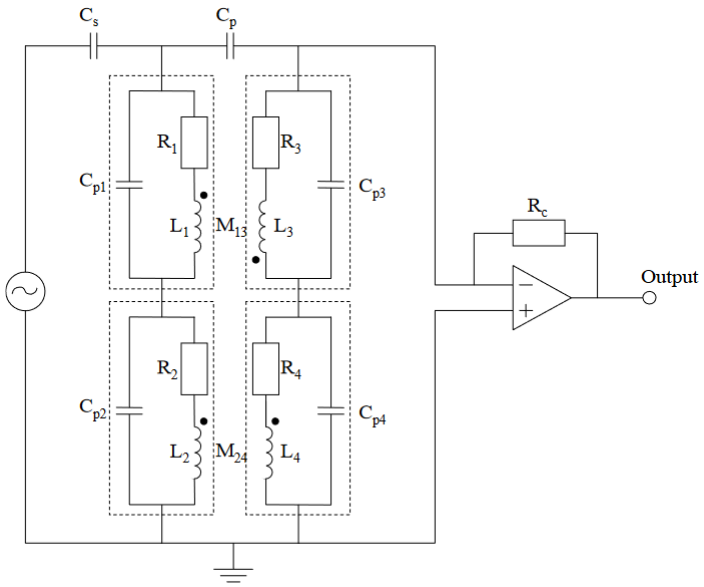


(a) Equivalent circuit : Components 1 and 2 represent primary inductors and components 3 and 4 represent secondary inductors, $C_s$ and $C_p$ represent inter-pair and series parasitic capacitance respectively. The measurement is taken from a voltage-to-current converter circuit.

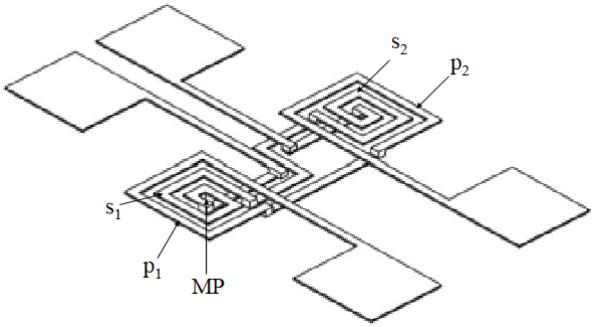


(b) Differential system diagram : $p_1$ and $p_2$ represent the primary inductors of the first and second pair. $s_1$ and $s_2$ represent the secondary inductors of the first and second pair.

Figure 5.1 – Representation of the differential system presented by [10]

Note that the inductances $L_1$ and $L_3$ representing the external and internal inductors of one of the two pairs, are opposite, i.e., their wiring are in opposite directions, the induced magnetic field opposing each other and thus creating an opposite induced voltage. If the system is balanced, i.e., if $L_1 = L_2$ and $L_3 = L_4$ and therefore the mutual inductance is identical within the two pairs, then the induced voltage from the two sensitive inductances $L_3$ and $L_4$ cancel each other out. The presence of a magnetic sample unbalances the system and induces a voltage. This principle is illustrated by the simplified diagram (Fig. 5.2). Equation (5.1) details the mathematical reasoning, which is only valid if there is no current flowing in the secondary coils, a strong assumption given that the voltmeter, despite its very high internal resistance, cannot be considered an ideal open circuit.

A differential system should therefore measure only the variation produced by the presence of a sample influencing the magnetic field intercepted by the sensitive inductors. In theory, we should therefore have a voltage that increases only linearly with frequency, the slope of which is proportional to the magnetic influence. The same applies to phase, which should vary linearly up to 90°.

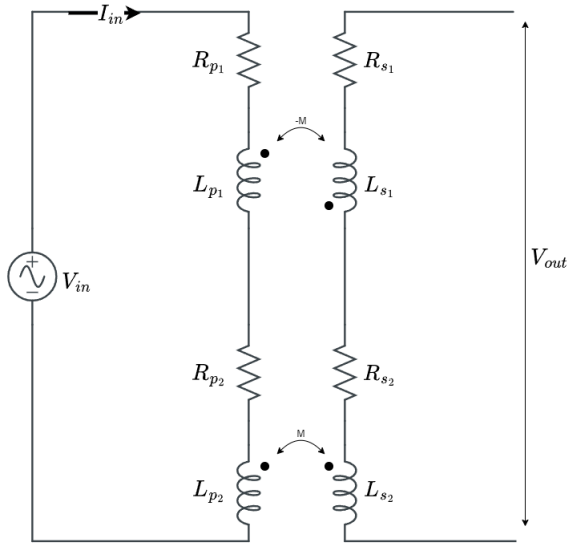


$$\begin{aligned} V_{out} &= \epsilon_1 + \epsilon_2 + j\omega\Phi_{Sample} \\ &= -j\omega M I_{in} + j\omega M I_{in} + j\omega\Phi_{Sample} \\ &= j\omega\Phi_{Sample} \end{aligned} \quad (5.1)$$

Figure 5.2 – Simplified equivalent circuit of the differential system

This chapter therefore seeks to evaluate the possibilities of using a differential system, in particular the one presented by [10].
In this context, we also take the opportunity to test two designs other than the one presented in the previous sections. In Section 4.2.7, we discover that the position of the sample in relation to the inductors can have an impact, as the sample must be between the two inductors to maximize the variation induced. In addition, in order to best capture magnetic variations, it is advisable for the inductors to have the largest possible surfaces. With these two parameters in mind, we decided to create a second design where the inductors would be **interleaved** so that the primary and secondary inductance would be as large as possible, while increasing the mutual inductance. And as a third design, we are testing two inductors with the same surface area, but **superimposed** where the sample will slide between the two.

First, we will develop each design individually, highlighting their electrical characteristics and frequency response in relation to ferromagnetic samples with variable surface area, and

hence variable permeability. Then we will compare the various electrical characteristics and frequency responses between the different designs and the simple exciting/sensing pair. Finally, we close this chapter by presenting the various advantages and disadvantages of each design, as well as outlining the potential for improvement and development.

## 5.1 Specifications of the three differential systems

We have created three differential systems based on a different exciting/sensing pair design:

1. The classic system based on the pair of inductors presented so far, with an internal inductor, and an external inductor.
2. Another so-called « interleaved » system where the two inductors are on the same surface, but the two inductors wind together while being insulated. This design improves magnetic coupling while retaining the constraint of being on a single surface.
3. The final « superposed » system consists of two identical inductors, one on top of the other. The sample is sandwiched between these two inductors. This system allows higher inductance values for the primary and secondary inductors, as well as improved magnetic coupling.

### 5.1.1 Classical system

The « classic » system is illustrated Fig. 5.3. The first connector supplies power to the primary inductors, while the second measures the voltage across the two secondary inductors.

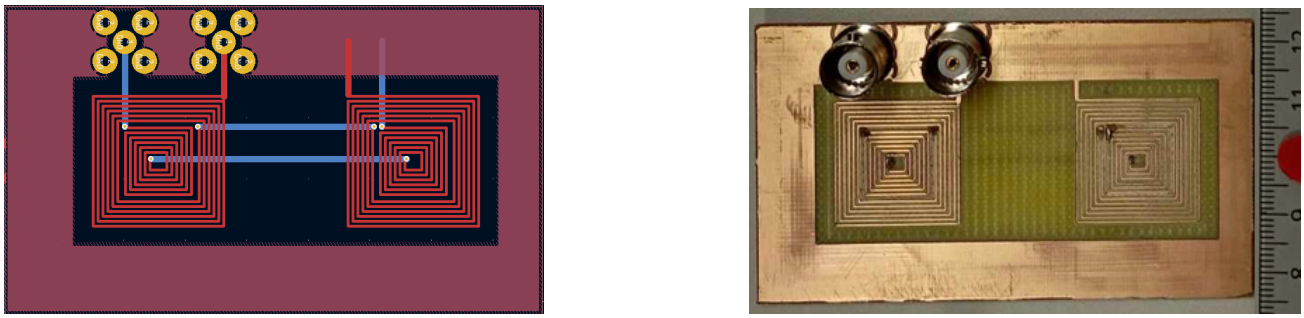

(a) KiCad system diagram

(b) Printed system picture

Figure 5.3 – « Classic » differential system based on the pair of inductors studied above

As a reminder, here are the specifications for the pair of internal/external inductors :

| Primary | | | | | Secondary | | | | | | |
|---|---|---|---|---|---|---|---|---|---|---|---|
| $R_p$ [Ω] | $L_p$ [µH] | $C_p$ [pF] | $f_{Q_{max}}$ [MHz] | $f_{res}$ [MHz] | $R_s$ [Ω] | $L_s$ [µH] | $C_s$ [pF] | $f_{Q_{max}}$ [MHz] | $f_{res}$ [MHz] | $M$ [µH] | $k$ |
| 1.73 | 0.24 | 1.01 | 191.15 | 349.84 | 2.07 | 0.837 | 1.62 | 79.31 | 136.48 | 0.0375 | 0.21 |

Table 5.1 – Specifications of the inductors making up the « classic » differential system

Now let us compare the measurement of single-layer crystalline samples by varying the surface area. This is equivalent to varying the magnetic permeability, allowing us to quickly assess the sensitivity of our detector.

As can be seen Fig. 5.4a, the large standard deviation indicates a lower SNR than when measuring with a single pair. What is more, we can see that the trend of the « No Sample »

curve is not as expected. In fact, a voltage is measured across the sensitive inductors, which is the opposite of what was assumed (Eq. (5.1)). This error is due to the fact that the system is not balanced. This is partly because the primary and secondary inductors are not perfectly identical, but also because the system is not perfectly open, so a current flows and creates a voltage caused by the system's resistance.

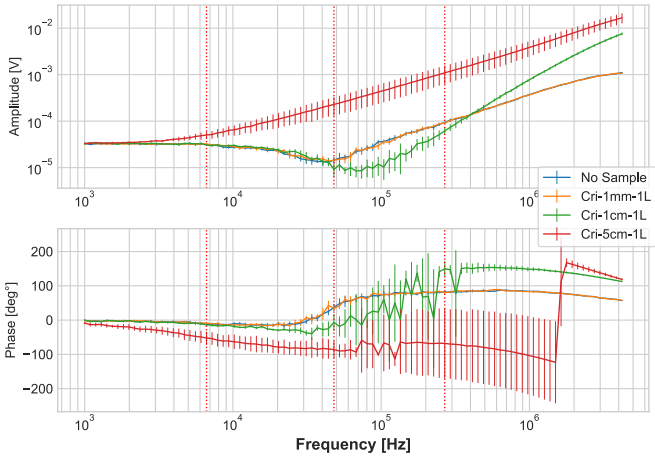


(a) **Absolute** measurements over the frequency spectrum 1 kHz to 5 MHz

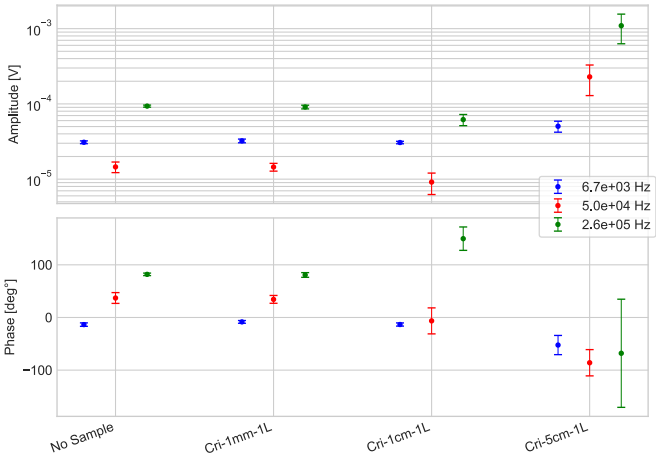


(b) **Absolute** measurements at specific frequencies

Figure 5.4 – **Absolute** measurements of single-layer crystalline ferromagnetic samples with variable surface area

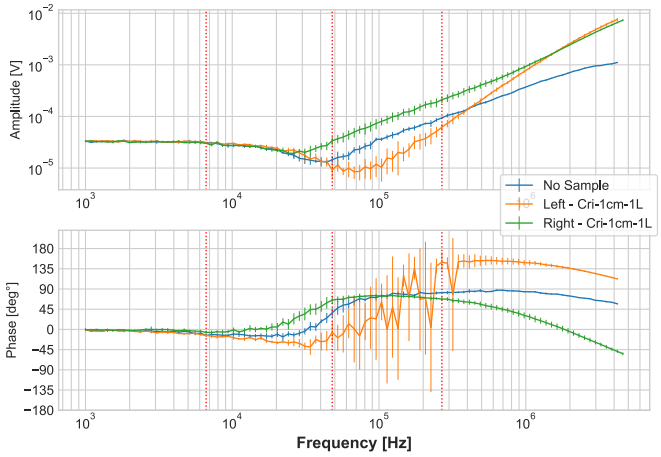


Figure 5.5 – Comparison of induced voltage with a sample on the left pair and a sample on the right pair

In addition, we also find an inconsistency in the phase shift, which should be zero without a sample, but varies up to 90°, symptomatic of a self-inductance, corroborating the thesis of a non-zero current flowing in the secondary inductor. The negative phase shift of the 5 $cm^2$ sample (red curve) is due to the fact that it overlaps both inductors, unlike the other two samples. This negative phase shift suggests that the voltage induced by the mutual inductance is greater than the voltage induced by the self-inductance.

Despite this, we can see clear detection in the presence of sample, making the detector functional despite the imbalance in the differential system. This imbalance can be demonstrated

by measuring the same sample on the left pair of inductors, then on the right pair (left and right being defined by the orientation of Fig. 5.3b). This imbalance is shown Fig. 5.5. Theoretically, we should have the same measurement, regardless of the pair on which the sample is placed, but as we can see, this is not the case at all, proving that we have an imbalance problem in the differential system.

Figures 5.6 show the relative ratio measurements. One might think that a singularity appears in the phase shift (Fig. 5.6a) at 30 kHz, but this is merely an artefact arising from the limits of the relative ratio calculation (Eq. (4.12)). Indeed, our reference value, the measurement without sample, oscillates around 0° (Fig. 5.4a) at phase level. As we calculate a ratio, when this reference value approaches 0, a semblance of asymptote appears, giving this singularity around the phase shift around 30 kHz.

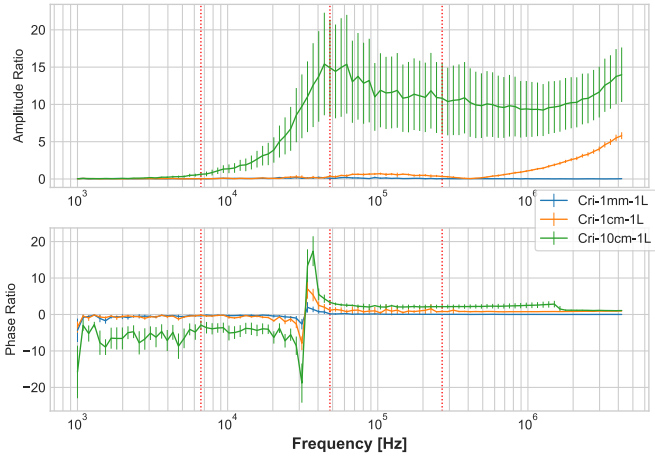


(a) Measurements using the equation $R = \frac{|V_0 - V_{\text{Sample}}|}{V_0}$. A singularity appears around 30 kHz when the $V_0$ value passes through the 0 V line.

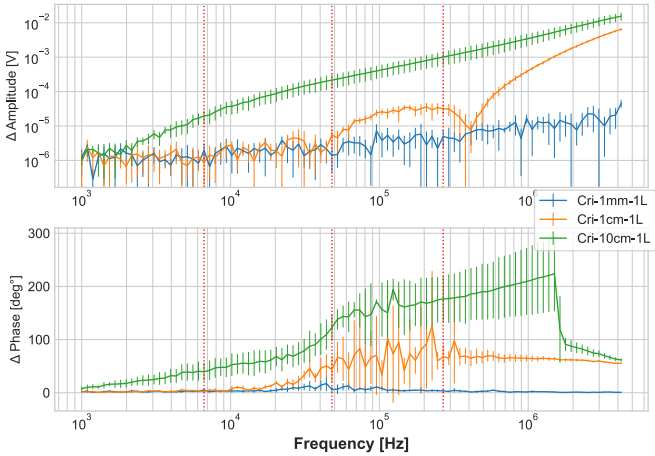


(b) Measurements **relative** using the formula $\Delta V = |V_0 - V_{\text{Sample}}|$. The singularity disappears.

Figure 5.6 – **Relative** measurements of single-layer crystalline ferromagnetic samples with variable surface area.

We therefore use a different form to highlight the variation induced by the presence of the sample, such as :

$$\Delta V = |V_0 - V_{Sample}| \tag{5.2}$$

This formula directly highlights the voltage difference induced by the presence of the sample. In particular, we can see a linear slope of the amplitude variation for the 5 cm² sample, the value of the slope representing the value of the inductance variation induced by the presence of our sample. Knowing the variation in the magnetic field picked up by the sensitive inductor and the intercept area, we can deduce the magnetic permeability of our sample. As we are only briefly exploring differential systems, we won't go into this possibility of knowing the apparent magnetic permeability of a sample, but this subject may be the focus of a later study.

### 5.1.2 Interleaved system

The second system, called « interleaved », is based on the principle that the magnetic sample will be better detected if it overlaps the two inductors as much as possible. Based on this idea, we decided to interleave the two inductors (Fig. 5.7). In this section, we don't go back over the

geometrical parameters and their links with the electrical parameters, but the reasoning is the same as in the previous sections.

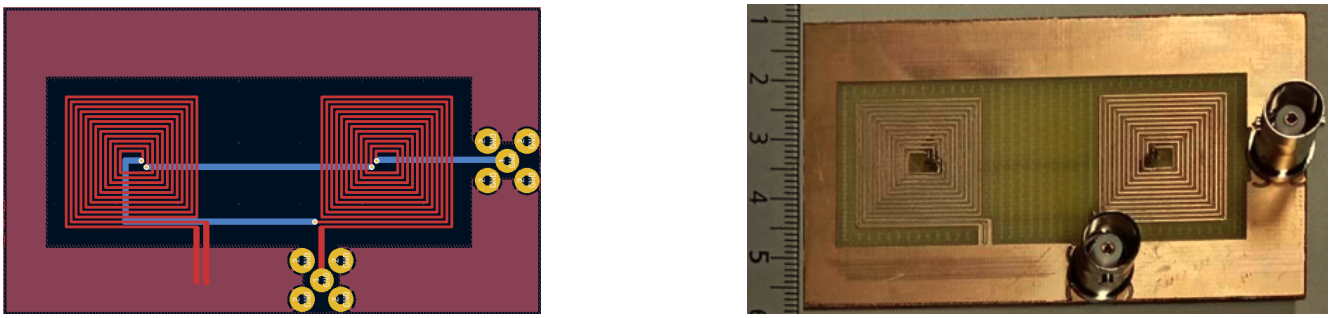

(a) KiCad system diagram

(b) Printed system picture

Figure 5.7 – « Interleaved » differential system

Table 5.2 shows the electrical parameters of interlaced inductors. These were measured using the methods presented in the previous chapters. Mutual inductance was measured using the « classical » method, i.e. by printing an inductor composed of the two inductances in series, then deducting the value of mutual inductance and magnetic coupling from the different inductances measured at the VNA.
Two observations can be made about these measurements: the first is that the parameters of the two primary and secondary inductances are almost equivalent, especially the inductances where we have 0.45 µH for the primary inductance versus 0.39 µH for the secondary inductance. The second observation shows that magnetic coupling, and hence mutual inductance, is greatly improved by this design. Remember that the simple internal/external pair can only have a maximum magnetic coupling $k$ of 0.46 (Section 4.1.2), compared with 0.62 for our interleaved pair.

| Primaire | | | | | Secondary | | | | | | |
|---|---|---|---|---|---|---|---|---|---|---|---|
| $R_p$ [Ω] | $L_p$ [µH] | $C_p$ [pF] | $f_{Q_{max}}$ [MHz] | $f_{res}$ [MHz] | $R_s$ [Ω] | $L_s$ [µH] | $C_s$ [pF] | $f_{Q_{max}}$ [MHz] | $f_{res}$ [MHz] | $M$ [µH] | $k$ |
| 1.83 | 0.45 | 1.34 | 118.2 | 203.95 | 1.9 | 0.39 | 1.22 | 136.48 | 231.86 | 0.26 | 0.62 |

Table 5.2 – Specifications of the inductors making up the « interleaved » differential system

We highlight the measurement of samples using the interleaved differential system (Fig. 5.8). Unfortunately, the voltage measured is 0.7 V RMS or 1 V. This induced voltage is simply impossible and means that we have a short-circuit in our system. This short-circuit certainly stems from the welding of the vias, which are extremely close to each other (Fig. 5.7). Nevertheless, the relative measurement (Fig. 5.8b) still allows us to highlight a variation of $\approx$ 1 mV around 1 MHz.

Unfortunately, the short-circuit prevented any proper analysis of the system, which had to be repaired. Despite the risk of short-circuiting due to the proximity of the vias, this design is one of the most promising. In fact, since the inductances are virtually identical, it makes it easier to characterize and model the system. What is more, the interleaved arrangement significantly improves magnetic coupling and hence mutual inductance. Finally, we have repeatedly found that detection is enhanced if the sample overlaps both inductances, so this design is ideally suited to this optimization.

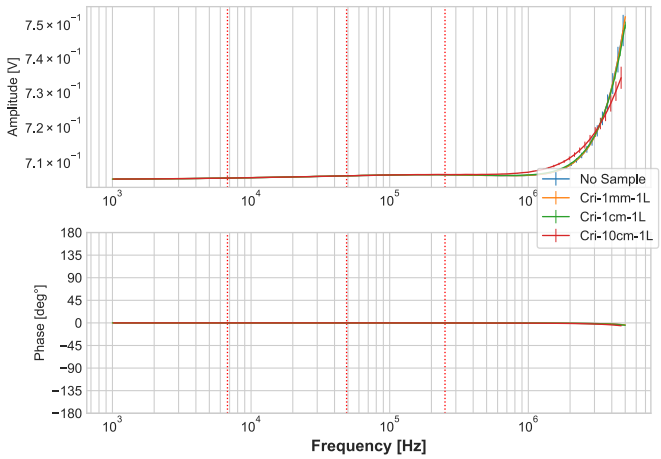


(a) **Absolute** measurements of induced voltage

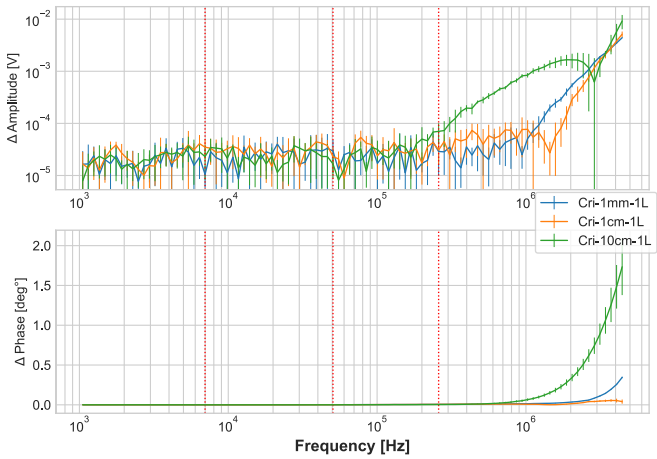


(b) **Relative** measurements based on the absolute difference between induced voltages without samples and induced voltages with samples.

Figure 5.8 – « Interleaved » differential system. Highlighting absolute and relative voltage measurement induced by the presence of ferromagnetic samples

### 5.1.3 Superposed system

Following the same logic as the system described above, we assume that we want the sample between two inductors to cover as large an area as possible. Based on these principles, we decided to design a so-called « superposed » system where the pairs of inductors would be arranged one on top of the other (Figs. 5.9a and 5.9b).

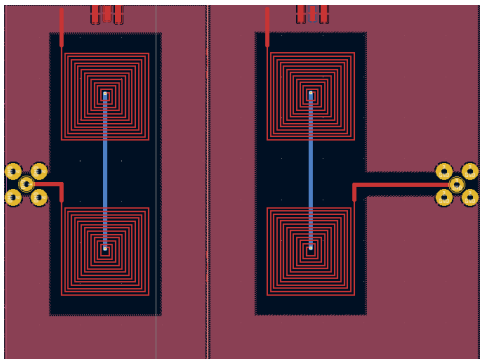

(a) KiCad system diagram

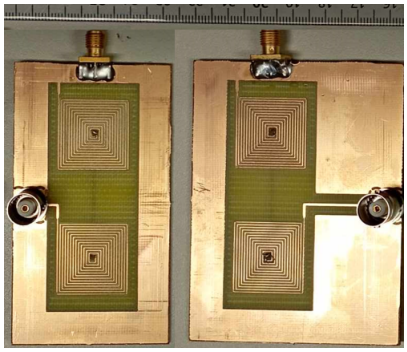

(b) Printed system picture

Figure 5.9 – Differential system **Superposed** divided into two pieces intended to be superposed.

Primary and secondary inductances are exactly the same. We therefore find the same electrical parameters for the primary and secondary inductances (Table 5.3).
Coupling and mutual inductance are lower than for the interlaced system, but equivalent to the conventional system. This low value is due to the large distance of almost 1 cm between the two inductances. This discrepancy is due to a faulty design resulting from the placement of the connectors used to link the masses of the SMA (Fig. 5.10).

Figure 5.11 shows us the low sample-induced variation, of the order of $\approx 10\mu V$, and a

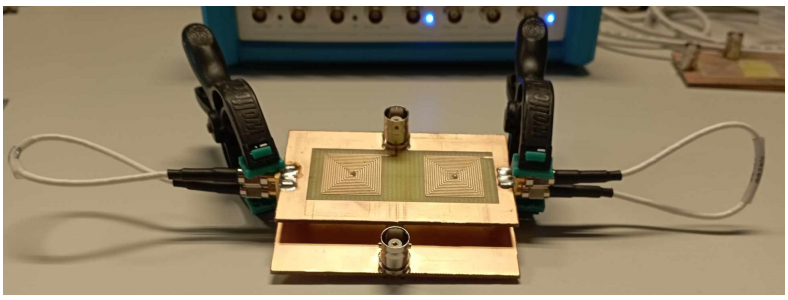

Figure 5.10 – Picture of the superimposed PCB. The clamps are used to keep the system parallel, and the two white cables are used to connect the grounds.

| Primary | | | | | Secondary | | | | | | |
|---|---|---|---|---|---|---|---|---|---|---|---|
| $R_p$ [Ω] | $L_p$ [µH] | $C_p$ [pF] | $f_{Q_{max}}$ [MHz] | $f_{res}$ [MHz] | $R_s$ [Ω] | $L_s$ [µH] | $C_s$ [pF] | $f_{Q_{max}}$ [MHz] | $f_{res}$ [MHz] | $M$ [µH] | $k$ |
| 2.66 | 1.19 | 1.97 | 60.26 | 103.76 | 2.66 | 1.19 | 1.97 | 60.26 | 103.76 | 0.30 | 0.25 |

Table 5.3 – Specifications of the inductors making up the « superposed » differential system

constant high-frequency phase shift of 180°. Although this system may seem interesting, the large gap between the two inductances greatly detracts from the detection quality. What is more, it would be interesting to check measurements at higher frequencies, but again, the system limits us to below 5 MHz. Unfortunately, the low variation indicates that this system, in its current state, is not very effective for detecting samples.

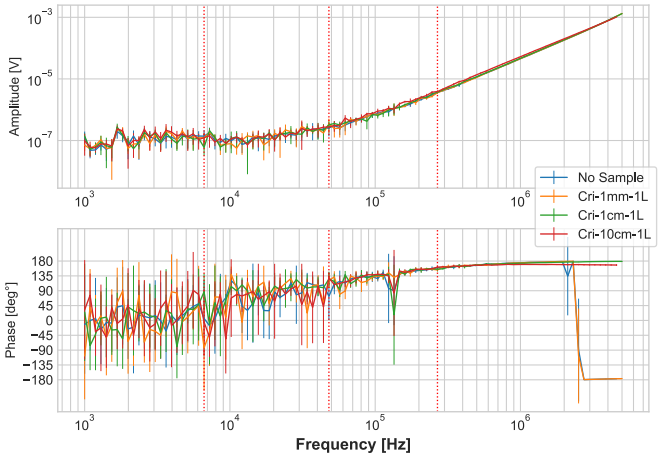


(a) **Absolute** measurements over the frequency spectrum 1 kHz to 5 MHz

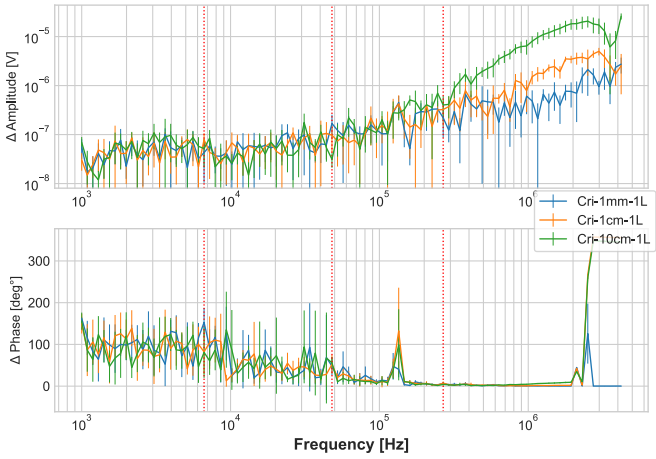


(b) **Relative** measurements based on the absolute difference between induced voltages without samples and induced voltages with samples.

Figure 5.11 – Differential system **superposed**. Highlighting absolute and relative voltage measurement induced by the presence of ferromagnetic samples

Figure 5.12 shows us that the system is once again unbalanced, the 4 curves representing the different possible locations of a sample: between and above the two inductors on the left, and between and above the two inductors on the right.

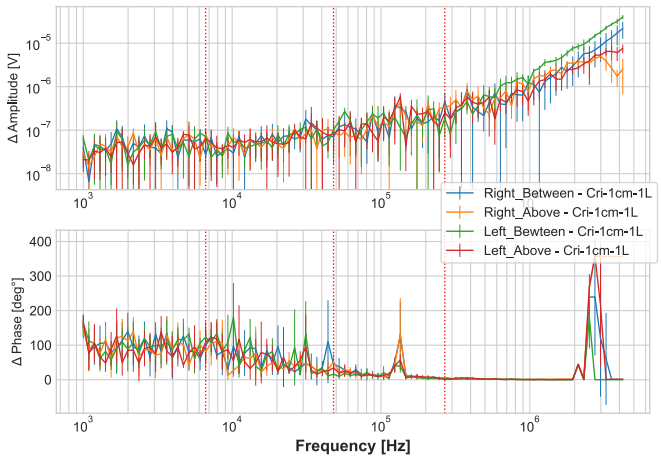


Figure 5.12 – Comparison of **relative** induced voltage with a sample between and above the left pair and between and above the right pair.

## 5.2 Compare systems

Let us compare our different differential systems. Table 5.4 shows the parameters of the different systems. As discussed, we can see that the best magnetic coupling, and therefore mutual inductance, comes from the interleaved design.
Apart from the magnetic coupling coefficient, the parameters follow the variation in geometric specifications, as already discussed in Section 3.1.4. For example, because of its large surface area, and therefore its high inductance value, the superimposed system gives the lowest frequency where the quality factor is maximum, but also gives a lower resonant frequency.

| | Primary | | | | | Secondary | | | | | | |
|---|---|---|---|---|---|---|---|---|---|---|---|---|
| | $R_p$ [Ω] | $L_p$ [µH] | $C_p$ [pF] | $f_{Qmax}$ [MHz] | $f_{res}$ [MHz] | $R_s$ [Ω] | $L_s$ [µH] | $C_s$ [pF] | $f_{Qmax}$ [MHz] | $f_{res}$ [MHz] | $M$ [µH] | $k$ |
| Classic | 1.73 | 0.24 | 1.01 | 191.15 | 349.84 | 2.07 | 0.837 | 1.62 | 79.31 | 136.48 | 0.0375 | 0.21 |
| Interleaved | 1.83 | 0.45 | 1.34 | 118.2 | 203.95 | 1.9 | 0.39 | 1.22 | 136.48 | 231.86 | 0.26 | 0.62 |
| Superposed | 2.66 | 1.19 | 1.97 | 60.26 | 103.76 | 2.66 | 1.19 | 1.97 | 60.26 | 103.76 | 0.30 | 0.25 |

Table 5.4 – Electrical parameters of various differential systems

Figure 5.13a compares the absolute voltages induced by the presence of a ferromagnetic sample of the different detection systems seen in this work. Figure 5.13b shows the relative ratios of sample-induced voltages.

First of all, unfortunately, we can see that our interlaced differential system has a short-circuit between its primary and secondary inductors, and its high voltage and zero phase are good indicators of this.

We also note that the slopes of the classical and superimposed systems are almost equal. Remembering that the slope of our differential systems is theoretically proportional to the variation in inductance induced by the sample, an identical slope indicates the same impact of the sample and therefore **correct** detection of it.

Another possible observation is a comparison of the relative ratios of induced voltages. We see that the classical differential system and the superimposed system give greater sample detection than the simple pair of inductors. This supports the view that a differential system **performs better** than a simple pair of exciting/sensitive inductors.
An outlier in the relative phase shifts (Fig. 5.13b) forces us to use a symmetrical logarithmic scale to display negative values too. We can see that the phase varies little with the presence

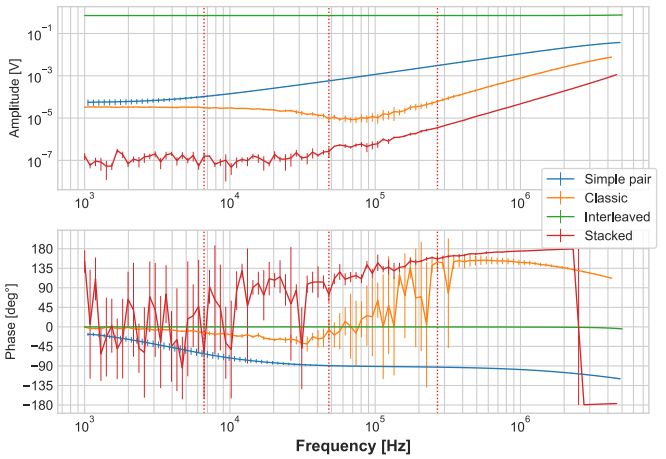


(a) **Absolute** comparison of different induced voltages

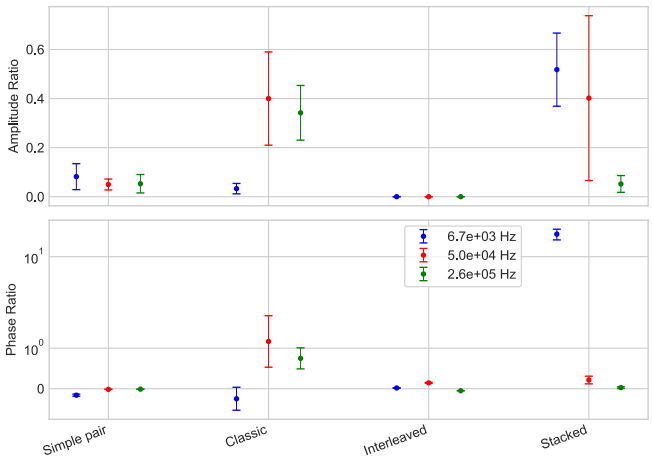


(b) **Relative** measurements of different induced voltages, using a symmetrical logarithmic scale to display negative logarithmic values.

Figure 5.13 – Comparisons of differential systems and a single pair of inductors. A 1 cm² crystalline sample with a single layer was used to highlight the variations.

of a sample. It is therefore more interesting to look at amplitude. Note, however, that this observation only applies to the spectrum under study.

Indeed, one of the major problems in studying our differential systems, apart from the fact that they are unbalanced, is that the spectrum studied is limited by the MFLI. A study over a wider spectrum would surely highlight a greater phase shift induced by the presence of a magnetic sample. In addition to being able to study the phase shift, we also find that induced voltages are lower in our differential systems, giving a lower SNR. A higher frequency would allow a greater induced voltage and therefore a greater SNR.

## 5.3 Conclusion

In this chapter, we have shown that differential systems allow better detection of magnetic samples. Unfortunately, the systems studied have a number of design faults, including short circuits, poorly positioned connectors and, most importantly, an inductance balancing problem. What is more, as the secondary inductors are not perfectly open-circuited, a non-zero voltage is detected in the absence of samples, contrary to the desired effect where the only induced voltage should be due to the presence of a magnetic sample.

A first solution to the problem of unbalance caused by an initial non-zero current is to take the voltage not at the terminals of the two secondary inductors, but at the terminals of each of the secondary inductors and connect them to a differential circuit (Fig. 5.14). If the resistors $R_0$ are identical, this circuit will give an output voltage equal to the difference between the voltages of the secondary inductors.

An intelligent design where the inductors are each on their own PCB would allow each inductor to be replaced individually in the event of failure, thus allowing easier **maintenance** and consequently extending the life of the transducer, improving the **economic** criterion of our device. Take care to connect the secondary inductor grounds for correct reading of the induced

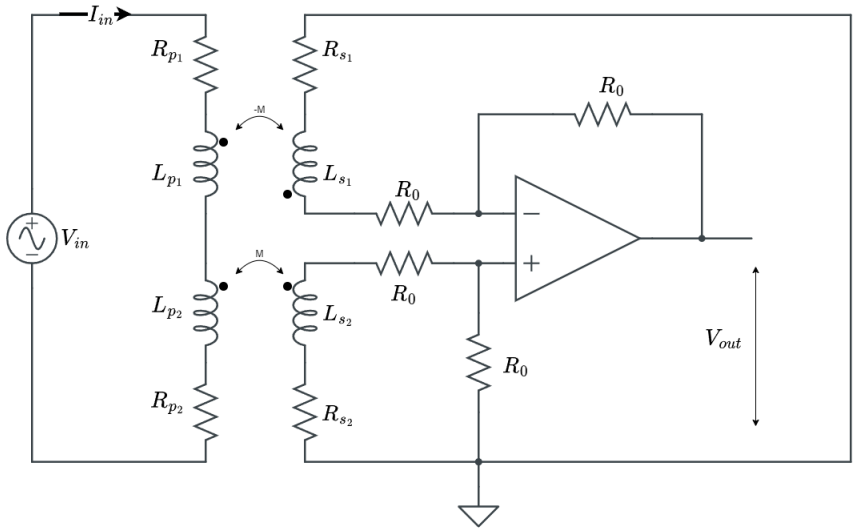


Figure 5.14 – Differential circuit. The two secondary inductors are separated and connected to the terminals of a differential operational amplifier

voltage.

The superposed system remains a good option, but is more complicated to design and implement major drawbacks for a system that we hope will be easy to manufacture. If we use secondary inductors on independent PCB, we can imagine in a future biosensor with notches where these inductors would be inserted and take the sample in « superposed ». Further studies would be interesting to show the relevance of this design, but a posteriori, a system of interleaved inductors remains the most efficient option.

Another possible improvement would be to use the transducer at a **higher frequency**, which would improve the SNR and therefore the detection, and also allow us to work at the frequency where the quality factor is at its maximum, and the inductor is therefore more efficient. Unfortunately, the measurement tools used in this work are not sufficient to explore this lead.

Despite the short circuit and limited frequency range, we remain convinced that an interleaved inductor design is more efficient than the internal/external design. This is because there's better magnetic coupling, and therefore better mutual inductance. What's more, this design makes it easier to apply the sample to both inductors, improving magnetic detection.

# Chapter 6

# Conclusion and perspectives

The main objective of this thesis was to evaluate the potential use and master the understanding of planar inductors for the design of a point-of-care biosensor based on magnetic nanoparticles meeting the « ASSURED » standards defined by WHO: Affordable, Sensitive, Specific, User-friendly, Rapid and robust, Equipment-free and Deliverable to end-users.

First, we defined all the theory needed to handle square planar inductors and then compared it with a concrete example printed on 1.25 $cm^2$ PCB. From the geometric parameters of our print, we were able to estimate the electrical parameters and compare them with real measurements. The resistance of the cables, the non-ideality of the vias and structural imperfections create a difference between theory and reality. However, this difference is negligible and the assembled theory provides a good model for square planar inductors. For example, using the Greenhouse model, we get an estimated inductance of 0.26 µH compared to 0.24 µH measured, a difference of barely 7%.

Based on this theory and measurements, we have developed several methods to determine the mutual inductance between two internal and external square planar inductors. We have shown that only a maximum magnetic coupling coefficient of $k = 0.46$ can be achieved. We have also shown that approximately 2.44 times as many loops are required on the inner inductor as on the outer inductor to maximize the mutual inductance.

We then presented measurements of an induced voltage of 10 µV amplitude, induced by a variable magnetic field of 16 µT produced by Helmholtz coils, and were able to derive a model that is sufficiently reliable to predict the electromagnetic behavior of an inductor, but also of a pair of exciting/sensing inductors. Both the model and the measurements highlight the possibility of measuring the variation of inductance in both amplitude and phase as a function of frequency. In fact, for the amplitude measurement, it is advisable to use the frequency at which the phase shift between the output voltage and the input voltage of the system is -90°. When measuring phase variation, we recommend using frequencies where the phase shift is 45° or 135°.
To study the frequency response of the induced voltage, we used a variety of ferromagnetic samples with different surfaces, thicknesses, and magnetic permeabilities. These samples proved that it is possible to detect and measure magnetic variations through the variation of the voltage induced across our inductors. For example, we were able to detect a nanocrystalline ferromagnetic sample measuring 1 $mm^2$ and 18 µm thick that induced a variation in induced voltage of $\approx 3\%$. We used these measurements to highlight the magnetic saturation between our nanocrystalline and amorphous samples. We then measured different relative concentrations of magnetic nanoparticles. Unfortunately, our simple pair of inductors is not efficient enough to make a quantitative measurement. However, it has been shown that we can make a qualitative mea-

surement of a variation of a few tenths of a percent in the voltage induced by these concentrations.

Finally, the measurements showed that the position of the sample could affect the quality of the measurement and that the best place for it was between the two inductors or on the secondary inductor. In designing differential systems to improve detection, we used this logic of sample placement to design 2 new designs in addition to the first, based on an internal and an external inductor.
The first « interleaved » design uses two planar inductors wrapped around each other. This first design achieves a coupling coefficient greater than $k = 0.6$, i.e. a mutual inductance value of 0.26 µH for primary and secondary inductors of 0.45 and 0.39 µH, respectively.
A second design uses two superposed inductors with a larger surface area than the first two prototypes. Unfortunately, this design is more complicated to implement and does not add any real value. In addition, all of the designs have flaws, including an incipient imbalance in the system. Nevertheless, we have demonstrated that differential systems improve magnetic detection by tens of percent. For example, a single pair of inductors detects a 1 $cm^2$ nanocrystalline ferromagnetic sample, inducing a voltage variation of about ten percent, while a differential system consisting of two pairs of inductors allows a variation of up to 40% of the initial voltage for the same sample without a sample. Based on our observations, we proposed a new design by separating the secondary inductors, thereby improving the induced voltage reading and overall system maintenance.

In conclusion, square planar inductors have great potential for use as efficient and cost-effective magnetic detectors, and are ideally suited for use in point-of-care devices. This work highlights a good first theoretical as well as practical understanding of planar inductors, and demonstrates the possibility of effective use in the form of a differential assembly and interleaved design.

This work is only a preamble to the possible uses of square planar inductors in magnetic detection. Many points remain to be developed. First, we need to prove in practice that the optimized design of the differential circuit is effective. This involves differentiating the voltages across the secondary inductors using an operational amplifier, as well as optimizing the mutual inductance, either by using an interleaved design, or by using the optimum ratio between the number of loops in the primary and secondary inductors.
Most of the models used and developed in this thesis are only sketches and require further investigation, in particular the effect of the parasitic capacitance between the system and the substrate, and the equation describing the behavior of the measured output voltage. In fact, an initial voltage is present in the model, and its origin needs to be further investigated.
We also need to establish the transfer function between the concentration of magnetic nanoparticles and the induced voltage. This requires in-depth knowledge of the behavior of magnetic nanoparticles, including the optimum frequency for exciting nanoparticles and the limits of the detection range.
These various points need to be studied over a wider frequency spectrum, as one of the major limitations of this work remains the limit of a spectrum ranging from 1 kHz to 5 MHz.

# Bibliography


[1] "EAU | HumanSmile." [Online]. Available: https://humansmile.be/eau/

[2] "Eau potable," *www.who.int*, 3 2022. [Online]. Available: https://www.who.int/fr/news-room/fact-sheets/detail/drinking-water#:~:text=La%20contamination%20microbiologique%20de%20l,cons%C3%A9cutifs%20%C3%A0%20des%20maladies%20diarrh%C3%A9iques.

[3] C. Rio, "L'accès à l'eau potable dans le monde," 1 2023. [Online]. Available: https://www.inegalites.fr/L-acces-a-l-eau-potable-dans-le-monde#:~:text=Parmi%20les%206%2C5%20milliards,moins%20douze%20heures%20par%20jour.

[4] C. Kosack, A.-L. Page, and P. Klatser, "A guide to aid the selection of diagnostic tests," *Bulletin of The World Health Organization*, vol. 95, no. 9, pp. 639–645, 6 2017. [Online]. Available: https://doi.org/10.2471/blt.16.187468

[5] M. Hauwaert, "*Towards electro-chemical characterisation of paper-based sensors and usage perspectives*," Master's thesis, Ecole polytechnique de Louvain, Universite catholique de Louvain, 2021, prom. : Raskin, Jean-Pierre. [Online]. Available: http://hdl.handle.net/2078.1/thesis:26771

[6] O. Crahay, "*Towards the design of a paper-based microfluidic sensor for water quality monitoring and comparative life cycle assessment*," Master's thesis, Ecole polytechnique de Louvain, Universite catholique de Louvain, 2020, prom. : Raskin, Jean-Pierre. [Online]. Available: http://hdl.handle.net/2078.1/thesis:25150

[7] G. L. Brun and J.-P. Raskin, "Material and manufacturing process selection for electronics eco-design: case study on paper-based water quality sensors," *Procedia CIRP*, vol. 90, pp. 344–349, 1 2020. [Online]. Available: https://doi.org/10.1016/j.procir.2020.02.041

[8] J. Vandeputte, "*Nanoparticles for paper-based biosensors and environmental impact assessment*," Master's thesis, Ecole polytechnique de Louvain, Universite catholique de Louvain, 2021, prom. : Raskin, Jean-Pierre. [Online]. Available: http://hdl.handle.net/2078.1/thesis:30695

[9] A. Loffet, "*Towards paper-based biosensors : design considerations for lateral flow assay strips using magnetic iron oxide nanoparticles*," Master's thesis, Ecole polytechnique de Louvain, Universite catholique de Louvain, 2023, prom. : Raskin, Jean-Pierre. [Online]. Available: http://hdl.handle.net/2078.1/thesis:40193

[10] J. Mäkiranta and J. Lekkala, "Modeling and Simulation of Magnetic Nanoparticle Sensor," 1 2005. [Online]. Available: https://doi.org/10.1109/iembs.2005.1616653

[11] J. Fraden, *Handbook of Modern Sensors*. Springer Science & Business Media, 9 2010.

[12] K. Kalantar-Zadeh, *Sensors - An Introduction Course*. Springer Science & Business Media, 3 2013.

[13] W. contributors, "Noise (electronics)," *Wikipedia*, 5 2023. [Online]. Available: https://en.wikipedia.org/wiki/Noise_(electronics)

[14] E. Limiti, W. Ciccognani, and S. Colangeli, *Characterization and Modeling of High-Frequency Active Devices Oriented to High-Sensitivity Subsystems Design*, 1 2014. [Online]. Available: https://doi.org/10.1016/b978-0-12-401700-9.00003-3

[15] W. contributors, "Signal-to-noise ratio," *Wikipedia*, 5 2023. [Online]. Available: https://en.wikipedia.org/wiki/Signal-to-noise_ratio

[16] "Signal-to-noise ratio online audio demonstrator." [Online]. Available: https://www.etti.unibw.de/labalive/experiment/snr/

[17] P. Regtien, *Sensors for Mechatronics*, 1 2012. [Online]. Available: https://openlibrary.org/books/OL26144758M/Sensors_For_Mechatronics

[18] Ustaad, "Noise." [Online]. Available: https://www.daenotes.com/electronics/communication-system/noise

[19] "IEC 60050 - International Electrotechnical Vocabulary - Details for IEV number 702-08-39: "white noise"." [Online]. Available: https://www.electropedia.org/iev/iev.nsf/display?openform&ievref=702-08-39

[20] E. Masson, "Les biocapteurs dans le domaine pharmaceutique." [Online]. Available: https://www.em-consulte.com/article/87675/les-biocapteurs-dans-le-domaine-pharmaceutique

[21] *General principles*. Boston, MA: Springer US, 1993, pp. 7–19. [Online]. Available: https://doi.org/10.1007/978-0-585-37623-3_2

[22] "Définitions - Potentiometrie." [Online]. Available: https://www.techniques-ingenieur.fr/base-documentaire/mesures-analyses-th1/methodes-electrochimiques-42388210/potentiometrie-p2115/definitions-p2115v2niv10001.html

[23] W. contributors, "Amperometry," *Wikipedia*, 6 2022. [Online]. Available: https://en.wikipedia.org/wiki/Amperometry

[24] E. Universalis, "VOLTAMeTRIE - Index - Encyclopædia Universalis." [Online]. Available: https://www.universalis.fr/index/voltametrie/#:~:text=La%20voltam%C3%A9trie%20est%20une%20technique,concentration%20d'oxydants...

[25] "Chapter 22 – Introduction to Electroanalytical Chemistry." [Online]. Available: https://www2.chemistry.msu.edu/courses/cem434/Chapter%2022%20%E2%80%93%20Introduction%20to%20Electroanalytical%20Chemistry.pdf

[26] C. Wang, M. Liu, Z. Wang, S. Li, Y. Deng, and N. He, "Point-of-care diagnostics for infectious diseases: From methods to devices," *Nano Today*, vol. 37, p. 101092, 4 2021. [Online]. Available: https://doi.org/10.1016/j.nantod.2021.101092

[27] H. S. Magar, R. Y. A. Hassan, and A. Mulchandani, "Electrochemical Impedance Spectroscopy (EIS): Principles, Construction, and Biosensing Applications," *Sensors*, vol. 21, no. 19, p. 6578, 10 2021. [Online]. Available: https://doi.org/10.3390/s21196578

[28] W. contributors, "Piezoelectricity," *Wikipedia*, 6 2023. [Online]. Available: https://en.wikipedia.org/wiki/Piezoelectricity

[29] Q. AquaPortail, "biocapteur," *AquaPortail*, 8 2020. [Online]. Available: https://www.aquaportail.com/definition-8394-biocapteur.html

[30] J.-c. Cau, "Biodetection optique sans marquage basee sur la diffraction de motifs moleculaires submicroniques," 11 2008.

[31] S.-J. Han and S. X. Wang, "Magnetic Nanotechnology for Biodetection," *JALA*, vol. 15, no. 2, pp. 93–98, 4 2010. [Online]. Available: https://doi.org/10.1016/j.jala.2009.10.008

[32] W. contributors, "Magnetoresistance," *Wikipedia*, 11 2022. [Online]. Available: https://en.wikipedia.org/wiki/Magnetoresistance

[33] ——, "Hall effect," *Wikipedia*, 6 2023. [Online]. Available: https://en.wikipedia.org/wiki/Hall_effect

[34] "Diagomics - Les differentes techniques ELISA." [Online]. Available: https://www.diagomics.com/methode-elisa

[35] L. M. M. S. C. S. Officer, "Biodetection and biosensing: technology and applications," *www.sepmag.eu*, 9 2022. [Online]. Available: https://www.sepmag.eu/blog/biodetection-and-biosensing

[36] D. Quesada-González and A. Merkoçi, "Nanoparticle-based lateral flow biosensors," *Biosensors and Bioelectronics*, vol. 73, pp. 47–63, 2015. [Online]. Available: https://www.sciencedirect.com/science/article/pii/S0956566315301482

[37] C. aux projets Wikimedia, "Immunochromatographie," *fr.wikipedia.org*, 9 2022. [Online]. Available: https://fr.wikipedia.org/wiki/Immunochromatographie

[38] G. Prod'hom, "Diagnostic des maladies infectieuses : place des «point of care tests» (POCT)," 4 2008. [Online]. Available: https://www.revmed.ch/revue-medicale-suisse/2008/revue-medicale-suisse-152/diagnostic-des-maladies-infectieuses-place-des-point-of-care-tests-poct

[39] V. T. Nguyen, S. Song, S. Park, and C. Joo, "Recent advances in high-sensitivity detection methods for paper-based lateral-flow assay," *Biosensors and Bioelectronics*, vol. 152, p. 112015, 3 2020. [Online]. Available: https://doi.org/10.1016/j.bios.2020.112015

[40] AlphaSense, "Datasheet - OX-A431 Oxidising Gas Sensor Ozone + Nitrogen Dioxide 4-Electrode." [Online]. Available: https://www.alphasense.com/wp-content/uploads/2019/09/OX-A431.pdf

[41] ——, "Datasheet - NO2-A43F Nitrogen Dioxide Sensor 4-Electrode." [Online]. Available: https://www.alphasense.com/wp-content/uploads/2019/09/NO2-A43F.pdf

[42] "Pyroelectric detector | Sensor division knowledge." [Online]. Available: https://www.infratec.eu/sensor-division/service-support/glossary/pyroelectric-detector/

[43] P. Jacquet, "Interférométrie avec des lasers femtosecondes infrarouges," Theses, Université Paris Sud - Paris XI, Jan. 2011. [Online]. Available: https://theses.hal.science/tel-00598680

[44] S. Azzouzi, L. Rotariu, A. M. Benito, W. K. Maser, M. B. Ali, and C. Bala, "A novel amperometric biosensor based on gold nanoparticles anchored on reduced graphene oxide for sensitive detection of L-lactate tumor biomarker," *Biosensors and Bioelectronics*, vol. 69, pp. 280–286, 7 2015. [Online]. Available: https://doi.org/10.1016/j.bios.2015.03.012

[45] D. Leslie-Pelecky and R. D. Rieke, "Magnetic Properties of Nanostructured Materials," *Chemistry of Materials*, vol. 8, no. 8, pp. 1770–1783, 1 1996. [Online]. Available: https://doi.org/10.1021/cm960077f

[46] C. Diaz, "*Impedimetry and potentiometry for the design of paper-based biosensors*," Master's thesis, Ecole polytechnique de Louvain, Universite catholique de Louvain, 2022, prom. : Raskin, Jean-Pierre. [Online]. Available: http://hdl.handle.net/2078.1/thesis:37967

[47] A. E. Urusov, A. V. Zherdev, and B. B. Dzantiev, "Towards Lateral Flow Quantitative Assays: Detection Approaches," *Biosensors*, vol. 9, no. 3, p. 89, 7 2019. [Online]. Available: https://doi.org/10.3390/bios9030089

[48] H. Kratz, M. Taupitz, A. A. De Schellenberger, O. Kosch, D. Eberbeck, S. Wagner, L. Trahms, B. Hamm, and J. Schnorr, "Novel magnetic multicore nanoparticles designed for MPI and other biomedical applications: From synthesis to first in vivo studies," *PLOS ONE*, vol. 13, no. 1, p. e0190214, 1 2018. [Online]. Available: https://doi.org/10.1371/journal.pone.0190214

[49] J. B. Haun, T.-J. Yoon, H. Lee, and R. Weissleder, "Magnetic nanoparticle biosensors," *Wiley Interdisciplinary Reviews-nanomedicine and Nanobiotechnology*, vol. 2, no. 3, pp. 291–304, 3 2010. [Online]. Available: https://doi.org/10.1002/wnan.84

[50] W. Wang, Y. Jing, S. He, J.-P. Wang, and J.-P. Zhai, "Surface modification and bioconjugation of feco magnetic nanoparticles with proteins," *Colloids and Surfaces B: Biointerfaces*, vol. 117, pp. 449–456, 2014. [Online]. Available: https://www.sciencedirect.com/science/article/pii/S0927776513007480

[51] R. Qiao, L. Esser, C. Fu, C. Zhang, J. Hu, P. Ramírez-Arcía, Y.-H. Li, J. P. Quinn, M. R. Whittaker, A. K. Whittaker, and T. P. Davis, "Bioconjugation and Fluorescence Labeling of Iron Oxide Nanoparticles Grafted with Bromomaleimide-Terminal Polymers." *Biomacromolecules*, vol. 19, no. 11, pp. 4423–4429, 11 2018. [Online]. Available: https://doi.org/10.1021/acs.biomac.8b01282

[52] Y.-T. Chen, A. G. Kolhatkar, O. Zenasni, S. Xu, and T. R. Lee, "Biosensing Using Magnetic Particle Detection Techniques," *Sensors*, vol. 17, no. 10, p. 2300, 10 2017. [Online]. Available: https://doi.org/10.3390/s17102300

[53] "Diametre hydrodynamique - Encyclopedie FRITSCH – fritsch.de." [Online]. Available: https://www.fritsch-france.fr/granulometrie/base-de-connaissances-fritsch/diametre-hydrodynamique/

[54] C. Sun, J. W. Lee, and M. Zhang, "Magnetic nanoparticles in MR imaging and drug delivery," *Advanced Drug Delivery Reviews*, vol. 60, no. 11, pp. 1252–1265, 8 2008. [Online]. Available: https://doi.org/10.1016/j.addr.2008.03.018

[55] W. contributors, "Magnetic susceptibility," *Wikipedia*, 4 2023. [Online]. Available: https://en.wikipedia.org/wiki/Magnetic_susceptibility

[56] R. A. Freedman and H. H. Young, *University Physics with Modern Physics*, 7 2003. [Online]. Available: https://ci.nii.ac.jp/ncid/BB29466225

[57] Sdv, "Relation between Relative Permeability and Magnetic Susceptibility," *Electrical Volt*, 7 2022. [Online]. Available: https://www.electricalvolt.com/2022/07/relation-between-relative-permeability-and-magnetic-susceptibility/

[58] T. Boisson, "Comment le phénomène de lévitation quantique se matérialise-t-il ?" *Trust My Science*, 12 2018. [Online]. Available: https://trustmyscience.com/comment-phenomene-levitation-quantique-se-materialise/

[59] C. GmbH, "Demagnetisation - notions de base | Cestriom GmbH," 7 2021. [Online]. Available: https://cestriom.com/fr/technologie-2/demagnetisation-notions-de-base/

[60] J. Dormann, "Le phenomene de superparamagnetisme," *Revue de physique appliquee*, vol. 16, no. 6, pp. 275–301, 1 1981. [Online]. Available: https://doi.org/10.1051/rphysap:01981001606027500

[61] W. contributors, "Superparamagnetism," *Wikipedia*, 12 2022. [Online]. Available: https://en.wikipedia.org/wiki/Superparamagnetism

[62] *Sensing Magnetic Nanoparticles*, ser. Magnetic Nanoparticles in Biosensing and Medicine. Cambridge: Cambridge University Press, 2019, pp. 172–227. [Online]. Available: https://www.cambridge.org/core/books/magnetic-nanoparticles-in-biosensing-and-medicine/sensing-magnetic-nanoparticles/D5241AE33B4862F659D6A68B48D483AB

[63] W. contributors, "Giant magnetoresistance," *Wikipedia*, 12 2022. [Online]. Available: https://en.wikipedia.org/wiki/Giant_magnetoresistance

[64] ——, "Magnetoresistance," *Wikipedia*, 11 2022. [Online]. Available: https://en.wikipedia.org/wiki/Magnetoresistance

[65] A. Chalastaras, "Gmr multilayers on a new embossed surface," *IEEE Transactions on Magnetics*, vol. 40, pp. 2257–2259, 2004.

[66] B. Srinivasan, Y. Li, Y. Jing, Y. Xu, X. Yao, C. Xing, and J.-P. Wang, "A Detection System Based on Giant Magnetoresistive Sensors and High-Moment Magnetic Nanoparticles Demonstrates Zeptomole Sensitivity: Potential for Personalized Medicine," *Angewandte Chemie*, vol. 121, no. 15, pp. 2802–2805, 3 2009. [Online]. Available: https://doi.org/10.1002/ange.200806266

[67] W. Qiu, L. S. Chang, Y. Liang, J. Litvinov, J. Guo, Y.-T. Chen, B. Vu, K. Kourentzi, S. Xu, T. R. Lee, Y. Zu, R. C. Willson, and D. Litvinov, "Spin-Valve based magnetoresistive nanoparticle detector for applications in biosensing," *Sensors and Actuators A-physical*, vol. 265, pp. 174–180, 10 2017. [Online]. Available: https://doi.org/10.1016/j.sna.2017.08.018

[68] L. K. Quynh, "Design optimization of an anisotropic magnetoresistance sensor for detection of magnetic nanoparticles," *Journal of Electronic Materials*, vol. 48, pp. 997–1004, 2018.

[69] L. Xuyang, P. Pong, and L. Chunhua, "Dual measurement of current and temperature using a single tunneling magnetoresistive sensor," 10 2018.

[70] H. Lei, K. Wang, X. Ji, and D. Cui, "Contactless measurement of magnetic nanoparticles on lateral flow strips using tunneling magnetoresistance (tmr) sensors in differential configuration," *Sensors*, vol. 16, no. 12, 2016. [Online]. Available: https://www.mdpi.com/1424-8220/16/12/2130

[71] "SQUID National Facility, IIT Delhi." [Online]. Available: http://squid.iitd.ernet.in/Basic_Literature.htm#:~:text=This%20is%20the%20basic%20working,3).

[72] S. Tumanski, "Induction coil sensors—a review," *Measurement Science and Technology*, vol. 18, no. 3, pp. R31–R46, 1 2007. [Online]. Available: https://doi.org/10.1088/0957-0233/18/3/r01

[73] K. Wu, Y. Wang, Y. Feng, L. Yu, and J.-P. Wang, "Colorize magnetic nanoparticles using a search coil based testing method," *Journal of Magnetism and Magnetic Materials*, vol. 380, pp. 251–254, 2015, 10th International Conference on the Scientific and Clinical Applications of Magnetic Carriers 10-14 June, 2014, Dresden, Germany. [Online]. Available: https://www.sciencedirect.com/science/article/pii/S0304885314009342

[74] S. Wei, X. Liao, H. Zhang, J. Pang, and Y. Zhou, "Recent Progress of Fluxgate Magnetic Sensors: Basic Research and Application," *Sensors*, vol. 21, no. 4, p. 1500, 2 2021. [Online]. Available: https://doi.org/10.3390/s21041500

[75] "Magnetometre à vanne de flux : Page pour l'impression." [Online]. Available: http://sesp.esep.pro/fr/pages_mesures-insitu/magnetometre_impression.html

[76] S. Schoinas, A.-M. E. Guamra, F. Moreillon, and P. Passeraub, "Fabrication and Characterization of a Flexible Fluxgate Sensor with Pad-Printed Solenoid Coils," *Sensors*, vol. 20, no. 8, p. 2275, 4 2020. [Online]. Available: https://doi.org/10.3390/s20082275

[77] Danisense, "The flux gate working principle and theory - danisense," *Danisense*, 12 2022.

[78] D. Ruehmer, E. Heim, A. S. Hirsch, R. Piel, T. Wawrzik, F. Ludwig, and M. K. Schilling, "A6.3 - Magnetic relaxation imaging with a fluxgate sensor scanner," 1 2009. [Online]. Available: https://doi.org/10.5162/sensor09/v2/a6.3

[79] J. Dieckhoff, M. Schilling, and F. Ludwig, "Fluxgate based detection of magnetic nanoparticle dynamics in a rotating magnetic field," *Applied Physics Letters*, vol. 99, no. 11, p. 112501, 9 2011. [Online]. Available: https://doi.org/10.1063/1.3639276

[80] P. Besse, G. Boero, M. Demierre, V. Pott, and R. Popovic, "Detection of a single magnetic microbead using a miniaturized silicon hall sensor," *Appl. Phys. Lett*, vol. 80, 01 2002.

[81] P. Liu, K. Skucha, M. Megens, and B. Boser, "A cmos hall-effect sensor for the characterization and detection of magnetic nanoparticles for biomedical applications," *Magnetics, IEEE Transactions on*, vol. 47, pp. 3449 – 3451, 11 2011.

[82] R. Popovic, Z. Randjelovic, and D. Manic, "Integrated hall-effect magnetic sensors," *Sensors and Actuators A: Physical*, vol. 91, no. 1, pp. 46–50, 2001, third European Conference on Magnetic Sensors & Actuators. [Online]. Available: https://www.sciencedirect.com/science/article/pii/S0924424701004782

[83] C. Min, H. Shao, M. Liong, T.-J. Yoon, R. Weissleder, and H. Lee, "Mechanism of Magnetic Relaxation Switching Sensing," *ACS Nano*, vol. 6, no. 8, pp. 6821–6828, 7 2012. [Online]. Available: https://doi.org/10.1021/nn301615b

[84] G. Nodet and M. Blackledge, "La relaxation en resonance magnetique nucleaire." [Online]. Available: http://thcgerm.free.fr/IMG/pdf/Blackledge_1.pdf

[85] S. Achtsnicht, A. M. Pourshahidi, A. Offenhäusser, and H.-J. Krause, "Multiplex detection of different magnetic beads using frequency scanning in magnetic frequency mixing technique," *Sensors*, vol. 19, 06 2019.

[86] M. Bauch, K. Toma, M. Toma, Q. Zhang, and J. Dostalek, "Plasmon-Enhanced Fluorescence Biosensors: a Review," *Plasmonics*, vol. 9, no. 4, pp. 781–799, 12 2013. [Online]. Available: https://doi.org/10.1007/s11468-013-9660-5

[87] K.-H. Huynh, E. Hahm, M. Y. Noh, J.-H. Lee, D.-E. Kim, S. Y. Lee, J. Kim, W.-Y. Rho, H. Chang, A. Baek, D.-W. Kim, D. H. Jeong, S. W. Park, and S. H. Lee, "Recent Advances in Surface-Enhanced Raman Scattering Magnetic Plasmonic Particles for Bioapplications," *Nanomaterials*, vol. 11, no. 5, p. 1215, 5 2021. [Online]. Available: https://doi.org/10.3390/nano11051215

[88] Y. Haddad, S. Dostalova, J. Kudr, O. Zitka, Z. Heger, and V. Adam, "DNA-magnetic Particle Binding Analysis by Dynamic and Electrophoretic Light Scattering," *Journal of Visualized Experiments*, no. 129, 11 2017. [Online]. Available: https://doi.org/10.3791/56815

[89] X. Bai, K. Wen, D. Peng, S. Liu, and L. Luo, "Atomic magnetometers and their application in industry," *Frontiers in Physics*, vol. 11, 6 2023. [Online]. Available: https://doi.org/10.3389/fphy.2023.1212368

[90] R.-M. Friedrich, S. Zabel, A. Galka, N. Lukat, J.-M. Wagner, C. Kirchhof, E. Quandt, J. McCord, C. Selhuber-Unkel, M. Siniatchkin, and F. Faupel, "Magnetic particle mapping using magnetoelectric sensors as an imaging modality," *Scientific Reports*, vol. 9, no. 1, p. 2086, Feb 2019. [Online]. Available: https://doi.org/10.1038/s41598-018-38451-0

[91] W. O. Nyang'au, A. Setiono, M. Bertke, H. Bosse, and E. Peiner, "Cantilever-Droplet-Based Sensing of Magnetic Particle Concentrations in Liquids," *Sensors*, vol. 19, no. 21, p. 4758, 11 2019. [Online]. Available: https://doi.org/10.3390/s19214758

[92] T. Bertók, A. Bertokova, S. Hroncekova, E. Chocholova, N. Kosutova, L. Lorencova, P. Kasák, and J. Tkac, "Novel prostate cancer biomarkers: Aetiology, clinical performance and sensing applications," *Chemosensors*, vol. 9, p. 205, 08 2021.

[93] "Chapitre IV : Inductance propre, inductance mutuelle. energie electromagnetique." [Online]. Available: http://sertella.free.fr/cours_psi_physique/electromagnetisme/electromag%20chapitre%2004.pdf

[94] W. contributors, "Inductance," *Wikipedia*, 5 2023. [Online]. Available: https://en.wikipedia.org/wiki/Inductance#:~:text=The%20inductance%20is%20proportional%20to,the%20hole%20in%20the%20center.

[95] "Inductors and inductor coils: basic principles, types, inductance, and applications." [Online]. Available: https://www.iqsdirectory.com/articles/electric-coil/inductors-and-inductor-coils.html

[96] F. Tounsi, D. Flandre, L. Rufer, and L. A. Francis, "Performances evaluation of on-chip large-size-tapped transformer for mems applications," *IEEE Transactions on Instrumentation and Measurement*, vol. 69, pp. 7051 – 7060, 09 2020.

[97] E. Aydin, M. T. Aydemir, A. Aksoz, M. E. Baghdadi, and O. Hegazy, "Inductive Power Transfer for Electric Vehicle charging Applications: A Comprehensive review," *Energies*, vol. 15, no. 14, p. 4962, 7 2022. [Online]. Available: https://doi.org/10.3390/en15144962

[98] J. L. Marques-Fernández, M. Salvador, J. Martínez-García, P. F. Miaja, A. García-Arribas, and M. Rivas, "New perspective on Planar inductive sensors: Radio-frequency refractometry for highly sensitive quantification of magnetic nanoparticles," *Sensors*, vol. 23, no. 5, p. 2372, 2 2023. [Online]. Available: https://doi.org/10.3390/s23052372

[99] G. Haobijam and R. P. Palathinkal, *Design and analysis of spiral inductors*, 1 2014. [Online]. Available: https://doi.org/10.1007/978-81-322-1515-8

[100] P. Pereira, M. H. Fino, F. Coito, and M. Ventim-Neves, "Rf integrated inductor modeling and its application to optimization-based design," *Analog Integrated Circuits and Signal Processing - ANALOG INTEGR CIRCUIT SIGNAL*, vol. 73, pp. 1–9, 10 2011.

[101] A. Islam, "Design and optimization of printed circuit board inductors for wireless power transfer system," *Circuits and Systems*, vol. 04, pp. 237–244, 01 2013.

[102] Y. Yang, M. El Baghdadi, Y. Lan, Y. Benomar, J. Van Mierlo, and O. Hegazy, "Design methodology, modeling, and comparative study of wireless power transfer systems for electric vehicles," *Energies*, vol. 11, no. 7, 2018. [Online]. Available: https://www.mdpi.com/1996-1073/11/7/1716

[103] M. Esa and A. V. Kordesh, "RF Spiral Planar Inductor Designs - Preliminary results," *ResearchGate*, 1 2003. [Online]. Available: https://www.researchgate.net/publication/253776033_RF_Spiral_Planar_Inductor_Designs_-_Preliminary_Results

[104] S. V. Mohan, M. Del Mar Hershenson, S. Boyd, and T. R. Lee, "Simple accurate expressions for planar spiral inductances," *IEEE Journal of Solid-state Circuits*, vol. 34, no. 10, pp. 1419–1424, 1 1999. [Online]. Available: https://doi.org/10.1109/4.792620

[105] H. M. Greenhouse, "Design of Planar Rectangular Microelectronic Inductors," *IEEE Transactions on Parts, Hybrids, and Packaging*, vol. 10, no. 2, pp. 101–109, 6 1974. [Online]. Available: https://doi.org/10.1109/tphp.1974.1134841

[106] E. B. Rosa, "Calculation of the self-inductance of single-layer coils," *Bulletin of the Bureau of Standards*, vol. 2, no. 2, p. 161, 8 1906. [Online]. Available: https://doi.org/10.6028/bulletin.034

[107] "COIL32 - Self-capacitance of single-layer inductor," 2 2015. [Online]. Available: https://coil32.net/theory/self-capacitance.html

[108] G. Grandi, M. Kazimierczuk, A. Massarini, and U. Reggiani, "Stray capacitance of single-layer solenoid air-core inductors," *Industry Applications, IEEE Transactions on*, vol. 35, pp. 1162 – 1168, 10 1999.

[109] T. Watanabe and H. Ueda, "Several Problems about Sensitivity and Frequency Response of an Induction Magnetometer," *Science reports of the Tohoku University. Ser. 5, Geophysics*, vol. 22, 1 1975. [Online]. Available: http://hdl.handle.net/10097/44722

[110] S. Tumanski, "Induction coil sensors—a review," *Measurement Science and Technology*, vol. 18, no. 3, p. R31, jan 2007. [Online]. Available: https://dx.doi.org/10.1088/0957-0233/18/3/R01

[111] A. B. Islam, S. Islam, and F. S. Tulip, "Design and optimization of printed circuit board inductors for wireless power transfer system," *Circuits and Systems*, vol. 04, no. 02, pp. 237–244, 1 2013. [Online]. Available: https://doi.org/10.4236/cs.2013.42032

[112] G. Stojanovi, L. Zivanov, and M. Damnjanovic, "Optimal design of circular inductors," *Facta universitatis - series: Electronics and Energetics*, vol. 18, 01 2005.

[113] P. Pirouznia and B. Azizollah Ganji, "Analytical optimization of high performance and high quality factor mems spiral inductor," *Progress In Electromagnetics Research M*, vol. 34, pp. 171–179, 01 2014.

[114] J. PARRY, "Helmholtz coils and coil design," *Developments in Solid Earth Geophysics*, vol. 3, 12 2013.

[115] W. contributors, "Helmholtz Coil," *Wikipedia*, 2 2023. [Online]. Available: https://en.wikipedia.org/wiki/Helmholtz_coil

[116] Yumpu.com, "Helmholtz-Spulen U8481500 - 3B Scientific." [Online]. Available: https://www.yumpu.com/es/document/view/35373623/helmholtz-spulen-u8481500-3b-scientific

[117] "THM1176 handheld three-axis hall magnetometer by MetroLab," 6 2023. [Online]. Available: https://www.metrolab.com/fr/products/thm1176-three-axis-hall-magnetometer/

[118] "About Lock-In Amplifiers." [Online]. Available: https://www.thinksrs.com/support/app.html

[119] Lodovico, "Lock-in amplifier," *PhysicsOpenLab*, 2 2020. [Online]. Available: https://physicsopenlab.org/2019/08/20/lock-in-amplifier/

[120] J. Drozd and W. T. Joines, "Determining Q using S parameter data," *IEEE Transactions on Microwave Theory and Techniques*, 1 1996. [Online]. Available: https://doi.org/10.1109/22.543972

[121] W. contributors, "Impedance parameters," *Wikipedia*, 4 2021. [Online]. Available: https://en.wikipedia.org/wiki/Impedance_parameters

[122] "Two-Port impedance model and Z-Parameters." [Online]. Available: https://resources.system-analysis.cadence.com/blog/msa2020-two-port-impedance-model-and-z-parameters

[123] Multi-Cb, "FR4 material: Glossary," 6 2019. [Online]. Available: https://www.multi-circuit-boards.eu/en/glossary/FR4_Material.html#:~:text=FR4%20is%20a%20class%20of,very%20suitable%20for%20standard%20applications.

[124] Connector and C. A. Supplier, "Connector Supplier - Latest news about electrical electronic connectors," 7 2023. [Online]. Available: https://connectorsupplier.com/

[125] S. Sis and E. Orta, "A cross-shape coil structure for use in wireless power applications," *Energies*, vol. 11, p. 1094, 04 2018.

[126] P. Ripka, "Magnetic sensors and magnetometers," *Measurement Science and Technology*, vol. 13, no. 4, p. 645, 3 2002. [Online]. Available: https://doi.org/10.1088/0957-0233/13/4/707

[127] F. Tounsi, M. H. Said, M. Hauwaert, S. Kaziz, L. Francis, J.-P. Raskin, and D. Flandre, "Variation range of different inductor topologies with shields for RF and inductive sensing applications," *Sensors*, vol. 22, no. 9, p. 3514, 5 2022. [Online]. Available: https://doi.org/10.3390/s22093514

# Appendix A

# Python code

## A.1 VNA analysis

```
from matplotlib import pyplot as plt
import numpy as np
import matplotlib as mpl


# ================================== Matplotlib parameters ==========================================
plt.style.use('seaborn-whitegrid')
mpl.rcParams['lines.linewidth'] = 1
mpl.rcParams['lines.linestyle'] = '-'
plt.rcParams['figure.figsize'] = [7, 10]



polar2z = lambda r,theta: r * np.exp( 1j * theta )
z2polar = lambda z: ( np.abs(z), np.angle(z) )
dB2Amp = lambda dB: 10**(dB/20)




mu0 = 4*np.pi * 10**-7
mu_r = 1
mu = mu0*mu_r
c = 3*10**8
eps0 = 1/(mu0*c**2)

copper_resistivity = 1.7e-8


   = lambda f : 2*np.pi*f
Q = lambda ind, f : -2*np.pi*f*(ind.C*ind.R**2 - ind.L + ind.C*ind.L**2*(2*np.pi*f)**2)/ind.R


class Inductance:

    def __init__(self, N, d_in, s, w, t):
        self.N = N
        self.d_in = d_in
        self.s = s
        self.w = w
        self.d_out = d_in + 2*(N * w + (N-1)*s)
        self.t = t #[m] tickness

        self.rho = (self.d_out-d_in)/(self.d_out+d_in)
        self.d_avg = (self.d_out+d_in)/2

        self.S_eq = self.d_avg**2*N

        self.l = 4*N*self.d_out-4*N*w-(2*N+1)**2 * (s+w) #length [m]
        # self.l = 4*N*(self.d_out-(w+s)*(N-1)) #length [m]

        c1 = 1.27
```

```
        c2 = 2.07
        c3 = 0.18
        c4 = 0.13
        self.L =  mu*N**2*self.d_avg*c1/2 * (np.log(c2/self.rho)+c3*self.rho+c4*self.rho**2)  #Greenhouse model
        self.C = 2*self.l*eps0/np.pi * np.log((self.w+self.s/2)/(self.s/2))

        self.R = copper_resistivity*self.l/(self.w*self.t)
        self.f_res = 1/(2*np.pi*np.sqrt(self.L * self.C))

    def setC(self, f_res):
        self.f_res = f_res
        return 1/((2*np.pi*f_res)**2*self.L)

    def setR(self, f):
        delta_sf = lambda f : np.sqrt(copper_resistivity/(np.pi*f*mu))
        return copper_resistivity*self.l/(self.w*delta_sf(f)*(1-np.exp(-self.t/delta_sf(f))))

    def Z(self, f):
        return (self.R + 1j*  (f)*self.L)/(1+1j*  (f)*self.C*self.R-(1j*  (f))**2*self.L*self.C)
    def fullZ(self, f):
        return (self.setR(f) + 1j*  (f)*self.L) / (1+1j*  (f)*self.C*self.setR(f)-(1j*  (f))**2*self.L*self.C)
    def Q(self, f):
        return -1*  (f)*(self.C*self.R**2 - self.L + self.C*self.L**2*  (f)**2)/self.R
# ========================================== Read function ==========================================

def readS2P(dir_path, filename):
    l_frequency, l_S11, l_S21, l_S12, l_S22 = [],[],[],[],[]

    file = open(dir_path + filename, "r")
    for line in file:
        if line[0] == '!':
            continue
        elif line[0] == '#':
            freq_unit = line.strip().split(" ")[1].upper()
            if freq_unit == 'GHZ':
                freq_unit = 1e9
            elif freq_unit == 'MHZ':
                freq_unit = 1e6
            elif freq_unit == 'MHZ':
                freq_unit = 1e3
            elif freq_unit == 'HZ':
                freq_unit = 1
            else:
                raise ValueError("Wrong unit in the file")

            dB_or_RI = line.strip().split(" ")[3].upper()
        else:
            if dB_or_RI == "RI":
                l_split = line.split()
                l_frequency.append(float(l_split[0])*freq_unit)
                l_S11.append(float(l_split[1]) + 1j*float(l_split[2]))
                l_S21.append(float(l_split[3]) + 1j*float(l_split[4]))
                l_S12.append(float(l_split[5]) + 1j*float(l_split[6]))
                l_S22.append(float(l_split[7]) + 1j*float(l_split[8]))

            elif dB_or_RI == "DB":
                l_split = line.split()
                l_frequency.append(float(l_split[0])*freq_unit)
                l_S11.append(polar2z(dB2Amp(float(l_split[1])), float(l_split[2])))
                l_S21.append(polar2z(dB2Amp(float(l_split[3])), float(l_split[4])))
                l_S12.append(polar2z(dB2Amp(float(l_split[5])), float(l_split[6])))
                l_S22.append(polar2z(dB2Amp(float(l_split[7])), float(l_split[8])))


    file.close()
    return np.array(l_frequency), np.array(l_S11), np.array(l_S21), np.array(l_S12), np.array(l_S22)

# ================================== S2P ==========================================

L_name ="L1_INTERNE"

dir_path = r"C:\Users\Thall\OneDrive - UCL\Master\M moire\Suivi_TFE_DorianVN_partage\Labos\20230715-lab8
```

```
    \04_08" + "\\"
# dir_path = r"E:" + "\\"

filename = L_name+".s2p"

frequency, S11, S21, S12, S22 = readS2P(dir_path, filename)

Z0 = 50
dS = (1-S11)*(1-S22)-S12*S21

Z11 = Z0 * ((1 + S11) * (1 - S22) + S12 * S21) / ((1 - S11) * (1 - S22) - S12 * S21)
Z12 = Z0 * 2 * S12 / ((1 - S11) * (1 - S22) - S12 * S21)
Z21 = Z0 * 2 * S21 / ((1 - S11) * (1 - S22) - S12 * S21)
Z22 = Z0 * ((1 - S11) * (1 + S22) + S12 * S21) / ((1 - S11) * (1 - S22) - S12 * S21)

Y0 = 1/Z0
dS = (1 - S11) * (1 - S22) - S12 * S21

Y11 = Y0 * ((1 - S11) * (1 - S22) + S12 * S21) / dS
Y12 = -Y0 * 2 * S12 / dS
Y21 = -Y0 * 2 * S21 / dS
Y22 = Y0 * ((1 + S11) * (1 + S22) - S12 * S21) / dS


Zin = Z0*(1+S11)/(1-S11)
Zout = Z0*(1+S22)/(1-S22)


fres_in = frequency[np.argmax(Zin)]
fres_out = frequency[np.argmax(Zout)]


q_factors = np.imag(S12)/np.real(S12)


# ======================================== Inductor
    ================================================================


L1_interne = Inductance(6, 2.4e-3, 0.4e-3, 0.4e-3, 17e-6)
L1_externe = Inductance(6, 13.2e-3, 0.4e-3, 0.4e-3, 17e-6)

L_data = L1_interne

# ======================================== Function
    ================================================================

def moving_average_filter(data, window_size):
    """
    Apply a moving average filter to smooth the input data.

    Parameters:
        data (numpy array): The input data to be filtered.
        window_size (int): The size of the moving average window.

    Returns:
        numpy array: The filtered data.
    """
    window = np.ones(window_size) / window_size
    filtered_data = np.convolve(data, window, mode='same')
    return filtered_data


# Function to calculate the magnitude of the impedance
def Z_RL_parallel_C(f, R, L, C):
    omega = 2 * np.pi * f
    Z_total = (R + 1j*omega*L)/(1+1j*omega*C*R-omega**2*L*C)
    return Z_total




# ======================================== Main
    ================================================================

# Calculate the impedance
```

```
VNA = Z11+Z22-(Z12+Z21)


# Create a figure and axes
fig, ax = plt.subplots(4, 1)

# ========================= First graphe : Data Amplitude ========================
ax[0].plot(frequency, np.abs(VNA), 'g', label='Magnitude VNA')

ax[0].set_xscale("log")
ax[0].set_yscale("log")
ax[0].set_ylabel("Z Amplitude [  ]")

# ========================= Second graphe : Data Phase ===========================
ax[1].plot(frequency, np.angle(VNA)*180/np.pi, 'g', label='Phase VNA')

ax[1].legend(bbox_to_anchor=(1, 0.75), loc='center left')

ax[1].set_xscale("log")
ax[1].set_ylabel("Z Phase [  ]")

# ========================= Third graphe : R =====================

data = np.real(VNA)

threshold = 1e-2
stable_region = np.abs(np.diff(data)) <= threshold
stable_frequencies = frequency[:-1][stable_region]
stable_resistance = data[:-1][stable_region]

fitting_R = np.mean(stable_resistance) #<======== FITTING

ax[2].plot(stable_frequencies, stable_resistance, 'b.', label=f'Treshold :    <= {threshold}')
ax[2].plot([stable_frequencies[0], stable_frequencies[-1]], np.ones(2)*fitting_R, 'r', label=f'Mean : {
    fitting_R:.2e}   ')
ax[2].plot([stable_frequencies[0], stable_frequencies[-1]], np.ones(2)*L_data.R, 'b:', label=f'Analytical
    : {L_data.R:.2e}   ')
ax[2].plot(frequency, np.abs(data), 'g')

ax[2].legend(bbox_to_anchor=(1, 0.75), loc='center left')

ax[2].set_ylabel("Fiting R [  ]")
ax[2].set_xscale("log")
ax[2].set_yscale("log")

# ========================= Fourth graphe : L =====================

data = np.imag(VNA)/(2*np.pi*frequency)

threshold = 0.3e-8
stable_region = np.abs(np.diff(data)) <= threshold
stable_frequencies = frequency[:-1][stable_region]
stable_inductances = data[:-1][stable_region]

fitting_L = np.mean(stable_inductances) #<======== FITTING

ax[3].plot(stable_frequencies, stable_inductances, 'b.', label=f'Treshold :    <= {threshold}')
ax[3].plot([stable_frequencies[0], stable_frequencies[-1]], np.ones(2)*fitting_L, 'r', label=f'Mean : {
    fitting_L:.2e} H')
ax[3].plot([stable_frequencies[0], stable_frequencies[-1]], np.ones(2)*L_data.L, 'b:', label=f'Analytical
    : {L_data.L:.2e} H')
ax[3].plot(frequency, np.abs(data), 'g')

ax[3].legend(bbox_to_anchor=(1, 0.75), loc='center left')

ax[3].set_ylabel("Fitting L [H]")
ax[3].set_xscale("log")
ax[3].set_yscale("log")

# ========================= Fitting vs Analytical ========================
fres = frequency[np.argmax(np.abs(VNA))]
fitting_C = 1/((2*np.pi*fres)**2 * fitting_L) #<======== FITTING

# === First graphe  ===
data = Z_RL_parallel_C(frequency, fitting_R, fitting_L, fitting_C)
ax[0].plot(frequency, np.abs(data), 'r:', label='Fitting data')
```

```
ax[0].plot(frequency[np.argmax(np.abs(VNA))],
           np.max(np.abs(VNA)), 'g^',
           label="$f_{res}$"+f': {frequency[np.argmax(np.abs(data))]/1e6:3g} MHz')
fL = fitting_R/(2*np.pi*fitting_L)
ax[0].plot(fL,
           Z_RL_parallel_C(fL, fitting_R, fitting_L, fitting_C), 'gv',
           label="$f_{L}$"+f': {fL/1e3:2g} kHz')


data = Z_RL_parallel_C(frequency, L_data.R, L_data.L, L_data.C)
ax[0].plot(frequency, np.abs(data), 'b:', label='Analycal data')
ax[0].plot(frequency[np.argmax(np.abs(data))],
           np.max(np.abs(data)), 'b^',
           label="$f_{res}$"+f': {frequency[np.argmax(np.abs(data))]/1e6:3g} MHz')
fL = L_data.R/(2*np.pi*L_data.L)
ax[0].plot(fL,
           Z_RL_parallel_C(fL, L_data.R, L_data.L, L_data.C), 'bv',
           label="$f_{L}$"+f': {fL/1e3:2g} kHz')


ax[0].legend(bbox_to_anchor=(1, 0.75), loc='center left')

# === Second graphe  ===
data = Z_RL_parallel_C(frequency, fitting_R, fitting_L, fitting_C)
ax[1].plot(frequency, np.angle(data)*180/np.pi, 'r:', label='Fitting data')

data = Z_RL_parallel_C(frequency, L_data.R, L_data.L, L_data.C)
ax[1].plot(frequency, np.angle(data)*180/np.pi, 'b:', label='Analycal data')


ax[1].legend(bbox_to_anchor=(1, 0.75), loc='center left')

plt.xlabel("Frequency [Hz]")

plt.tight_layout()
plt.savefig(r"C:\Users\Thall\OneDrive - UCL\Master\M moire\Suivi_TFE_DorianVN_partage\Labos\figures\
    VNA_ANALYSE_CHANGE_NAME.svg")
# Show the plot
plt.show()
```

## A.2 Mutual inductance analysis

```
from matplotlib import pyplot as plt
import numpy as np
import matplotlib as mpl

from matplotlib.ticker import AutoMinorLocator, MultipleLocator

# ================================== Matplotlib parameters
    ================================================
plt.style.use('seaborn-whitegrid')
mpl.rcParams['lines.linewidth'] = 1
mpl.rcParams['lines.linestyle'] = '-'
plt.rcParams['figure.figsize'] = [7, 5]


color = ["blue", "green","red", "brown", "pink", "purple", "orange", "gray", "olive", "cyan"]

polar2z = lambda r,theta: r * np.exp( 1j * theta )
z2polar = lambda z: ( np.abs(z), np.angle(z) )
dB2Amp = lambda dB: 10**(dB/20)


mu0 = 4*np.pi * 10**-7
mu_r = 1
mu = mu0*mu_r
c = 3*10**8
eps0 = 1/(mu0*c**2)

copper_resistivity = 1.7e-8


   = lambda f : 2*np.pi*f
Q = lambda ind, f : -2*np.pi*f*(ind.C*ind.R**2 - ind.L + ind.C*ind.L**2*(2*np.pi*f)**2)/ind.R

```

```
33
34 class Inductance:
35
36     def __init__(self, N, d_in, s, w, t):
37         self.N = N
38         self.d_in = d_in
39         self.s = s
40         self.w = w
41         self.d_out = d_in + 2*(N * w + (N-1)*s)
42         self.t = t #[m] tickness
43
44         self.rho = (self.d_out-d_in)/(self.d_out+d_in)
45         self.d_avg = (self.d_out+d_in)/2
46
47         self.S_eq = self.d_avg**2*N
48
49         self.l = 4*N*self.d_out-4*N*w-(2*N+1)**2 * (s+w) #length [m]
50         # self.l = 4*N*(self.d_out-(w+s)*(N-1)) #length [m]
51
52         c1 = 1.27
53         c2 = 2.07
54         c3 = 0.18
55         c4 = 0.13
56         self.L =  mu*N**2*self.d_avg*c1/2 * (np.log(c2/self.rho)+c3*self.rho+c4*self.rho**2)  #Greenhouse
    model
57         self.C = 2*self.l*eps0/np.pi * np.log((self.w+self.s/2)/(self.s/2))
58
59         self.R = copper_resistivity*self.l/(self.w*self.t)
60
61     def fullC(self, f_res):
62         return 1/((2*np.pi*f_res)**2*self.L)
63
64     def fullR(self, f):
65         delta_sf = lambda f : np.sqrt(copper_resistivity/(np.pi*f*mu))
66         return copper_resistivity*self.l/(self.w*delta_sf(f)*(1-np.exp(-self.t/delta_sf(f))))
67
68     def Z(self, f):
69         return (self.R + 1j*  (f)*self.L)/(1+1j*  (f)*self.C*self.R-(1j*  (f))**2*self.L*self.C)
70     def falseZ(self, f, R):
71         return (R + 1j*  (f)*self.L)/(1+1j*  (f)*self.C*R-(1j*  (f))**2*self.L*self.C)
72     def fullZ(self, f):
73         return (self.fullR(f) + 1j*  (f)*self.L) / (1+1j*  (f)*self.C*self.fullR(f)-(1j*  (f))**2*self.L*
    self.C)
74     def Q(self, f):
75         return -1*  (f)*(self.C*self.R**2 - self.L + self.C*self.L**2*  (f)**2)/self.R
76
77
78
79 N_total = int(1e3)
80 atol = 1e-2
81
82 d_in = 2.4e-3
83 w = 0.4e-3
84 s = 0.4e-3
85 t = 17e-6
86
87
88
89 k = []
90 M = []
91 L1 = []
92 L2 = []
93 L_series = []
94
95 for i in range(1,N_total):
96     L1_interne = Inductance(i, d_in, s, w, t)
97     L1.append(L1_interne.L)
98     L2.append(Inductance(N_total-i, L1_interne.d_out+s, s, w, t).L)
99     L_series.append(Inductance(N_total, d_in, s, w, t).L)
100
101     M.append((L_series[-1]  - L1[-1] - L2[-1])/2)
102     k.append(M[-1]/np.sqrt(L1[-1] * L2[-1]))
103
104
105 N = np.arange(1, N_total)
106
```

```
# Create the figure and the first Axes instance
fig, ax1 = plt.subplots()

# Plot k on the first Axes
ax1.plot(N, k, "r",label="k")  # change the line color to red
ax1.set_ylabel("k", color="red")  # change the label color to red
ax1.tick_params(axis='y', colors='red')  # change the tick color to red
ax1.xaxis.set_major_locator(MultipleLocator(base=N_total//10))  # Set major ticks every N_total/10
ax1.xaxis.set_minor_locator(AutoMinorLocator(4))  # Set minor ticks
ax1.set_xlabel("Number of secondary loops $N_s$")

# Create the second Axes instance, which shares the x-axis with ax1
ax2 = ax1.twinx()

# Plot M, L1, and L2 on the second Axes
ax2.plot(N, M, "r:", label="M")
ax2.plot(N, L1, label="$L_s$")
ax2.plot(N, L2, label="$L_p$", color="green")
ax2.set_yscale("log")
ax2.set_ylabel("Inductance [H]")

# Create a new x-axis with inverted values
ax3 = ax1.twiny()
ax3.set_xlim(ax1.get_xlim()[::-1])  # Reverse the x-axis limits
ax3.set_xlabel("Number of primary loops $N_p$")
ax3.xaxis.set_major_locator(MultipleLocator(base=N_total//10))  # Set major ticks every N_total/10
ax3.xaxis.set_minor_locator(AutoMinorLocator(4))  # Set minor ticks



N_L1eqL2 = np.where(np.isclose(L1, L2, atol=atol))[0][0]
rapport = int(N_L1eqL2)
print(np.where(np.isclose(L1, L2, atol=atol)))

print(f"Rapport : {rapport/(N_total-rapport)}")
print(f"k : {k[N_L1eqL2]}")


ax1.plot(np.argmax(k[50:]), np.max(k[50:]),"rv", label="$N_{k_{max}}$" + f" = {np.argmax(k[50:])} for \n"
    +" $k_{max}$ = " + f"{np.max(k[50:]):.2}")
ax2.plot(N_L1eqL2, L1[N_L1eqL2], "x", label="$N_{L_p=L_s}$"+f" = {N_L1eqL2}")
ax2.plot(np.argmax(M), np.max(M),"r^", label="$N_{M_{max}}$"+f" = {np.argmax(M)}")

# Add legends for both Axes
ax1.legend(bbox_to_anchor=(1.37,1.13))
ax2.legend(bbox_to_anchor=(1.08,0.93))

plt.savefig(r"C:\Users\Thall\OneDrive - UCL\Master\M moire\Suivi_TFE_DorianVN_partage\Labos\figures\
    MUTUAL_CHANGE_NAME.svg")

plt.show()
```

## A.3 MFLI induced voltage analysis

```
from matplotlib import pyplot as plt
import numpy as np
import matplotlib as mpl
import os

# ================================== Matplotlib parameters ==================================
plt.style.use('seaborn-whitegrid')
mpl.rcParams['lines.linewidth'] = 1
mpl.rcParams['lines.linestyle'] = '-'
plt.rcParams['figure.figsize'] = [7, 5]

# ================================== Function ==================================
def read_txt_file(file_path):
    data = []
    with open(file_path, 'r') as file:
        for line in file:
            if not line.startswith('%'):
                freq, amp, angle = map(float, line.split(';'))
                data.append((freq, amp, angle))
    return np.array(data)
```

```
21
22 def process_folder(folder_path):
23     files = [os.path.join(folder_path, f) for f in os.listdir(folder_path) if f.endswith('.txt')]
24     all_data = [read_txt_file(f) for f in files]
25
26     # Determine the minimum length
27     min_len = min([len(data) for data in all_data])
28
29     # Truncate data files to the minimum length
30     truncated_data = [data[:min_len] for data in all_data]
31
32     means = np.mean(truncated_data, axis=0)
33     stds = np.std(truncated_data, axis=0)
34
35     return means, stds
36
37 def plot_exact(folders, names, specific_freqs):
38     fig1, axs = plt.subplots(2, 1)
39     lines = []
40
41     specific_amplitudes_mean = []
42     specific_phases_mean = []
43     specific_amplitudes_std = []
44     specific_phases_std = []
45
46     elinewidth = 0.5  # Adjust this value to your preference
47
48     for folder, name in zip(folders, names):
49         means, stds = process_folder(folder)
50
51         # Amplitude plot
52         line0 = axs[0].errorbar(means[:, 0], means[:, 1], yerr=stds[:, 1], label=name, elinewidth=
    elinewidth)
53
54         # Angle plot
55         axs[1].errorbar(means[:, 0], means[:, 2], yerr=stds[:, 2], label=name, elinewidth=elinewidth)
56         lines.append(line0)
57
58         # Specific frequencies mean and std calculations
59         freq_indices = [np.abs(means[:, 0] - freq).argmin() for freq in specific_freqs]
60         specific_amplitudes_mean.append(means[freq_indices, 1])
61         specific_phases_mean.append(means[freq_indices, 2])
62         specific_amplitudes_std.append(stds[freq_indices, 1])
63         specific_phases_std.append(stds[freq_indices, 2])
64
65     # Formatting the frequency plots
66     for ax in axs:
67         ax.set_xscale("log")
68         ax.xaxis.grid(True, which='both')  # Add gridlines for x-axis
69
70     axs[0].set_ylabel("Amplitude [V]")
71     axs[0].set_yscale("log")
72     axs[1].set_ylabel("Phase [deg]")
73     fig1.legend(lines, names, loc='center right', bbox_to_anchor=(1.15, 0.5), frameon=True, facecolor='
    white')
74     plt.xlabel("Frequency [Hz]", weight='bold', fontsize=12)
75     plt.tight_layout()
76     plt.show()
77
78
79
80     # New figure for specific frequencies
81     fig2, axs2 = plt.subplots(2, 1)
82     x_ticks = np.arange(len(names))
83     offset = 0.2  # This value determines how far each frequency is from the main x-axis value. Adjust as
     needed.
84     colors = ['b', 'r', 'g', 'm', 'y', 'c', 'k']  # Assuming you have max 7 specific frequencies. Extend
    this list if needed.
85     handled_frequencies = set()  # Set to ensure each frequency is added to the legend only once
86     elinewidth = 0.5  # Adjust this value to your preference
87
88     for idx_freq, freq in enumerate(specific_freqs):
89         for idx_name, name in enumerate(names):
90             x_position = x_ticks[idx_name] + idx_freq * offset - (len(specific_freqs) - 1) * offset / 2
91             if freq not in handled_frequencies:
92                 label_amp = f'{freq:.1e} Hz'  # Format the frequency in scientific notation
```

```
                handled_frequencies.add(freq)  # Mark this frequency as handled
            else:
                label_amp = None  # This ensures the label is added to the legend only once
            axs2[0].errorbar(x_position, specific_amplitudes_mean[idx_name][idx_freq], yerr=specific_amplitudes_std[idx_name][idx_freq], label=label_amp, capsize=3, color=colors[idx_freq], fmt='.', elinewidth=elinewidth)
            axs2[1].errorbar(x_position, specific_phases_mean[idx_name][idx_freq], yerr=specific_phases_std[idx_name][idx_freq], capsize=3, color=colors[idx_freq], fmt='.', elinewidth=elinewidth)


    axs2[0].set_ylabel("Amplitude [V]")
    axs2[0].set_xticks(x_ticks)
    axs2[0].set_xticklabels([])  # Remove x-axis labels for the first subplot
    axs2[0].set_yscale("log")
    axs2[0].grid(True, axis="both", which='both')  # Add gridlines for x-axis

    axs2[1].set_ylabel("Phase [deg ]")
    axs2[1].set_xticks(x_ticks)
    axs2[1].set_xticklabels(names, rotation=20, ha='right')

    # Adding legend in the center right with white background
    handles, labels = axs2[0].get_legend_handles_labels()
    fig2.legend(handles, labels, loc='center right', bbox_to_anchor=(1.15, 0.5), frameon=True, facecolor='white')

    plt.tight_layout()
    plt.show()



def plot_relative(folders, names, specific_freqs):
    fig1, axs = plt.subplots(2, 1)
    lines = []

    ref_means, ref_stds = process_folder(folders[0])  # Get the data for the reference folder

    elinewidth = 0.5  # Adjust this value to your preference

    for folder, name in zip(folders[1:], names[1:]):  # Skipping the first folder, as it is our reference
        means, stds = process_folder(folder)
        ratio_amplitude = np.abs(ref_means[:, 1] - means[:, 1]) / ref_means[:, 1]
        ratio_phase = np.abs(ref_means[:, 2] - means[:, 2]) / ref_means[:, 2]


        # Calculate the standard deviations for the ratio values
        std_ratio_amplitude = ratio_amplitude * np.sqrt((ref_stds[:, 1] / ref_means[:, 1])**2 + (stds[:, 1] / means[:, 1])**2)
        std_ratio_phase = ratio_phase * np.sqrt((ref_stds[:, 2] / ref_means[:, 2])**2 + (stds[:, 2] / means[:, 2])**2)

        line0 = axs[0].errorbar(means[:, 0], ratio_amplitude, yerr=std_ratio_amplitude, label=name, elinewidth=elinewidth)
        axs[1].errorbar(means[:, 0], ratio_phase, yerr=std_ratio_phase, label=name, elinewidth=elinewidth)
        lines.append(line0)

    for ax in axs:
        ax.set_xscale("log")
        ax.xaxis.grid(True, which='both')  # Add gridlines for x-axis

    for freq in specific_freqs:
        axs[0].axvline(ref_means[np.abs(ref_means[:, 0] - freq).argmin(), 0], color='red', linestyle=':')
        axs[1].axvline(ref_means[np.abs(ref_means[:, 0] - freq).argmin(), 0], color='red', linestyle=':')

    axs[0].set_ylabel("Amplitude Ratio")
    axs[1].set_ylabel("Phase Ratio")
    fig1.legend(lines, names[1:], loc='center right', bbox_to_anchor=(1.15, 0.5), frameon=True, facecolor='white')
    plt.xlabel("Frequency [Hz]", weight='bold', fontsize=12)
    plt.tight_layout()
    plt.show()

    # Update the second plot to show ratios for specific frequencies
    fig2, axs2 = plt.subplots(2, 1)
    x_ticks = np.arange(len(names) - 1)  # Adjusted for skipping reference folder
```

```
    offset = 0.2  # This value determines how far each frequency is from the main x-axis value. Adjust as needed.
    colors = ['b', 'r', 'g', 'm', 'y', 'c', 'k']  # Assuming you have max 7 specific frequencies. Extend this list if needed.

    for idx_freq, freq in enumerate(specific_freqs):
        ref_idx = np.abs(ref_means[:, 0] - freq).argmin()
        ref_amp = ref_means[ref_idx, 1]
        ref_phase = ref_means[ref_idx, 2]
        ref_amp_std = ref_stds[ref_idx, 1]
        ref_phase_std = ref_stds[ref_idx, 2]

        for idx_name, name in enumerate(names[1:]):  # Skipping the first name, as it is our reference
            means, stds = process_folder(folders[idx_name + 1])  # +1 because we're skipping the reference
            data_idx = np.abs(ref_means[:, 0] - freq).argmin()
            amp = means[data_idx, 1]
            phase = means[data_idx, 2]
            amp_std = stds[data_idx, 1]
            phase_std = stds[data_idx, 2]

            ratio_amp = np.abs(ref_amp - amp) / ref_amp
            ratio_phase = np.abs(ref_phase - phase) / ref_phase

            std_ratio_amplitude = ratio_amp * np.sqrt((ref_amp_std / ref_amp)**2 + (amp_std / amp)**2)
            std_ratio_phase = ratio_phase * np.sqrt((ref_phase_std / ref_phase)**2 + (phase_std / phase)**2)

            x_position = x_ticks[idx_name] + idx_freq * offset - (len(specific_freqs) - 1) * offset / 2
            label_amp = f'{freq:.1e} Hz' if idx_name == 0 else None  # Only label the first time
            axs2[0].errorbar(x_position, ratio_amp, yerr=std_ratio_amplitude, label=label_amp, capsize=3, color=colors[idx_freq], fmt='.', elinewidth=elinewidth)
            axs2[1].errorbar(x_position, ratio_phase, yerr=std_ratio_phase, capsize=3, color=colors[idx_freq], fmt='.', elinewidth=elinewidth)

    axs2[0].set_ylabel("Amplitude Ratio")
    axs2[0].set_xticks(x_ticks)
    axs2[0].set_xticklabels([])  # Remove x-axis labels for the first subplot
    axs2[0].grid(True, axis="both", which='both')  # Add gridlines for x-axis

    axs2[1].set_ylabel("Phase Ratio")
    axs2[1].set_xticks(x_ticks)
    axs2[1].set_xticklabels(names[1:], rotation=20, ha='right')

    # Adding legend in the center right with white background
    handles, labels = axs2[0].get_legend_handles_labels()
    fig2.legend(handles, labels, loc='center right', bbox_to_anchor=(1.15, 0.5), frameon=True, facecolor='white')

    plt.tight_layout()
    plt.show()




if __name__ == "__main__":

    folders_path = [
                    r"C:\Users\Thall\OneDrive - UCL\Master\M moire\Suivi_TFE_DorianVN_partage\Labos\Bonnes mesures\MFLI\L1_1k_to_5M_1V_all_x5\NoSample",
                    r"C:\Users\Thall\OneDrive - UCL\Master\M moire\Suivi_TFE_DorianVN_partage\Labos\Bonnes mesures\MFLI\L1_1k_to_5M_1V_all_x5\Cri_10mm_1c",
                    r"C:\Users\Thall\OneDrive - UCL\Master\M moire\Suivi_TFE_DorianVN_partage\Labos\Bonnes mesures\MFLI\L1_1k_to_5M_1V_all_x5\Cri_10mm_5c",
                    r"C:\Users\Thall\OneDrive - UCL\Master\M moire\Suivi_TFE_DorianVN_partage\Labos\Bonnes mesures\MFLI\L1_1k_to_5M_1V_all_x5\Cri_10mm_10c"
                    ]

    measure_Name = [
                    "No Sample",
                    "Cri_1cm _1L",
                    "Cri_1cm _5L",
                    "Cri_1cm _10L",
                    ]

    # ... [Your folder_path and measure_Name definitions] ...
```

```
    specific_frequencies = [1e3, 1e5, 1e6]  # Change this list based on the frequencies you are
    interested in

    # Plot exact values
    plot_exact(folders_path, measure_Name, specific_frequencies)

    # Your reference folder path here:
    reference_folder = r"C:\Users\Thall\OneDrive - UCL\Master\M moire\Suivi_TFE_DorianVN_partage\Labos\
    Bonnes mesures\MFLI\L1_1k_to_5M_1V_all_x5\NoSample"

    # Plot relative differences
    plot_relative(folders_path, measure_Name, specific_frequencies)
```

**UNIVERSITÉ CATHOLIQUE DE LOUVAIN**
**École polytechnique de Louvain**
Rue Archimède, 1 bte L6.11.01, 1348 Louvain-la-Neuve, Belgique | **www.uclouvain.be/epl**